PACIFIC EARTHQUAKE ENGINEERING RESEARCH CENTER

City-Scale Multi-Infrastructure Network Resilience Simulation Tool

Kenichi Soga
Renjie Wu
Bingyu Zhao
Chaofeng Wang

Department of Civil and Environmental Engineering
University of California, Berkeley

PEER Report No. 2021/05

Pacific Earthquake Engineering Research Center
Headquarters at the University of California, Berkeley
August 2021

PEER 2021/05
August 2021

City-Scale Multi-Infrastructure Network Resilience Simulation Tool

Kenichi Soga
Renjie Wu
Bingyu Zhao
Chaofeng Wang

Department of Civil and Environmental Engineering
University of California, Berkeley

PEER Report No. 2021/05

Pacific Earthquake Engineering Research Center
Headquarters, University of California, Berkeley
August 2021

ABSTRACT

The goal of this project is to deliver a coherent framework of simulation tools that can quantify the performance of the water distribution network (WDN) and the transportation network at the city scale under different ground-motion scenarios. In addition to tool development, this project also investigates the potential interactions between structural and infrastructure systems in the case of normal operational and various earthquake damage scenarios. A multi-threaded, high-performance computing (HPC) scalable semi-dynamic traffic simulation model has been developed to understand the complex behaviors of the entire transportation system and to evaluate various performance metrics (e.g., traffic flow, delay, accessibility, etc.) in a large-scale hazard event. An efficient, multi-threaded C++ program, HydrauSim, has been created to understand the hydraulic behavior of WDNs after a disruptive hazard event such as an earthquake. Equipped with advanced linear system solvers, HydrauSim solves hydraulic parameters for a city-scale WDN almost instantaneously, allowing the water distribution change under many earthquake damage scenarios to be determined in a short time. To support a framework of holistic assessment of regional performance after earthquakes, multiple existing tools are integrated, including the ground-motion generation software from Stanford University and the building damage assessment tool rWhale from the SimCenter.

Earthquake scenarios (M7.05 Hayward fault) in the San Francisco Bay Area are studied to evaluate the infrastructure networks' hazard response using the developed tools. In collaboration with the East Bay Municipal Utility District (EBMUD), the WDN hydraulic responses on the EBMUD gravity feed zone (65,700 distribution pipes with a total length of 7,223,217 ft) under various ground movement conditions have been studied. The SimCenter building damage estimation tool, rWhale, is used to simulate building damage states for 1.8 million buildings across the Bay Area. On the traffic side, 2 million agents' movements on the full San Francisco Bay Area's road network (224,224 nodes with 549,009 links) has been simulated to understand potential traffic re-distributions after major hazard events. Interactions between these three infrastructure systems under the Hayward fault earthquake scenarios are explored in the study.

ACKNOWLEDGMENTS

This study was sponsored by the Pacific Earthquake Engineering Research Center (PEER). Any opinions, findings, and recommendations expressed in this material are those of the author(s) and do not necessarily express those of the funding agency(ies), PEER, or the Regents of the University of California. Portions of this work were carried out under National Science Foundation Grant SimCenter award number NSF-1612843.

The authors would like to acknowledge the generous support of PEER. Exchange student Miki Komatsu from Kobe University, Japan, helped on the development of transportation model. Graduate student Zhenxiang Su from U.C. Berkeley and Assistant Professor Krishna Kumar from the University of Texas at Austin contributed to the development of the water distribution network analysis toolkit: HydrauSim. Professor Jack Baker from Stanford University provided the earthquake ground-motion simulation software. All these contributions are greatly acknowledged.

CONTENTS

LIST OF TABLES

LIST OF FIGURES

Nomenclature

ACS American Community Survey

BPR Bureau of Public Roads

CH Contraction Hierarchy

CTPP Census Transportation Planning Products

FEMA Federal Emergency Management Agency

HPC High-Performance Computing

HPC High-performance computing

NIAC National Infrastructure Advisory Council

OD Origin-destination

OSM OpenStreetMap

TAZ Traffic Analysis Zone

VHT Vehicle Hours Traveled

WDN Water Distribution Network

WNTR Water Network Tool for Resilience

1 Introduction

1.1 OVERVIEW

This PEER project has developed simulation tools that quantify the resilience of city-scale infrastructure systems. Specifically, toolkits for hydraulics analysis of water distribution network and city-scale traffic simulation were developed for both normal and hazard scenarios.

A multi-threaded, high-performance computing (HPC) scalable semi-dynamic traffic simulation model has been developed to understand the complex behaviors of the entire transportation system and to evaluate various performance metrics (e.g., traffic flow, delay, accessibility, etc.) in response to a large-scale hazard event such as an earthquake. It adopts a semi-dynamic framework that divides an analysis period (typically 24 hours or during the peak morning hours) into 15-minute slices. In each time slice, the vehicles are gradually assigned to their shortest paths in batches. After each batch, the road link-level travel times are updated to reflect the traffic congestion. For trips that exceed the 15-minute window, the remaining part of the trip is added to the next 15-minute time step as “residual demand.” This framework captures the traffic dynamics during peak hours while still preserving the computational efficiency and flexibility for this large network.

To quantify the hydraulic behavior of water distribution networks (WDNs) after a disruptive hazard event such as an earthquake, an efficient, multi-threaded C++ WDN hydraulic simulator (HydrauSim) was developed. HydrauSim allows disruptive incidents (e.g., pipe leaks/breaks) to be included in the network analysis. The status of leakages is quantified through a modified pressure-demand-driven (PDD) model simulation. In addition to hydraulic simulation, HydrauSim also includes functionalities to analyze a WDN’s robustness from the point of view of isolation segments, which are defined as the smallest component to isolate a pipe from the remaining system. HydrauSim provides tools to read, configure, and analyze the impact of isolation segments concerning different isolation valve configurations and valve failure scenarios. Moreover, the hydraulic simulator in HydrauSim is optimized to simulate extremely large-sized WDNs; therefore, it is suitable for computationally-intensive tasks such as large-scale WDN hydraulic analysis or optimization procedures that requires many simulation runs.

Following the U.S. Geological Survey’s (USGS) HayWired Report (Hudnut et al., 2018), earthquake scenarios (M7.05 Hayward fault) in the San Francisco Bay Area were studied to demonstrate the capability of the proposed unified network model in simulating the earthquake impact for city infrastructure systems in cases of normal operational and various earthquake damage scenarios. This study adopted a probabilistic seismic hazard analysis (PSHA) as the general approach for simulating earthquake risk for the study area, the San Francisco Bay Area. A set of M7.05, Hayward-Rodgers Creek HN+HS earthquake rupture events from UCERF2 (Working Group on California Earthquake Probabilities(WGCEP), 2008) are simulated with spatial correlation considerations on earthquake intensity measures (IMs).

The generated IMs were used as input to estimate the earthquake's impact on the WDN and building systems. The earthquake impacts on a WDN were modeled herein as follows: (1) Using the simulated earthquake ground-motion IMs (PGV), the probability of failure for each network component was estimated using pipeline fragility curves; (2) Based on the estimated failure probability, certain components were sampled as the failed component with corresponding degrees of damage; and (3) A pressure-dependent hydraulic simulation was performed on the damaged network to estimate the water supply and degree of shortages anticipated for the case study. A Monte Carlo (MC) simulation was used to deal with uncertainties from across different ground-motion scenarios. The simulation was performed on East Bay Municipal Utility District's (EBMUD) main gravity feed zone. Around 200–800 pipes were estimated to break during the simulated earthquake events. On average, 25% of demand nodes may experience insufficient water pressure levels, which can rise to 78% for the worst case scenario.

The damage states of 1.8 million buildings after the hypothesized earthquake scenario across the San Francisco Bay Area were simulated using the SimCenter rWhale software (Elhaddad et al., 2019). With detailed building information and site-specific ground motions, rWhale evaluates the seismic performance of buildings using the FEMA P-58 method, in which a nonlinear structural dynamic analysis is performed to obtain the engineering demand parameters (EDPs), such as lateral drifts, accelerations, etc., caused by seismic ground motions. Around 30,000 buildings were considered as red tagged for the simulated earthquake scenarios.A "red-tagged" structure is defined as a building that has been severely damaged to the degree that the structure is too dangerous to inhabit.

Lastly, the regional impacts of earthquake-induced WDN and building damage were tied in through traffic simulations. Specifically, damaged water pipes were assumed to affect road connectivity, either due to water bursts or the presence of heavy repair equipment blocking roads. The building damage was assumed to affect the travel demand, as people cannot live or work in red-tagged buildings. Their trips are canceled proportionally according to the percentage of red-tagged buildings in a census tract (the smallest unit of the travel demand data). In addition, the capacity of the San Francisco—Oakland Bay Bridge was also assumed to be affected by the earthquake. Although the simulated changes in the traffic volume in the Bay Area during the peak morning hours immediately following the hypothesized earthquake scenarios were concentrated in the East Bay area near the rupture locations, neighboring areas are also affected due to commuting patterns. Regarding infrastructure system interdependence in both the immediately after the earthquake and the halfway recovered scenarios, the traffic performance metrics do not change much when pipeline damage is not considered. However, if building damage is not considered, the loss in travel demand is greatly underestimated. Under the scenario whereby the capacity of the Bay Bridge is reduced, both overall vehicle hours traveled (VHT) and individual trip times will increase as the remaining traffic needs to be rerouted.

1.2 ORGANIZATION OF THE REPORT

The report contains three main parts. Chapter 2 describes the developed scalable steady-state hydraulic simulation software, HydrauSim, for WDNs. It starts with theoretical descriptions of the physics of both demand-driven (DD) and pressure-demand-driven (PDD) model of hydraulic simulations. Detailed modeling implementations are illustrated that are followed by theoretical explanations. To model earthquake impacts on WDNs, water leakage due to network damage and the resulting sub-network isolation are modeled and implemented in the software. The software architecture and design concepts are also included as references for users and potential future contributors. Lastly, program performance has been profiled and compared to other hydraulic simulation software.

Chapter 3 describes the city-scale traffic modeling. An efficient traffic simulation tool is developed to evaluate the impact on the traffic system performance under earthquake-induced infrastructure damage. It adopts a semi-dynamic framework that divides an analysis period (typically 24 hours or during the peak morning commute hours) into 15-minute slices. In each time slice, the vehicles are gradually assigned to their shortest paths in batches. After each batch, the road link-level travel times are updated to reflect the traffic congestion. This does not guarantee user equilibrium, but nonetheless provides an approximated traffic distribution considering interactions between vehicles at peak hours. For trips that exceed 15 minutes, the remaining parts of the trips are added to the next 15-minute time step as “residual demand”. The benefit of adopting this framework is to capture the traffic dynamics during the peak hours while still preserving the computational efficiency and flexibility for this large network.

Following the USGS’s HayWired case study (Hudnut et al., 2018), Chapter 4 evaluates the potential impact of similar earthquake scenarios (M7.05 Hayward fault earthquake) on the San Francisco Bay Area to demonstrate the capability of using a collection of existing and newly developed tools into a framework of post-earthquake regional infrastructure performance assessment. It starts with the description of the earthquake ground-motion scenario generation. Probabilistic seismic hazard analysis is adopted as the approach for simulating earthquake risk for the area of study. Spatial correlated ground-motion IMs are generated on the region of study. By collaborating with East Bay Municipal Utility District (EBMUD), the detailed hydraulics of the water distribution network of the eastern Bay Area are modeled before and after the earthquake. A stochastic simulation approach is adopted to consider both ground motion and pipeline fragility uncertainties. Through analyzing hydraulic simulation results, potential earthquake induced water supply shortages are discussed. In addition to WDN analysis, the damage state of 1.8 million buildings after the hypothesized earthquake scenario across the San Francisco Bay Area is simulated using the SimCenter rWhale software (Elhaddad et al., 2019). Spatial distribution of the simulated red-tagged buildings in the study area after the hypothetical earthquake is presented. Lastly, the regional impacts of earthquake-induced WDN and building damage are united through traffic simulations. Temporal changes in the traffic system performance, which are the losses in the traffic system performance at different stages of an earthquake event (before, immediately after, halfway recovered, and fully recovered), are simulated in the study. Inter-dependencies between WDN, buildings, and traffic patterns are discussed.

2 Hydraulic Simulation for Water Distribution Networks

2.1 OVERVIEW

Water distribution networks are considered part of the critical infrastructure of every modern city by providing clean drinking water for industrial and residential usage. With the growth of population and the physical expansion of cities, WDNs in major cities tend to be large and complex. Considering the importance of the water supply and the increase of the size of WDNs and accompanying complexities, concerns over the resilience of the WDNs have risen in recent years (National Infrastructure Advisory Council (NIAC), 2009; Christodoulou and Fragiadakis, 2015; Shin and Burian, 2018). Recent experience from natural and man-made water-related disasters (Yoo et al., 2016a) suggests that current water infrastructure systems cannot protect against or prevent all disruptive events and may perform unreliably because of high uncertainty of disturbances, complicated inter-dependency of infrastructure systems, and stochastic failures resulting from unpredictable events (Asefa, 2014; Shin and Burian, 2018). The National Infrastructure Advisory Council (NIAC) states that the effectiveness of a resilient infrastructure or enterprise depends upon its ability to anticipate, absorb, adapt to, and/or rapidly recover from a potentially disruptive event. Based on this criterion, understanding how drinking water systems will perform during disruptive incidents is essential in characterizing the resilience of the WDNs.

Many water network analysis tools have been developed by researchers to quantify WDN resilience during disruptive incidents, especially in the case of seismic events. These tools can be grouped into two categories. The first group consists of tools that use empirical relationships for WDN damage estimations. Developed by Federal Emergency Management Agency (FEMA), HAZUS-MH (FEMA, 2018) is a GIS-based tool that estimates the damage of infrastructure (including WDNs) in terms of social and economic values under multi-hazard scenarios. For seismic hazard analysis, the Mid-America Earthquake Center developed MAEviz (Navarro et al., 2008) for infrastructure earthquake risk evaluation. Based on MAEviz, INCORE (Gardoni et al., 2018) was developed as an open-source multi-hazard assessment, response, and planning tool for community resilience planning. A major limitation of these tools is the lack of precision as that they do not explicitly model the hydraulic behavior of damaged WDNs. To overcome such issue, hydraulic simulation-based WDN risk analysis tools have been developed over the years. EPANET (Rossman et al., 2000), developed by the U.S. Environmental Protection Agency (EPA), is public domain software that models the hydraulics of water distribution systems. Based on the EPANET hydraulic simulator, many tools have been developed to model WDNs resilience. GIRAFFE (Shi et al., 2006) employs the iterative approach for the treatment of negative pressures in the damaged water supply system using the EPANET hydraulic solver. REVAS.NET (Yoo et al., 2016b) includes seismic events generation into the simulation process for a comprehensive WDN seismic resilience estimation. One drawback to using EPANET (version 2.0) is that it does not model network damage explicitly, and advanced hydraulic simulation techniques—such as pressure-driven hydraulic simulation—are not included, thus limiting the hazard analysis capability of the extended tools. Recently, an open-source python-based WDN resilience software, WNTR (Klise et al., 2020), has been developed, which is a comprehensive tool developed by EPA and Sandia National Laboratories that aims at WDN resilience analysis. However, the simulation speed of the WNTR hydraulic simulator is not scalable—an issue when considering the size of WDNs—thus making it unsuitable for a resilience analysis of large-scale WDNs or optimization tasks that require repeated hydraulic simulations.

This study developed a computer simulation package, HydrauSim, to understand the hydraulic behavior of WDNs after a disruptive hazard event such as an earthquake. HydrauSim is an efficient C++ program designed to analyze the robustness of WDNs. Robustness is defined herein as a WDNs capacity to absorb and adapt to a hazard. Similar to EPANET (Rossman et al., 2000) and WNTR (Klise et al., 2020), HydrauSim is capable of performing the following tasks:

1. Generate water network models from scratch or from existing EPANET formatted water network model input (EPANET INP) files;

2. Modify network structure by adding/removing components and changing component characteristics;

3. Modify network operation by changing initial conditions and component settings; and

4. Simulate network hydraulics (steady-state) using either a demand-driven mode (DD) or a pressure-driven mode (PDD).

Unlike EPANet, which targets simulating the normal operating conditions of WDNs, and WNTR, which deals with the resilience of WDNs in general, HydrauSim focuses on assessing the ability of WDNs to resist hazards on a whole system scale by extending the original EPANet .inp file to include disruptive incidents (i.e., pipe leaks) to the network. The status of leakages can be quantified through a modified pressure-driven model (PDM) simulation, as described in Section 2.2.2. In addition to hydraulic simulation, HydrauSim also includes functionalities to analyze a WDN's robustness from the point of view of isolated segments, which are defined as the smallest component to isolate a pipe from the remaining system (Jun and Loganathan, 2007a). Compared to WNTR, which provides limited functionalities in regards to isolated segments, HydrauSim provides tools to read, configure, and analyze the impact of isolation segments concerning different isolation valves configurations and valve failure scenarios (see Section 2.2.3). Moreover, the hydraulic simulator in HydrauSim is highly optimized to simulate extremely large-scale WDNs (see Section 2.4). Hence, it is more suitable for computatively intensive tasks such as large-scale WDN hydraulic analysis or optimization procedures that require many simulations. Note: the current version of HydrauSim does not include extended-time hydraulic simulation nor water-quality simulation. HydrauSim can be downloaded from `https://github.com/cb-cities/pipe-network`.

2.2 MODEL DESCRIPTION

2.2.1 Network Components

HydrauSim models a water distribution system as a collection with nodes connected by links; it follows the same approach as Klise et al. (2020) and Rossman et al. (2000). The nodes represent junctions and reservoirs. The links represent pipes, pumps, and valves. In addition, to control valves, isolation valves are also included for isolated segments of damage. General descriptions for the system components are listed below. Readers can refer Rossman et al. (2000) for detailed descriptions.

1. Junctions: Junctions are connections points for links in the network. Water paths split or merge on junctions.

2. Reservoirs: Reservoirs are external sources (with unlimited supply) of water to the network.

3. Pipes: Pipes are the media that conduct water from one junction to another junction in the network.

4. Pumps: Pumps raise the hydraulic head of the water across connecting junctions by injecting external energy into the passing water flow. The head gain from the pump is determined by their pump curves.

5. Valves: Valves act as flow regulators for the network by restricting the pressure or flow at the locations where they are installed.

Four different valve types are modeled in HydrauSim:

1. Pressure Reducing Valve (PRV): PRVs are used to limit the pressure at the locations where they are installed.

2. Flow Control Valve (FCV): FCVs are used to limit the passing flow to a desired amount.

3. Throttle Control Valve (TCV): TCVs are used to simulate partially closed valves.

4. Isolation Valve: Isolation valves are used to isolate damaged sub-networks from the main network to prevent the effects of individual events from spreading throughout the system.

A typical water distribution network is illustrated by Figure 2.1. Water demand is supplied from junctions, which are connected to water sources (reservoir and tank) via pipes. Pumps provide additional energy other than gravity to drive fluid motion, and valves are used to control fluid behavior or to isolate damaged part from the system.

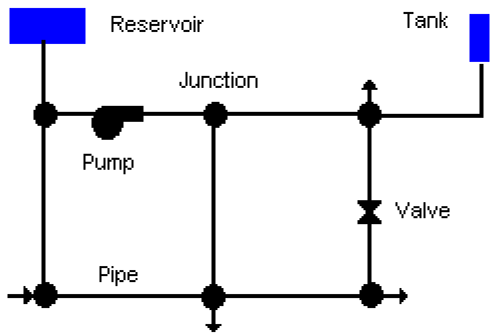

Figure 2.1: Physical components for a water distribution network [from Rossman et al. (2000)].

2.2.2 Steady-State Hydraulic Analysis

Basic Concepts

Hydraulic simulation of WDNs aims at simulating water distribution status for a given network. Two important quantities are simulated to represent the water distribution status at a given time. One is the flow rate inside pipes, Q, and the other is the hydraulic heads on junctions, H. Although a fast flow rate may damage pipes, a stagnant flow may lead to water-quality problems. Junction pressure is related to hydraulic heads by Equation (2.1). High pressure may break junctions, causing water leakage, whereas low pressure may produce insufficient water supply to end-users.

$$P = H - E \tag{2.1}$$

where P is the pressure, H is the hydraulic head, and E is the elevation for junctions of a WDN.

A large number of different flow conditions may occur in water pipeline systems, such as quasi-steady flow, surge, and water hammer (Mays et al., 2000). This study only considers the steady-flow condition, where flow conditions inside the network do not change dramatically over a short period of time. This is because under normal conditions with a relatively large simulation time step, flows inside the network can be approximated as steady state (Mays et al., 2000); the steady-state assumption is held by both Klise et al. (2020) and Rossman et al. (2000) as well. Two sets of governing equations are used for the steady-state flow simulation of WDNs (Todini and Rossman, 2013). The first governing equation raises from the law of conservation of energy across each pipe k :

$$H_i - H_j - \Phi(Q_k) = 0 \tag{2.2}$$

where i and j represent the nodes at the extremes of pipe k, and $\Phi(Q_k)$ describes the head loss due to friction as a function of flow.

The other governing equation arises from the law of conservation of mass on nodes, which states that total inflow must equal to total outflow at the junctions in the network.

$$\sum_{k=1}^{n_i} Q_{k_{i,j}} + q_i = 0 \tag{2.3}$$

where $Q_{k_{i,j}}$ is the flow in the pipe $k_{i,j}$ connected to junction i; n_i is the number of connected links on junction i; and q_i represents the demand or withdrawal rate on the junction i.

There are many formulas to describe the energy loss (i.e., head loss) across pipes, $\Phi(Q_k)$, in the energy conservation equation [Equation (2.2)]. Following Klise et al. (2020), the Hazen-Williams headloss equation is adopted in this work due to its simplicity and universality. The Hazen-Williams headloss formula is defined as:

$$h_k = 10.667C^{-1.852}d^{-4.871}Lq^{1.852} \tag{2.4}$$

where h_L is the energy loss (head loss) in the pipe k; C is the Hazen-Williams roughness coefficient; d represent the diameter of pipe k; L is the length of the pipe, and q is the flow rate of water in the pipe.

In summary, reservoirs/tanks in the network act as sources, which provide water to the end-users (sinks), who withdraw water to meet their demand from the end-service nodes. As water flows from the water sources to the end-users, energy is lost due to the friction of the pipe. To accommodate such energy loss (head loss), external energy sources (reservoirs and/or pumps) must be included to inject external energy into the system. Since system-component conditions, such as reservoir head and pump curves are known and fixed for a given WDN, the behavior of water distribution across the network will be determined by user demand (the sink rate) using the following equations: Equations (2.2), (2.3), and (2.4), which will be discussed below.

Demand Driven Simulation

In a demand-driven simulation, the distribution state of water, node pressure H, and link flow Q depends on the node demands, which are assumed to be known and must be met for the simulation to run properly. Such an assumption holds under normal operating conditions.

To solve the unknown H and Q, we combine and rewrite Equation (2.3) and Equation (2.2), which gives the following matrix notation, known as the global algorithm representation:

$$\begin{bmatrix} A_{11} & A_{12} \\ A_{21} & 0 \end{bmatrix} \begin{bmatrix} Q \\ H \end{bmatrix} = \begin{bmatrix} -A_{10}h_0 \\ -q \end{bmatrix} \tag{2.5}$$

where h_0 is the known nodal heads (from reservoirs); q is the known nodal demands (user demand); $A_{1,0}$ is a matrix relating the pipes to the fixed head nodes; $A_{1,1}$ is a diagonal matrix relating flow to headloss; $A_{1,2}$ is a matrix relating the pipes to the unknown head nodes; and $A_{2,1}$ is a matrix relating flows to known demand. See Todini and Rossman (2013) for detailed explanations.

Equation (2.5) is not linear because of the non-linearity of the headloss equation of Equation (2.4), which may be addressed using the Newton-Ralphson (NR) method:

$$J \cdot dx = R \tag{2.6}$$

where J is the Jacobian matrix; dx is the NR variable updating vector; and R is the residual vector. At each NR iteration, J and R need to be computed from the current state of unknown variables (H and Q) using the governing equations. The variable vector is updated by subtracting dx, which is updated by solving the linear system of Equation (2.6). This iterative process ends when the system residual reaches a small number ($< 1e-8$ as default). Note that unlike the EPANet's implementation (Rossman et al., 2000), which decomposes Equation (2.5) to solve H first and then updates Q, the same procedure in WNTR (Klise et al., 2020) is followed to solve the linear system in Equation (2.6) directly. Such simple implementation makes it easy to extend model functionalities when considering more governing equations, as will be shown below.

Pressure Depends Demand Simulation

Because WDNs may be damaged by natural hazards (earthquakes, etc.) or man-made hazards (power outages, etc.), in such cases, some of the nodes may experience low-pressure conditions due to pipe leaks, pump failures, or other broken components. Customers with low-pressure supply nodes do not always receive their requested demand. Hence, the basic assumption for the demand-driven simulation is no longer suitable, and the pressure depends demand (PDD) simulation needs to be used instead.

In the PDD simulation, the demand pressure relation is formulated with the following equation (Wagner et al., 1988):

$$d = \begin{cases} 0 & p \leq P_0 \\ D_f(\frac{p-P_0}{P_f-P_0})^{0.5} & P_0 \leq p \leq P_f \\ D^f & p \leq P_f \end{cases} \tag{2.7}$$

where d is the actual demand; D_f is the desired demand; p is the pressure; P_f is the nominal pressure, which is the pressure threshold that the consumer will receive the requested demand if it is met; and P_0 is the minimum pressure, which is the pressure threshold that the consumer will not receive any water if it cannot be met. Equation (2.5) can be easily extended to account for Equation (2.7). In addition to node head H and link flow Q, actual demand d will be included as unknown variables as well, and the pressure demand relation will be encoded by extending the A part [leftmost part in Equation (2.5)]. Note that nodal pressure is related to nodal head by Equation (2.1). The extended system equations can be directly solved using NR without further mathematical derivations, as described earlier.

Leak Model

One of the most common consequences of a damaged WDN is water leakage. For modeling purposes, pipe leaks are aggregated to their closest nodes. The leak is modeled using a general form of the equation by Crowl and Louvar (2001):

$$d_{leak} = C_d A p^{\alpha} \sqrt{\frac{2}{\rho}} \tag{2.8}$$

where d_{leak} is the leak discharge; C_d is the discharge coefficient; A is the area of the broken hole; p is the gauge pressure inside the pipe; α is the discharge coefficient; and the ρ is the density of the fluid. Similar to the PDD model in the previous section, Equation (2.5) can be extended to account for the leak model. The NR algorithm is still effective in solving the extended system of equations, which include the unknown leak discharges in addition to the nodal head, nodal demand, and link flow as part of the variables. Information on leaks can be configured through the extended .inp file; see Appendix A.1.

2.2.3 Isolation Segments

When WDNs are damaged, the damaged sections need to be isolated from the main network by closing the corresponding isolation valves to prevent the effects of individual events from spreading throughout the system (Jun and Loganathan, 2007a). For instance, damaged pipes need to be isolated from the system by closing at least two isolation valves before being repaired. Note, WDNs may have missing or inoperable valves in real-world scenarios due to human/environmental factors such as equipment aging. As a result, isolating the desired component may include other components of the system due to malfunctioning or missing isolation valves. For instance, consider the situation in Figure 2.2. If $P1$ is damaged and $V2$ is missing or inoperable, then isolating $P1$ will result in the isolation of $N2$ and $P2$. Moreover, when a segment is closed, there may be other parts of the network that become disconnected from the sources, creating unintended isolation. Therefore, understanding the properties of isolation segments concerning systems configurations and the consequences of missing/malfunctioning isolation valves is indispensable for assessing the resilience or robustness of WDNs. To achieve this goal, HydrauSim provides a "ValveGraph" module to read, model, and analyze the impact of isolation valves and their corresponding isolation segments on the system. Isolation-valve configurations can be imported through a modified version of the .inp file; see Appendix A.2. Efficient valve-segment analysis algorithms are implemented, which allows the user to: (a) find isolation segments inside the system; (b) evaluate the impact of valve failures; and (c) find any unintended isolation due to closure of desired segments.

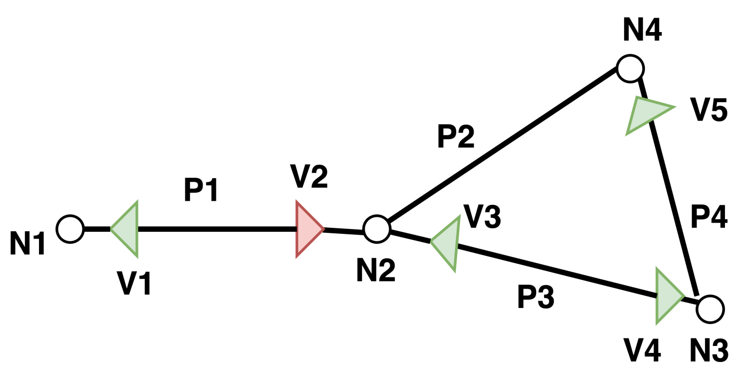

Figure 2.2: System configuration for isolation segment identification.

HydrauSim includes an automatic isolation segment-finding algorithm based on the algorithm proposed by Jun and Loganathan (2007b). By replacing the recursion structure with lookup tables, the modified structure is more computationally efficient compared to the original algorithm. The segment-finding algorithm detects the corresponding isolation segment information for a given pipe, including isolated pipes, isolated nodes, and isolation valves that need to be closed. The basic structure of the algorithm as follows:

1. For a pipe that needs to be isolated, the corresponding isolated nodes will be found first; they are pipe end nodes that do not have a valve installed on the searching pipe.
2. For a found isolated node i, its corresponding valve lacking pipes is found, which are pipes that do not have valves installed close to the node i.
3. Perform step 1 for the newly found valve-lacking pipes.
4. Stop when there is no pipe and node to explore.
5. Add all the valves that are related to isolated pipes and nodes as the valves that need to be closed for this segment. Program ends.

The above algorithm is illustrated by considering the system configuration in Figure 2.2 as an example. Assume pipe $P1$ need to be isolated, but valve $V2$ is broken: the segment finding algorithm works as follows:

1. Searches for isolated nodes of pipe $P1$, which is node $N2$.
2. Searches for valve-deficient pipes from node $N2$, which is pipe $P2$ ($P1$ has been explored).
3. Searches for isolated nodes of pipe $P2$, which is $N4$ ($N2$ has been explored).
4. Searches for valve-deficient pipes from node $N4$, of which there are none ($P4$ has $V5$).
5. If there are no new pipes or nodes to explore, add all related valves, which are $V1$, $V3$, $V5$. Isolated pipe $P1$ will result the isolation of $P1$, $P2$, and $N2$,$N4$ by closing $V1$, $V3$, $V5$.

The isolation-finding algorithm can be performed for all pipes to determine all potential isolation segments from the system layout. The found isolation segmentation and their corresponding valves can be used to construct a dual graph representation of the WDN, which represents graph nodes with isolation segments and links to those valves that should be closed (see Jun and Loganathan (2007b)). This segment-valve representation approach is adopted by HydrauSim to analyze the impact of component isolation and valve failures on the system. To isolate a malfunctioning pipe, one needs to find the corresponding isolation segments and close all the corresponding valves by removing its incident edges. Note, removal of one isolation segment may cause unintentional isolation for the system.

Consider the isolation of pipe $P2$ in Figure 2.1. The corresponding segment-valve representation is shown by Figure 2.3(a). Since $P2$ corresponds to segment $S2$, isolating $P2$ means the removal of edges that link to $S2$, which are $V2$, $V3$, and $V5$ in the graph. Removal of these links results in three mutually disjoint components in the graph; see Figure 2.3c). If we assume water comes from $N1$, then isolating pipe $P2$ will unintentionally cause the isolation of pipe $P3$ and $P4$ as there is no available connection to the water source for these two pipes. Representing the system with a segment-valve graph makes it easy to analyze the impact of valve failures. Failure of valves simply means the removal of such valves (edges) from the segment-valve graph and merging of the linked segments. For example, failure of valve v2 will result in the removal of edge v2 from the Figure 2.3(a) and the combination of segments $S1$ and $S2$. The isolation valves module of HydrauSim can automatically detect both intended and unintended isolation segments.

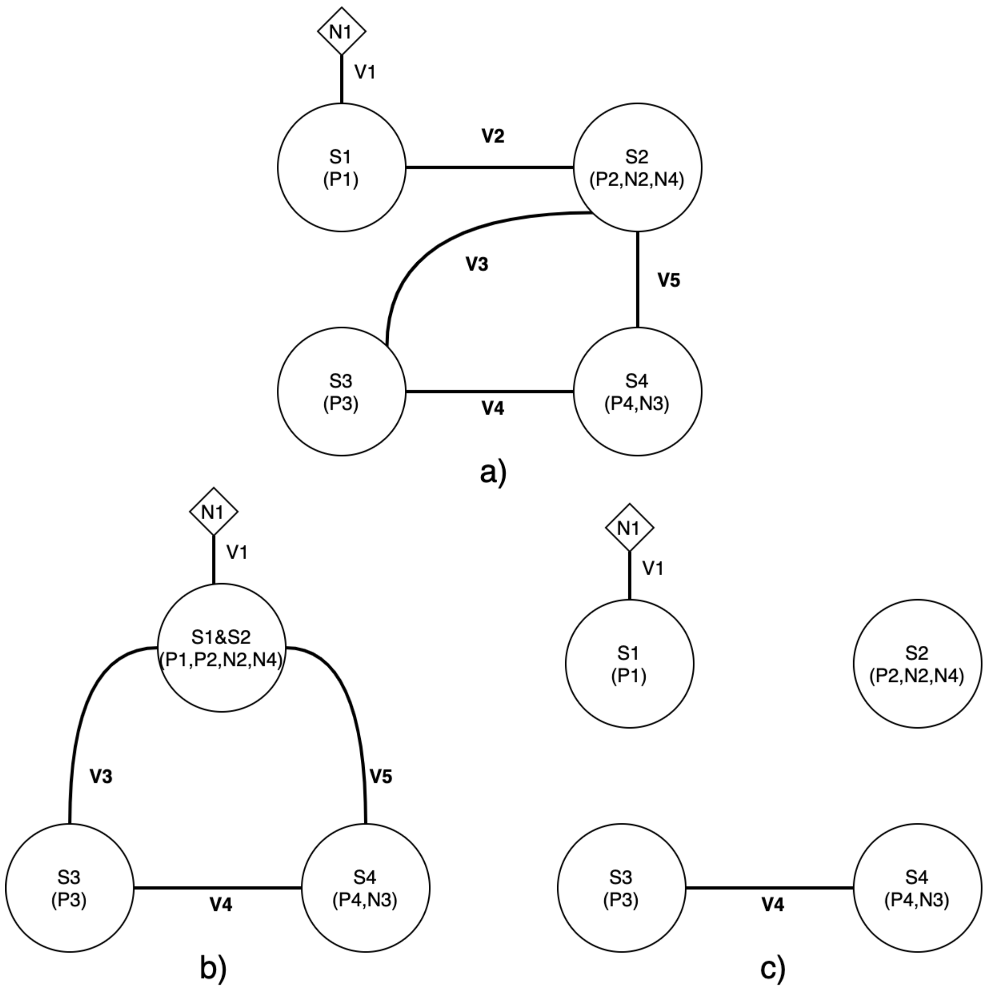

Figure 2.3: Segment-valve representation for a WDN shown by Figure 2.2: (a) all the isolation valves function properly; (b) valve $V2$ fails; and (c) unintended isolation due to the isolation of pipe $P2$.

2.3 PROGRAM DESIGN ARCHITECTURE

The architecture of HydrauSim is presented below for users to better understand, utilize, and potentially contribute to the program. The essential design principle for HydrauSim is the decoupling different types of functionalities as much as possible. In this way, the program can be relatively easy to extend with new features without much impact on the existing system. Figure 2.4 illustrates the simplified program design architecture of the program. The system is composed of six major parts:

1. Model Settings: parameter settings for the system, such as the initial value of flow rate of the hydraulic simulation, normal pressure for sufficient water supply on demand nodes, etc.
2. Nodes: nodal objects in the network, including junctions, tanks, and reservoirs.
3. Links: link objects in the network, including different types of pipes, valves, and pumps.
4. Mesh: an object that represents the network, which contains all the nodal objects, link objects, and network properties, such as links/nodes that are disconnected from water sources. Isolating segments resulting from closing isolation valves are also included in this category.
5. Matrix Assembler: an object that contains methods to compute, update, and store required matrices (Jacobian matrix, variables, and residuals) for hydraulic simulation from the network (the Mesh).
6. Simulator: an object that performs required hydraulic simulation (DD or PDD) for the network using matrices assembled by the Matrix Assembler. The linear system from NR method is solved either by a sequential solver (Eigen LU Solver) for a small network or a parallel solver (MKL Pardiso Solver) for a large network. Details on solver choices will be discussed in the next section.
7. IO: an object that contains protocols for reading .inp files and writing the simulation result back to a file.

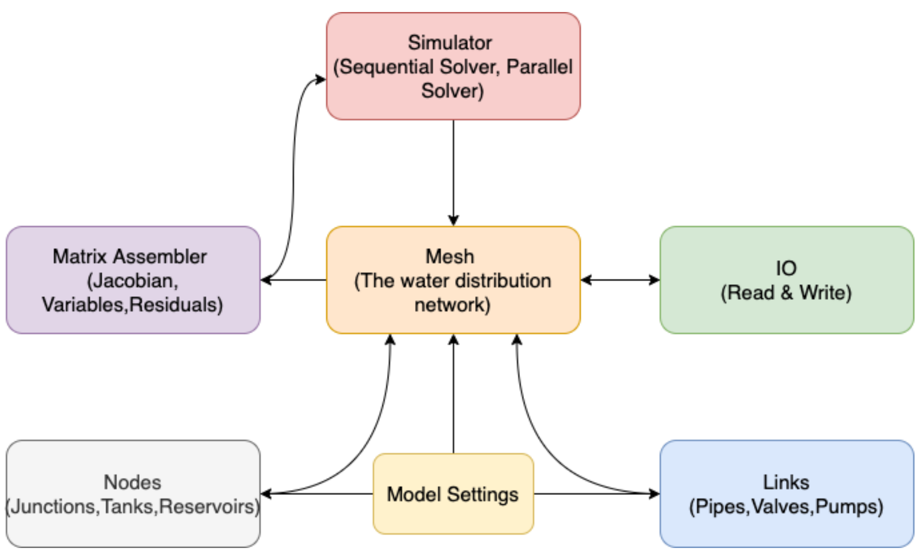

Figure 2.4: Software design architecture, simplified.

A typical workflow for the system is as follows: The IO module reads the .inp file from the user. The parsed information is then used to create the Mesh, which contains Nodes and Links. Network analysis—such as finding isolation segments—can be performed by the Mesh. To perform the steady-state hydraulic simulation, network information contained in the Mesh is assembled by the Matrix Assembler for use by the Simulator. The Simulator performs the desired simulation (e.g., DD/PD and leak quantification) and updates the Mesh with simulation results. Finally, the IO object can be called to export the analysis result back to the user.

2.4 PROGRAM PROFILING

One key feature of HydrauSim is its ability to perform steady-state hydraulic simulation for large-scale water distribution networks. Specifically, the simulation time for HydrauSim scales linearly to the network size, whereas both WNTR and EPANet exhibit nonlinear behavior for large networks. As shown in Figure 2.5, the simulation times for both WNTR and EPANet rise sharply for large-scale networks ($n > 10000$) compared to HydroSim. To achieve such computation efficiency, both SIMD (single instruction, multiple data) and MIMD (multiple instructions, multiple data) parallelism concepts were incorporated into the design of the hydraulic simulator. For SIMD, all simulation variables were vectorized using C++ package Eigen3 (Guennebaud et al., 2010) with Intel AVX (advanced vector extensions) enabled for Intel processors. In this way, the benefit of vector-focused modern computer architecture can be fully utilized for variable updating and residual computation during the simulation.

In addition, an adaptive approach was adopted to solve the linear system; see (Equation 2.6). Specifically, the Pardiso (De Coninck et al., 2016) unsymmetrical sparse linear system solver was used for large networks. Currently, one of the fastest modern linear system solvers, Pardiso parallels its computation over available cores of the host machine through MIMD. That said, multi-threading does have drawbacks. One major drawback is that multi-threading often requires a fixed amount of time as “threading overhead”, which may slow down the whole system when the actual computation time is small. Therefore, for small networks, the highly-efficient, sequential SuperLU solver from the Eigen3 package was used to solve the sparse linear system. The default network size setting for solver switching is 10,000 nodes, but this can be changed by the user for other considerations.

Based on the design configuration above, HydrauSim was constructed and profiled; see Figures 2.5 and 2.6. The testing system used was Ubuntu 18.043, Python 3.7; C++14, GCC 7.4 with Intel i7-9800X CPU, 64 Gb memory. WNTR V0.2.2 and EANETTools v1.0.0 were used for benchmark purposes. Note that profiling was performed using synthetic networks to ensure fixed network properties among networks with different sizes. In other words, only the network size—not network features inside the network—was the variable for the profiling procedure. The details of how to generate realistic synthetic networks is included in Appendix A.3.

As shown in Figure 2.5, there was no significant difference regarding simulation time for all simulators on small networks; however, for those networks that exceeded 10k, the advantage gained by using HydrauSim becomes obvious. For a network with 100k nodes, the simulation time for HydrauSim is around 5 sec; it is around 20 sec for EPANET and over 30 sec for WNTR. Profiling of the program also shows promising results. Figure 2.6(b) shows the majority of HydrauSim's computation time (94%) is due to the linearSystem solver part, implying efficient or even optimal computation is performed by other parts of system; the linear system solving time is rather fixed as advanced external library was used. Any endeavor to improve the performance is incumbent on the other part of the system.

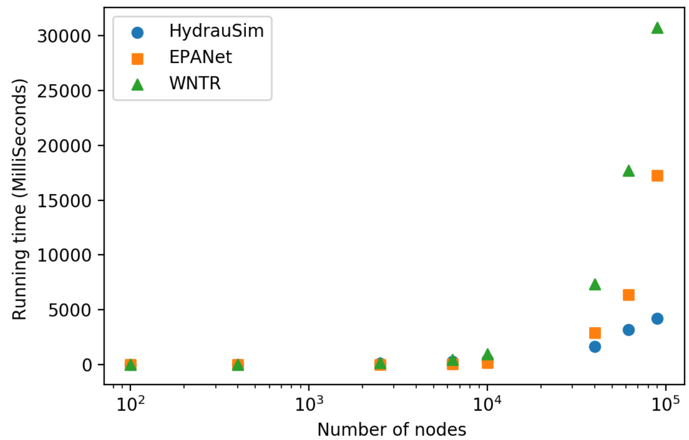

Figure 2.5: Hydraulic simulation speed for different WDN analysis software.

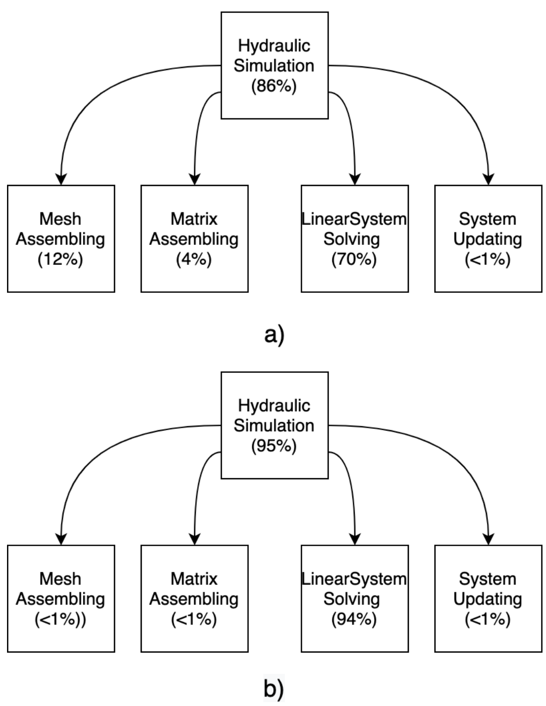

Figure 2.6: Profiling of hydraulic simulation systems: (a) EPANet and (b) HydrauSim.

3 Traffic Model

3.1 INTRODUCTION

With the increasing availability of transport-related data and improvements in computation techniques, methods to understand, predict, and control urban traffic patterns are also expanding. Unlike statistical models that estimate traffic conditions in the future that are based on past records (Ma et al., 2017), inferences made from traffic simulation models are less restricted by the availability of past information as training data. Instead, knowledge from multiple sources–such as crowd-sourced road networks, survey-based travel demands, and informed assumptions on complex human behaviors–can be incorporated into a single platform, thus providing the comprehensiveness and versatility required in evaluating traffic system performance in complex scenarios.

Traffic is a major indicator of regional economy. A healthy economy is often accompanied by vital traffic activities resulting from personal, business, and freight transport related trips (Metropolitan Transportation Comission (MTC)). In the face of natural disasters, damage to the transport infrastructure, as well as the relocation of residents and businesses, will reduce the vitality of the traffic activities. To understand the potential traffic disruption scenarios after earthquakes and multiple infrastructure damage, a semi-dynamic traffic simulation model is introduced in this chapter. The modeling framework is capable of incorporating the changes in the network supply and demand due to multiple forms of earthquake-induced infrastructure damage, such as bridge capacity reduction, population relocation as a result of unsafe buildings, and/or water supply deficiencies. A Python implementation of the model has been developed that runs relatively efficiently on a desktop computer or HPC clusters, taking advantage of the multi-core structure of modern computers. This enables multiple scenarios to be studied at the same time. A background of the model and integration framework is presented in Section 3.2, with detailed explanation of the modeling strategy given in 3.3. Specifications of the model inputs and outputs are described in Sections 3.4. The limitations of the model are discussed in Section 3.5. A case study that adopts the traffic simulation framework will be presented in Chapter 4. The code can be downloaded from `https://github.com/cb-cities/residual_demand`

3.2 BACKGROUND: FOUR-STEP TRAFFIC MODEL

The goal of traffic modeling is to predict the numbers of vehicles that use certain traffic facilities (e.g., a road link) at a particular time. Key traffic performance indicators, such as the total travel

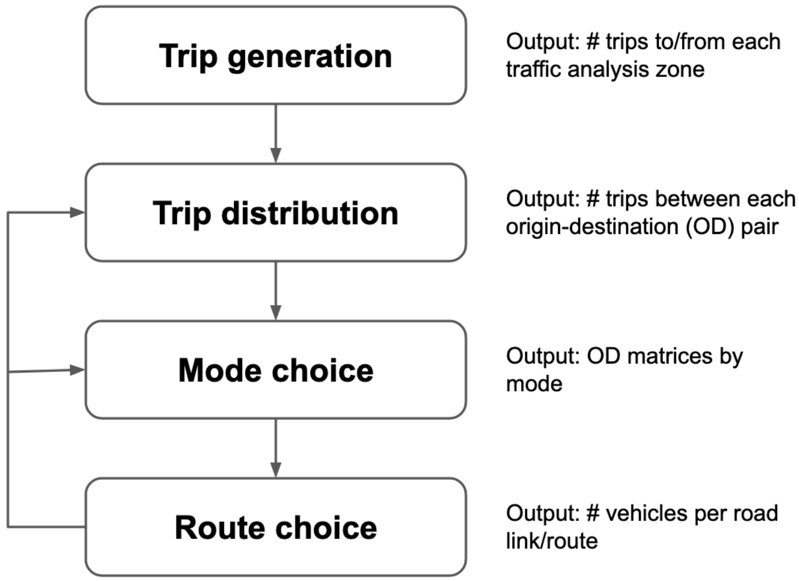

Figure 3.1: Four-step traffic model, adapted from Ait-Ali and Eliasson (2019).

time and congestion status, can be derived from model outputs. Traffic modeling is a spatio-temporal process; however, early traffic models, such as the still widely adopted four-step model, do not include temporal dynamics. Nevertheless, static models such as the four-step model are still widely adopted in real practice. In addition, they are the foundation of many advanced models, such as the residual-demand traffic assignment model presented below. The workflow of the four-step model is presented in Figure 3.1.

The modeling process begins with the analysis area being divided into Traffic Analysis Zones (TAZs), or other types of spatial subdivisions. In the first step, "trip generation"—the total number of trips starting and ending from each TAZ—is calculated based on demographic and land-use data. For example, residential areas experience a higher number of departures in the morning peak hours, while downtown and business locations have higher departure traffic in the evening peak hours. Next, in "trip distribution", the origin and destination locations generated from the previous step are matched to form the origin-destination (OD) pairs. This is equivalent to assigning a destination for each trip origin, constrained by the total numbers of trip origins and destinations from the TAZs. The output of this step is sometimes represented by an OD matrix, where the row and column headers indicate the starting and ending zones (or zone IDs) of the trips, and the matrix cell values represent the number of trips between each OD pair. In the third step, the "mode choice", the OD matrices obtained from the second step are split into OD matrices for each mode. This step is needed when a multi-modal transport system is considered, i.e., automobiles, public transits, and foot traffic. Lastly, a route is assigned to each trip in the OD matrices in the "route choice" step.

Criteria for the route assignment varies according to the model selected, but overall it is assumed that all trips will be assigned to the routes that maximize the utility of the travelers. Some theoretical framework for the route assignment includes the all-or-nothing assignment, where trips are assigned to the shortest path in free-flow conditions without considering vehicle interactions, or the Wardrop's User Equilibrium and System Optimum criteria are used, which involve optimization and distribution of the congestion throughout the network. The result of the "route choice" step is the link/route-level traffic flow and congestion status, which can be used as feedback for previous steps to adjust and optimize the trip distribution and mode choice, thus optimizing use of the transport system.

Apart from the four-step models, recent research has proposed activity-based models that replace the origin-destination (OD) pairs in the traditional four-step model with a chain of activities, e.g., home-work-shopping-home. Although activity-based models may represent the spatio-temporal travel demand in a more logical and behaviorally coherent way; it demands higher requirements of the model inputs.

This project used the four-step framework for the traffic simulation. Specifically, the travel demand was sourced from existing databases (Census Transportation Planning Products, CTPP (American Association of State Highway and Transportation Officials (AASHTO)), to generate OD pairs using Steps (1) and (2) listed above. As only vehicular trips will be considered, the third step—the mode choice—will be simplified to a single mode. Considering step 4—the traffic assignment and address the limitation of the static four-step assignment by including temporal dynamics—we developed a semi-dynamic residual demand assignment to more realistically model congestion and time delays in the city-scale road network compared to the more frequently used static models. Details of this model will be given in Section 3.3.3.

3.3 MODEL DESCRIPTION

Before the semi-dynamic traffic assignment model is introduced in Section 3.3.3, the concepts of routing and link-level traffic performance curves are explained below. These two concepts were fundamental in developing the semi-dynamic traffic assignment model with residual demand.

3.3.1 Individual Traffic Behavior: Shortest-Path

For each individual trip, the most common assumption considers that a traveler follows the shortest or fastest path to reach its destination in a road network. Consider the road network shown in Figure 3.2(a), where the link travel time is given by the numbers next to each road, the shortest path from the left-most node to the right-most node is the horizontal path, with the shortest path length of 4.5 units.

These shortest paths can be calculated using the Dijkstra's algorithm or its variations; however, on a large network with many OD pairs, the shortest path calculation can quickly lead to overwhelmingly high computation time. Since the computational time of the shortest path algorithms increases with the size of the graph (number of nodes and edges), the computation speed can be improved if the graph is simplified. To make the shortest path calculation more efficient, we used the contraction hierarchy (CH) algorithm to modify the Dijkstra's algorithm. (Geisberger et al., 2008; Urban Data Science Toolkit (UDST), 2021). The core idea of the CH algorithm is illustrated

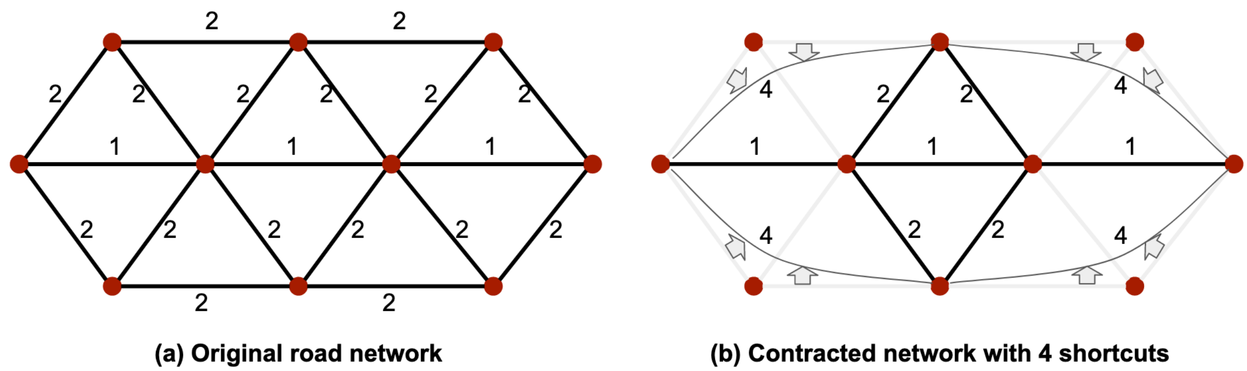

Figure 3.2: Shortest path computation on the original road network using the contraction hierarchy.

in Figure 3.2(b). In CH, nodes are removed in sequence, and new shortcuts between neighboring nodes of the removed node are added to the graph if the removed node is on the shortest path between the two neighboring nodes. When querying for the shortest path, a search is performed from both the origin and the end nodes, but only needs to search for edges of increasing hierarchy, which reduces the search time.

In reality, routing behaviors can be difficult to model accurately. For example, under the rationality assumption, people will seek those options that maximize their utilities. In terms of traffic routing, this can be translated as seeking the route that minimizes the travel-time cost, monetary cost, or other forms of cost. Time costs are frequently used as the standard for modeling route choices. The travel time of a trip is not static and is dependent on both the time of the day and the presence of other vehicles on the road network. To reflect the impacts of other vehicles, link performance functions can be used to update the travel time for each trip segment. This will be introduced in Section 3.3.2.

3.3.2 Link-Level Congestion Description: Volume-Delay Curves

The time that it takes for a vehicle to traverse a road link depends on the congestion status of the link. Under the free-flow conditions—where very light or no traffic is present—vehicles can drive at the speed limit (25 mph for most local roads and 50–70 mph for highways). As the road becomes more congested, the traffic speed also reduces until reaching a standstill condition. This relationship, represented by the fundamental diagrams of traffic flow, as illustrated in Figure 3.3, shows the empirical relationships between three traffic-related quantities: speed, density, and flow. Among them, speed reduces monotonically with density, while flow—as a multiplication of speed and density—has a two-phased relationship with either of the two other variables.

Note key points A and B shown in Figure 3.3. Starting from the free-flow condition (density is zero and speed equals to the free-flow speed), the speed remains at or close to the free-flow speed until point A. This is the division of the road status when the traffic is relatively light. As the traffic density increases, the flow reaches its maximum value (saturation flow) at point B. After

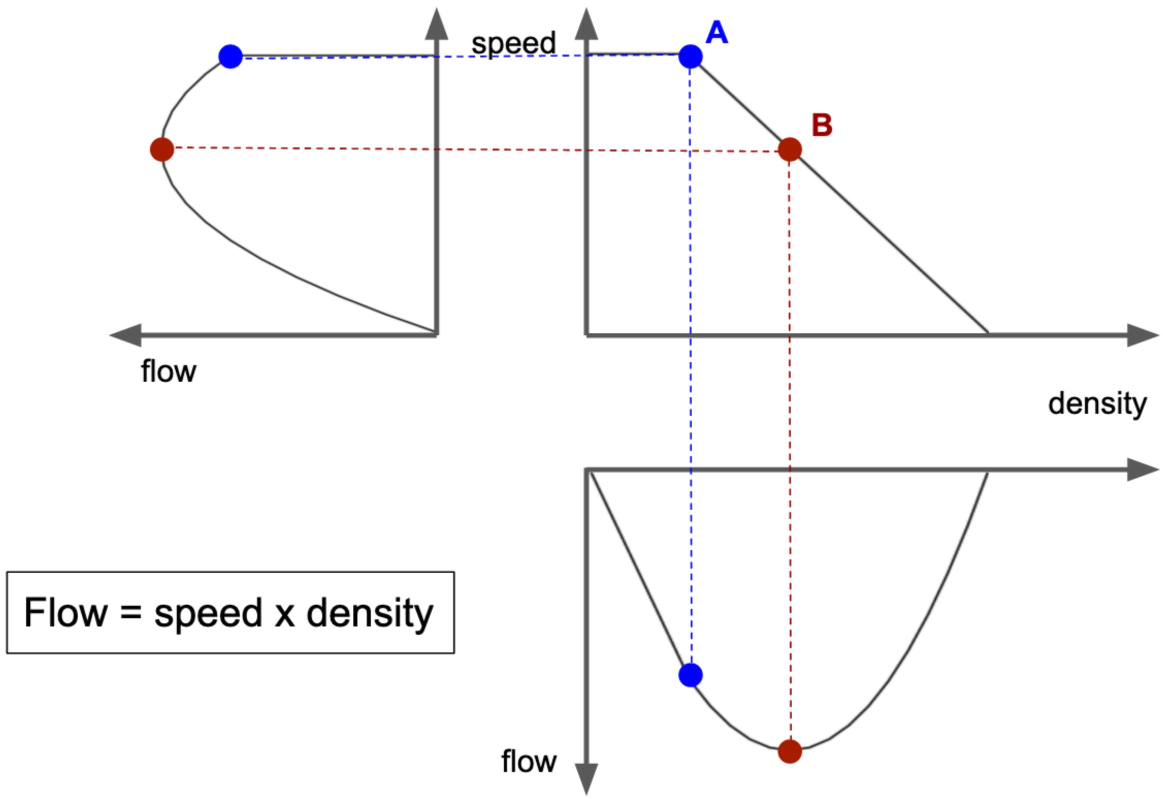

Figure 3.3: Illustration of the fundamental diagram of traffic flow.

this point, the flow will decrease due to the reduced speed in response to the increase in traffic density. This usually corresponds to the congested states of the road link. Finally, the density reaches its maximum value (jam density), where the vehicles are in a standstill condition, at which point both the speed and flow on the link become zero.

Various mathematical relationships have been proposed to describe the empirical relationships between speed, flow, and density. Some of the notable models are given in Figure 3.4. In the semi-dynamic assignment framework, The volume delay representation adopts a simplified version of the fundamental diagram. The most famous volume-delay relationship is proposed by the Bureau of Public Roads (BPR), which uses a power function to associate the volume-to-capacity ratio of the road to the travel time delays; see Equation 3.1.

$$t = t_0 \times (1 + \alpha(volume/capacity)^{\beta}) \tag{3.1}$$

where t and t_0 are the time to traverse a road link in traffic and free-flow conditions, respectively. *Volume* and *capacity* are the number of vehicles passing a road link and the maximum flow capacity in unit time (e.g., in one hour). *Alpha* and *beta* are calibration parameters specific to the area of study. In this study, *alpha* = 0.6 and *beta* = 1.2 are used. A city-specific multiplication factor of 1.2 is applied to t in accordance with the parameters used in Çolak et al. (2016).

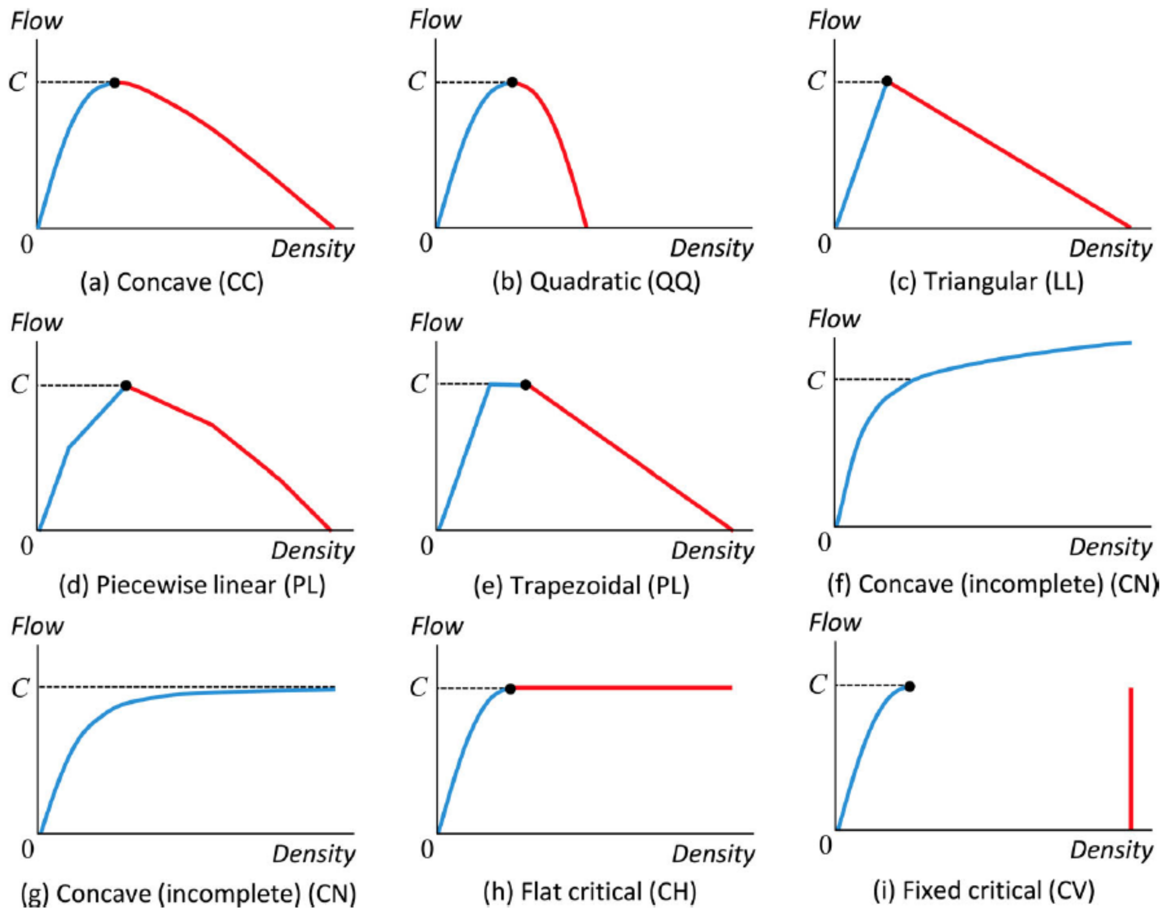

Figure 3.4: Various forms of fundamental diagrams in the literature, from Bliemer et al. (2017).

The use of volume-delay curves is not without criticism. First of all, the original parameters for the BPR curves were calibrated according to the U.S. road conditions in the 1950s and 1960s, which are different from the conditions nowadays. To correct for it, various modifications have been proposed, from city-specific correction factors in Çolak et al. (2016), to street-specific calibrations using crowd-sourced data (Casey et al., 2020). In addition, due to its omission of the hyper-congested branch of the fundamental diagram (where the flow decreases with increasing congestion, i.e., passing point B in Figure 3.3), it fails to capture key features of traffic (e.g., backward propagation waves).

Related to this drawback, Bliemer et al. (2017) has pointed out that using a BPR-curve style function results in a traffic flow that exceeds capacity and will only be penalized with unrealistically high travel times; in reality, the flow should never exceed the capacity. Despite these drawbacks, volume-delay functions are still the most convenient for use in numerical studies due to the monotonic depiction of the relationship between the assigned volume and link travel time, especially in regards to static traffic assignments.

3.3.3 Network-Level Traffic Dynamics: Semi-Dynamic with Residual Demand

In emergency situations such as earthquakes, the traffic conditions change hour-by-hour. Even in non-emergency situations, i.e., during the peak hours, traffic flow may exhibit strong temporal fluctuations. To capture these temporal dynamics more realistically, the conventional static assignment is modified to include time steps. The static assignment process assumes a large assignment period (three hours to a whole day), and that all vehicles finish their trips in the assignment period. This assumption can no longer hold in the proposed assignment framework, as the assignment period (e.g., 15 minutes) will generally be shorter than the duration of typical trip. To address this inconsistency between the assignment period and trip duration, the concept of residual demand is introduced; the assignment process is illustrated in Figure 3.5.

For trips with a given origin, destination, and departure time [see Figure 3.5(a) while assuming an assignment time step T (e.g., 15 minutes), an initial route is planned; see Figure 3.5(b). After time T, the vehicle may not reach its destination and can only reach the intermediate stop location; see Figure 3.5(c). At this time step assignment, the traffic condition for the unfinished part of the initial route [see dashed line in Figure 3.5(c)] might have been changed, e.g., due to the presence of other vehicles or emergency road closures. The trip from the intermediate stop to the destination then enters the next time step, as the "residual demand" from the previous time slice. A new route is planned according to current traffic condition; see Figure 3.5(d). This routing, stop, and rerouting process is repeated until the vehicle has reached its destination. For trips that stop in the middle of the link, the intermediate stop location is randomly sampled from the start and the end of the link according to the remaining time.

The residual demand assignment framework is built upon the shortest path calculation algorithms for computing routes; see Section 3.3.1. The link travel time used for routing on the road network graph is determined using the volume-delay function shown in Section 3.3.2. Within each assignment interval T, all trips are assigned separately in batches to guarantee a certain level of equilibrium; however, due to the computational time, strict equilibrium is not attempted.

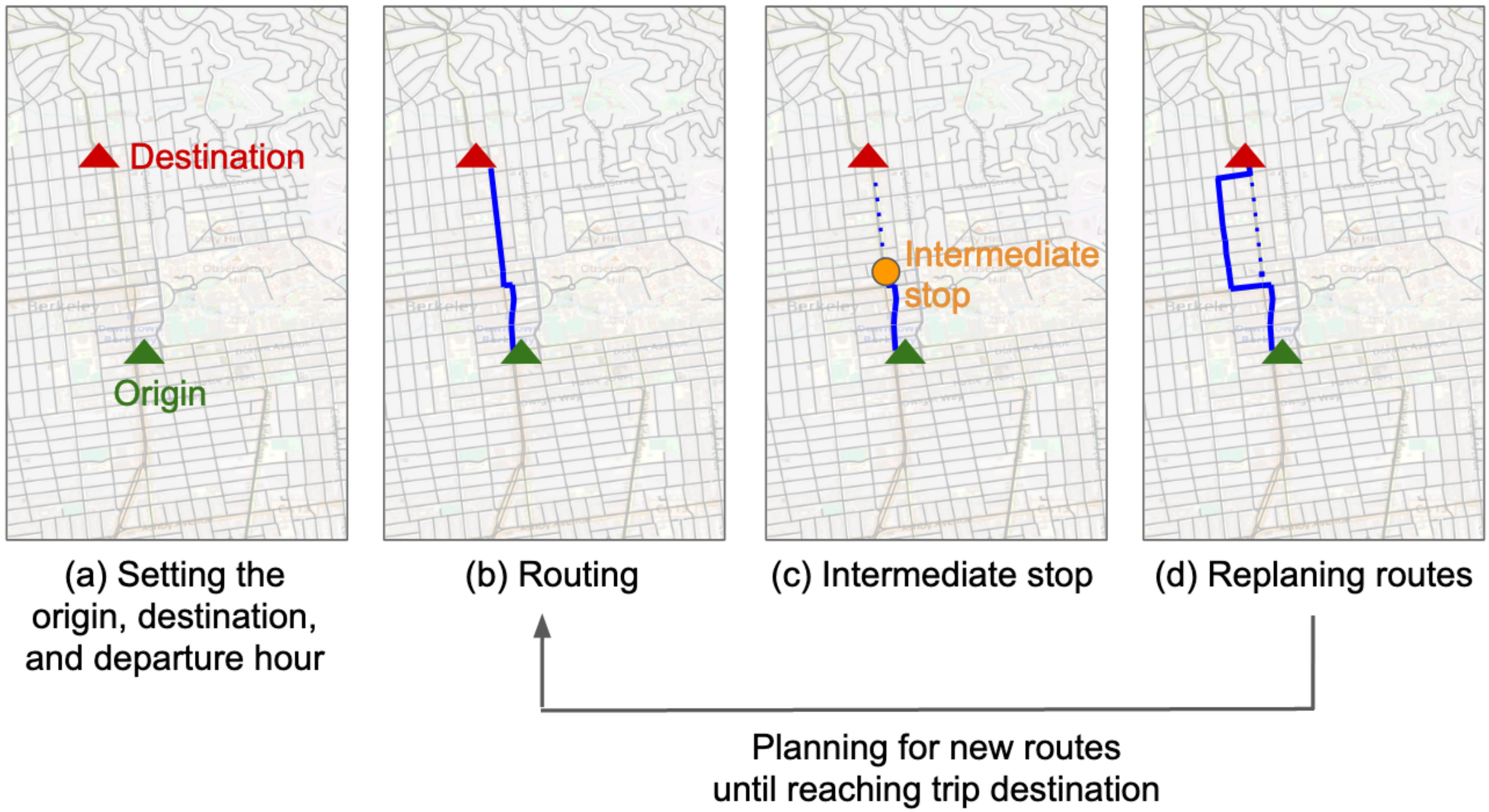

Figure 3.5: Illustration of route assignment with residual demand across time steps.

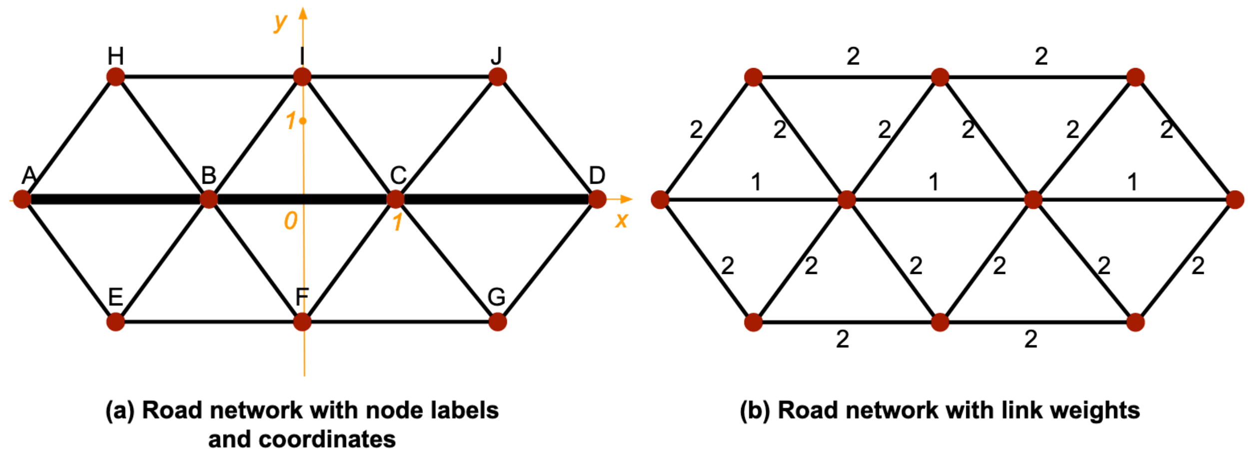

Figure 3.6: Road network replotted from Figure 3.2, with (a) all nodes labeled; and (b) link weights.

3.4 INPUTS AND OUTPUTS

In this section, the inputs required and standard outputs are given. The road network shown in Figure 3.2(a) is replotted in Figure 3.6 as an example. Specifically, Figure 3.6(a) has all nodes labeled (A to J), and Figure 3.6(b) shows the link weights, where 1 is 15 minutes, and 2 means 30 minutes. Modifications can be introduced to the inputs to incorporate specific earthquake-induced infrastructure damage scenarios. In addition, further post-processing can be conducted based on the standard outputs to obtain problem-specific metrics.

3.4.1 Inputs: Network and Demand

The first set of inputs is the graph nodes and edges, as shown in Tables 3.1 and 3.2. The needed information for nodes include a sequential ID of each node ($node\_id$) as well as its label ($node\_label$). The coordinates x and y can be used to calculate the length of the links as well as for plotting and visualization purposes. For links, the basic information required includes the sequential id ($edge\_id$), the ID and label of the start and end nodes ($start\_nid$, $start\_node$, end_nid, and end_node). Since all links are directed, $A \to B$ is a different link from $B \to A$. Also, the free-flow traversal time fft, as well as the *capacity* in vehicles per hour, are needed for calculating and updating the link-level travel time. Among all the links, the route that connects A, B, C, and D are considered to be of a higher class, which have shorter travel times as well as higher capacity compared to the rest of the links.

The second set of inputs is the travel demand. It is given herein as the OD matrix shown in Table 3.1. A separate OD matrix can be supplied for each time step. As a simplified example, it is assumed that all trips begin at time 0. There are 5000 trips going from node A to node D, and 2000 trips from node A to node G. A total of 3000 trips start from node H; while 2000 trips go to node D, the rest 1000 go to node G.

Table 3.1: Node-level information inputs for network in Figure 3.6.

node_id	*node_label*	*x*	*y*
0	A	-3	0
1	B	-1	0
2	C	1	0
3	D	3	0
4	E	-2	-1.73
5	F	0	-1.73
6	G	2	-1.73
7	H	-2	1.73
8	I	0	1.73
9	J	2	1.73

3.4.2 Outputs: Link and Trip-Level Information

The output of the residual assignment includes the time-stepped traffic volume per road link; see Figure 3.7. It can be seen that for trips that cannot finish in one time step (15 minutes), the distribution of traffic gradually moves from the left side (locations of the origin nodes) to the right side (destination nodes). Based on these outputs, further outcome metrics can be derived, such as the total traffic flow by link; see Figure 3.8.

Apart from link-level traffic, it is possible to obtain outputs on a per-trip basis. Figure 3.9 shows the histogram distribution of the trip-level travel time. From trip-level data, many other quantities can be derived, such as those portions of the trips with increased travel time before and after network disruptions. This is particularly useful in assessing the spatial vulnerable communities after earthquake-induced infrastructure damage.

Table 3.2: Link-level information inputs for network in Figure 3.6.

edge_id	*start_node*	*end_node*	*start_nid*	*end_nid*	*fft*	*capacity*	*geometry*
0	A	B	0	1	1	4000	LINESTRING(-3 0, -1 0)
1	B	A	1	0	1	4000	LINESTRING(-1 0, -3 0)
2	B	C	1	2	1	4000	LINESTRING(-1 0, 1 0)
3	C	B	2	1	1	4000	LINESTRING(1 0, -1 0)
4	C	D	2	3	1	4000	LINESTRING(1 0, 3 0)
5	D	C	3	2	1	4000	LINESTRING(3 0, 1 0)
6	A	E	0	4	2	2000	LINESTRING(-3 0, -2 -1.73)
7	E	A	4	0	2	2000	LINESTRING(-2 -1.73, -3 0)
8	E	B	4	1	2	2000	LINESTRING(-2 -1.73, -1 0)
9	B	E	1	4	2	2000	LINESTRING(-1 0, -2 -1.73)
10	B	F	1	5	2	2000	LINESTRING(-1 0, 0 -1.73)
11	F	B	5	1	2	2000	LINESTRING(0 -1.73, -1 0)
12	F	C	5	2	2	2000	LINESTRING(0 -1.73, 1 0)
13	C	F	2	5	2	2000	LINESTRING(1 0, 0 -1.73)
14	C	G	2	6	2	2000	LINESTRING(1 0, 2 -1.73)
15	G	C	6	2	2	2000	LINESTRING(2 -1.73, 1 0)
16	G	D	6	3	2	2000	LINESTRING(2 -1.73, 3 0)
17	D	G	3	6	2	2000	LINESTRING(3 0, 2 -1.73)
18	E	F	4	5	2	2000	LINESTRING(-2 -1.73, 0 -1.73)
19	F	E	5	4	2	2000	LINESTRING(0 -1.73, -2 -1.73)
20	F	G	5	6	2	2000	LINESTRING(0 -1.73, 2 -1.73)
21	G	F	6	5	2	2000	LINESTRING(2 -1.73, 0 -1.73)
22	A	H	0	7	2	2000	LINESTRING(-3 0, -2 1.73)
23	H	A	7	0	2	2000	LINESTRING(-2 1.73, -3 0)
24	H	B	7	1	2	2000	LINESTRING(-2 1.73, -1 0)
25	B	H	1	7	2	2000	LINESTRING(-1 0, -2 1.73)
26	B	I	1	8	2	2000	LINESTRING(-1 0, 0 1.73)
27	I	B	8	1	2	2000	LINESTRING(0 1.73, -1 0)
28	I	C	8	2	2	2000	LINESTRING(0 1.73, 1 0)
29	C	I	2	8	2	2000	LINESTRING(1 0, 0 1.73)
30	C	J	2	9	2	2000	LINESTRING(1 0, 2 1.73)
31	J	C	9	2	2	2000	LINESTRING(2 1.73, 1 0)
32	J	D	9	3	2	2000	LINESTRING(2 1.73, 3 0)
33	D	J	3	9	2	2000	LINESTRING(3 0, 2 1.73)
34	H	I	7	8	2	2000	LINESTRING(-2 1.73, 0 1.73)
35	I	H	8	7	2	2000	LINESTRING(0 1.73, -2 1.73)
36	I	J	8	9	2	2000	LINESTRING(0 1.73, 2 1.73)
37	J	I	9	8	2	2000	LINESTRING(2 1.73, 0 1.73)

Table 3.3: Travel demand OD matrix for the network in Figure 3.6.

Origin - Destination	D	G
A	5000	2000
H	2000	1000

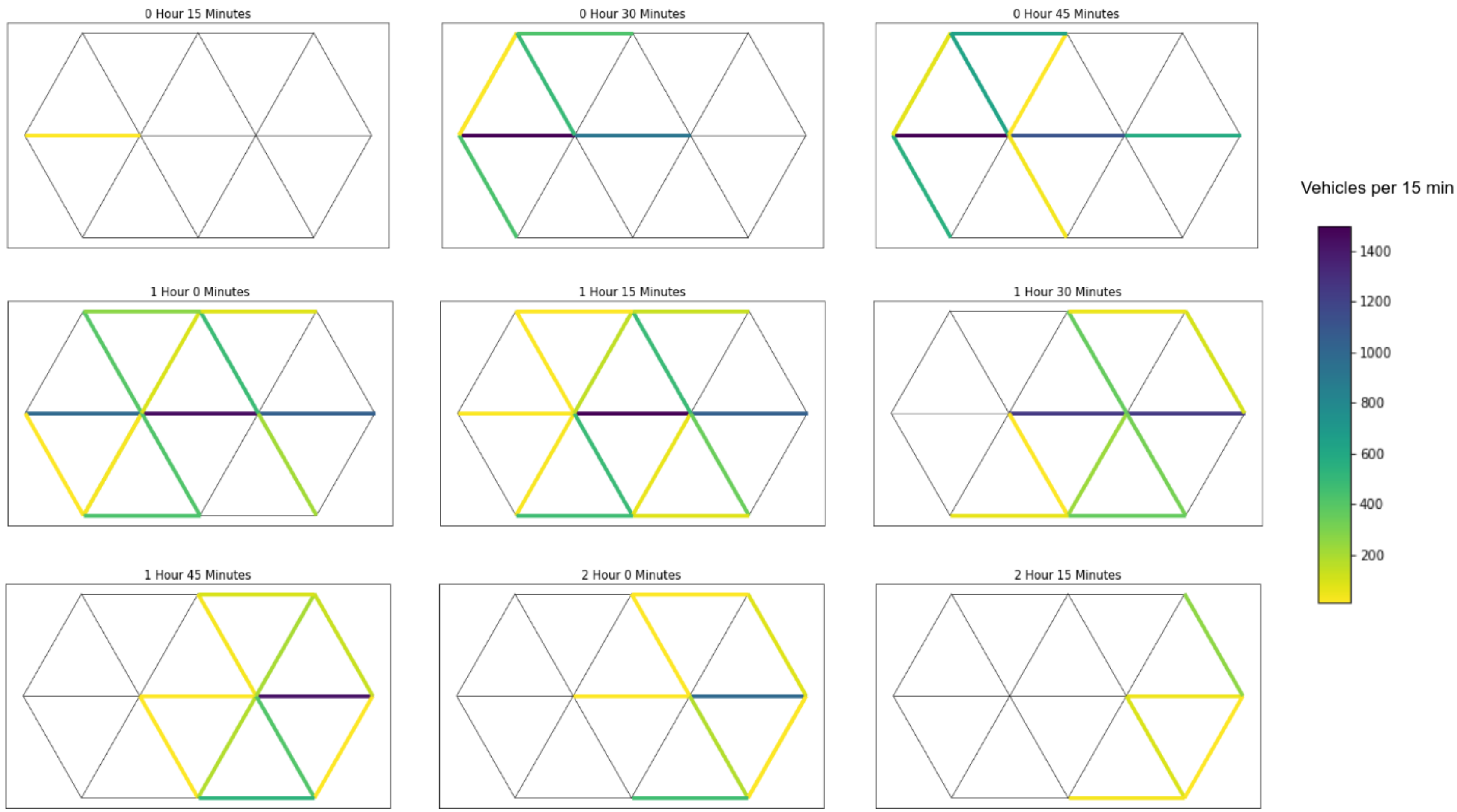

Figure 3.7: Output example: link-level traffic flow per time step.

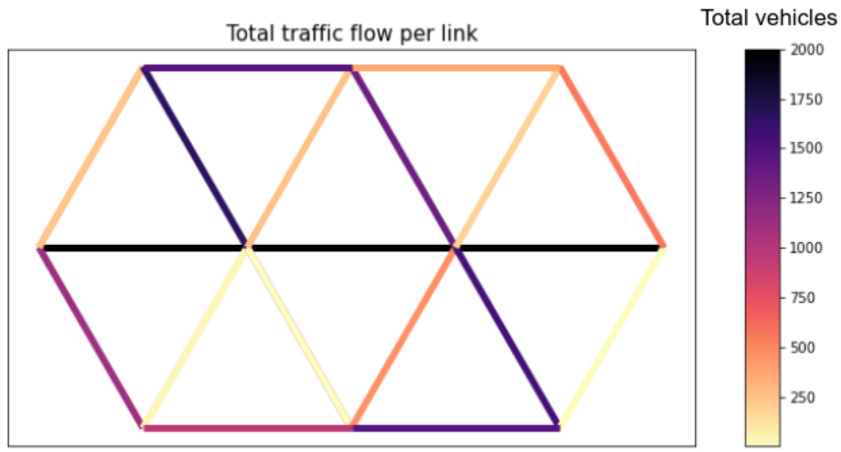

Figure 3.8: Output example: total link-level traffic flow during the analysis period.

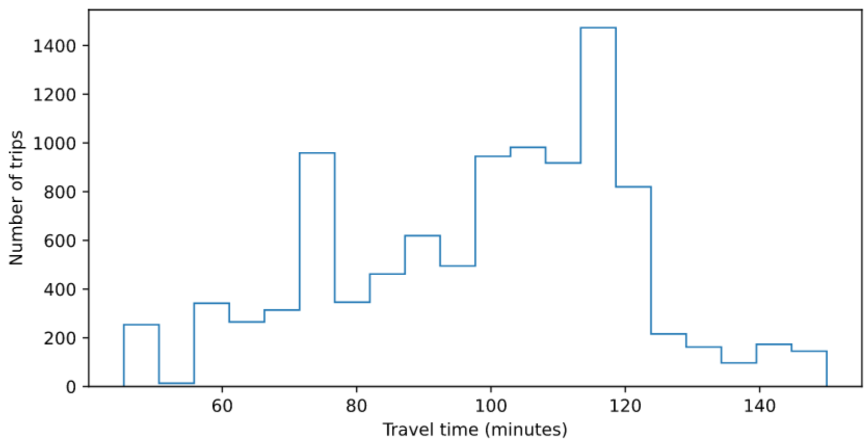

Figure 3.9: Output example: distribution of trip-level travel time.

3.5 DISCUSSION

This section presented a residual-demand based traffic model framework. It has the capability of introducing temporal dynamics yet still capable of taking into account the trips that cannot finish in one assignment period. This framework is especially applicable for large networks with temporal output requirements, where fully dynamic assignment with optimized routing is too computationally intensive to be carried out. The above framework is not without problems. For example, the CH routing algorithm implementation is still time-consuming on a large road network, which limits the numbers of CH operations that can be performed. In other words, only a pseudo-equilibrium traffic distribution is achieved, as strict equilibrium assignment would require iteratively updating the routes and running the CH operations many times.

In addition, the selection of the stopping node in the residual demand calculation is also a simplified process, where the route traversal time is estimated based on the traffic flow in the previous assignment using the BPR curve. This may under- or over-estimate the link travel time if the differences between the travel demand in the two consecutive assignment period is large. This issue can be overcome with the introduction of the network loading module using dynamic simulation models, such as SUMO (Lopez et al., 2018), MATSim (German Aerospace Center (DLR), 2021) or Mobiliti (Troutman, 2019).

4 Case Study

4.1 INTRODUCTION

In this section, the ability of using a collection of existing and newly developed city-scale simulation tools into a framework of post-earthquake regional infrastructure performance assessment is demonstrated. The workflow begins with earthquake selection and ground-motion generation, supports water shortage analysis and building damage assessment, and finalizes with traffic performance evaluation. Inter-dependencies between these complex systems are quantified through controlled experiment simulations. The workflow of the case study is summarized in Figure 4.1.

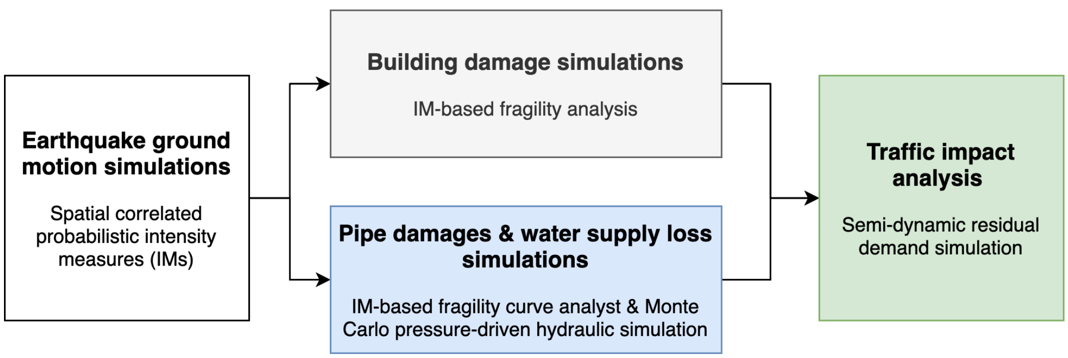

Figure 4.1: Conceptual workflow of the case study.

A probabilistic seismic hazard analysis (PSHA) was adopted herein as the general approach to simulate earthquake risk for the study area, the San Francisco Bay Area. The considered earthquake events are similar to the USGS HayWired case study (Aagaard et al., 2017). Specifically, multiple M7.05, Hayward-Rodgers Creek HN+HS earthquake rupture events realizations from UCERF2 (Working Group on California Earthquake Probabilities(WGCEP), 2008) were simulated using the ground-motion prediction equations (GMPEs) from Boore and Atkinson (2008). Since the study focused on earthquake risk assessment of spatially distributed infrastructure system, spatial correlation of intensity measures (IMs) (PGA and PGV) between different sites were modeled using the method developed by Jayaram and Baker (2009).

The potential earthquake impact on a WDN was modeled as follows: (1) using the simulated earthquake ground-motion IMs (PGV), the probability of failure for each network component was estimated using the pipeline fragility curves; (2) based on the estimated failure probability, certain components were sampled as the failed component with corresponding damaging degrees; and

(3) a pressure-dependent (PDD) hydraulic simulation was performed on the damaged network to estimate the water supply shortage across the selected study region. A Monte Carlo (MC) simulation was used to deal with uncertainties from different ground-motion scenarios. The newly developed WDN hydraulics program, HydrauSim, was used to perform hydraulic simulations on damaged networks.

In addition to the WDN analysis, the damage states of 1.8 million buildings post-event across the San Francisco Bay Area were simulated using the SimCenter rWhale software (Elhaddad et al., 2019). With detailed building information and site-specific ground motions, rWhale evaluates the seismic performance of buildings using the FEMA P-58 method, in which a nonlinear structural dynamic analysis is performed to obtain the engineering demand parameters (EDPs), such as lateral drifts, accelerations, etc., caused by seismic ground motions. Spatial distribution of the simulated red-tagged buildings in the study area after the hypothetical earthquake is presented.

The regional impacts of earthquake-induced WDN and building damage are tied together through traffic simulations. Specifically, damaged water pipes are assumed to affect road connectivity, either due to flooding or the presence of heavy repair work that blocks the roads. Building damage is assumed to affect travel demand as residents cannot live or work in red-tagged buildings. Their normal traffic patterns are either disrupted or eliminated proportionally according to the percentages of red-tagged buildings in a census tract (the smallest unit of the travel demand data). In addition, the capacity of the Bay Bridge is also assumed to be affected by the earthquake. Temporal changes in the traffic system performance were simulated in the study, which include losses in the traffic system performance at different stages of the earthquake events (before, immediately after, halfway recovered, and fully recovered). Inter-dependencies between the WDN, buildings, and traffic are discussed in the end.

4.2 EARTHQUAKE GROUND-MOTION INTENSITY GENERATION MODEL

The first step in an earthquake hazard analysis is to acquire the earthquake-induced ground-motion intensity data for the study area. Since this study was aimed at hypothetical earthquake hazard scenario testing, simulated ground-motion intensities were used instead of real data. This research adopted PSHA as the general approach on simulating earthquake risk for the San Francisco Bay Area to quantify uncertainties of earthquake events and combine them to produce an explicit description of the distribution of future shaking that may occur at a site. Hence, PSHA provides more comprehensive risk assessments than a simple deterministic approach (Baker, 2008). The principle equation for PSHA is presented by Equation 4.1.

$$P(IM) = \sum_{i=1}^{n_{sources}} P(M_i > m_{min}) \sum_{j=i}^{n_M} \sum_{k=1}^{n_g} P(IM|m_j, r_k) P(m_j) P(r_k) \tag{4.1}$$

where $P(IM)$ is the probability distribution of an earthquake IM; $P(M_i > m_{min})$ is the probability of a given earthquake source capable of producing rupture magnitude larger than a threshold (m_{min}); $P(IM|m_j, r_k)$ is the probability distribution of an IM value given the rupture magnitude and the distance from the epicenter; and $P(m_j)$ and $P(r_k)$ represent the probability distribution for rupture magnitude and distance for an earthquake, respectively.

In Equation (4.1), the probability distribution of an IM for a site or location, $P(IM)$ is calculated by summing up uncertainties on earthquake source ($\sum_{i=1}^{n_{sources}}$); uncertainties on the magnitudes of an earthquake ($\sum_{j=1}^{n_M}$); and uncertainties on the locations of an earthquake ($\sum_{k=1}^{n_g}$). This study selected a set of specific earthquake rupture events with a given magnitude that followed assumptions similar to the U.S. Geological Survey (USGS) Haywired case study (Hudnut et al., 2018): i.e., the uncertainties on earthquake sources and earthquake magnitude were not considered in this case and only the distance uncertainty remains. Therefore, Equation 4.1 is reduced to Equation 4.2.

$$P(IM) = \sum_{k=1}^{n_g} P(IM|r_k)P(r_k) \tag{4.2}$$

The region of interest covers most of the major populated areas in the San Francisco Bay Area; see Figure 4.2. Specifically, a bounding box area (-123.52544, -121.21856, 36.904645, 38.8581786) was generated that contained the San Francisco Bay Area, with a 2 km by 2 km grid of simulation points following Aagaard et al. (2017). Grid points that fall into the sea or non-populated areas were removed for computational efficiency. In total, 5709 grid points remained for ground-motion simulations. Although this case study shares many similarities to the HayWired case (study area, rupture fault, rupture magnitude, etc.), there are several ways in which they are different:

1. The rupture configurations are different. The HayWired case study considered an M7.05 earthquake scenario (HS+HN G04 HypoO) from a suite of 39 scenario earthquakes for the Hayward fault developed by (Aagaard et al., 2010b). The study case herein used an M7.05, Hayward-Rodgers Creek HN+HS earthquake rupture event from UCERF2 (Working Group on California Earthquake Probabilities(WGCEP), 2008).

2. The current case does not fix the epicenter of the earthquake, whereas the HayWired case study has its epicenter in Oakland. Having variances on the earthquake epicenter location allows exploring infrastructure systems responses under different spatially distributed ground motions.

3. The ground-motion simulation models are fundamentally different. The HayWired case uses a three-dimensional (3D) numerical simulation to solve the wave equation using the USGS Bay Area Seismic Velocity Model 08.3.0 (Aagaard et al., 2010a) for the properties in the 3D volume. Herein, the PSHA computation framework, OpenSHA (Field et al., 2003) is used, with spatial correlation considerations for earthquake IMs generation. Although PSHA lacks simulation precision compared to the 3D numerical modeling, it requires fewer computation resources and input information, e.g., slip distribution, hypocenter, and the geological model of the study area. This makes feasible the exploration of many earthquake scenarios with different epicenter locations.

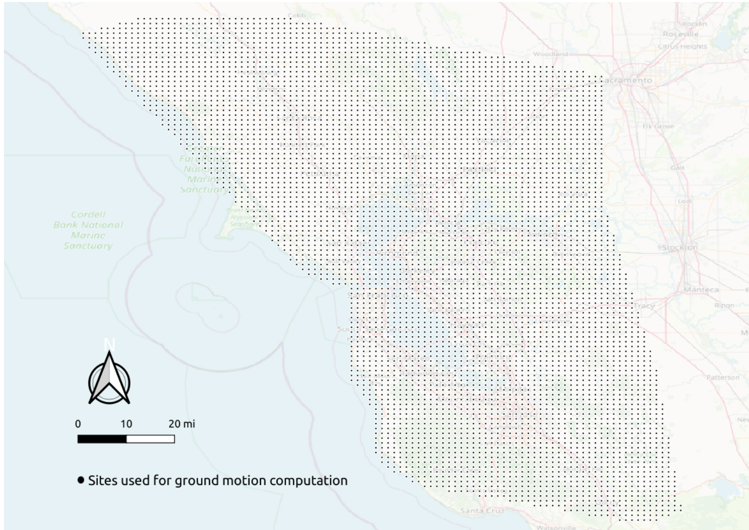

Figure 4.2: Study area for the ground-motion simulation. Black points indicate grid points (sites) for the earthquake ground motion simulation model.

OpenSHA is an open-source framework that provides a flexible community-modeling environment for the development and testing of a seismic hazard analysis (SHA) algorithm (Field et al., 2003). The fundamental framework for OpenSHA is shown by Figure 4.3. It requires the selection of earthquake IMs, study sites list, the IM relationship (i.e., GMPEs), and an earthquake-rupture forecast model. The earthquake IMs used in this study were PGA and PGV. The simulated PGA was used to analyze earthquake hazards on buildings, whereas PGV was used to quantify earthquake damages on WDNs. As mentioned previously, 5709 grid points were simulated for this study; see Figure 4.2. The earthquake-rupture forecast model, UCERF2 (Working Group on California Earthquake Probabilities(WGCEP), 2008), was used to generate the earthquake rupture events (M7.05, Hayward-Rodgers Creek HN+HS). The GMPEs from Boore and Atkinson (2008) were used for the IM relationship. The time-averaged shear-wave velocity from the surface to 30 m (V_{s30}) was assumed to be constant as 760 m/sec.

Since this study focused on earthquake risk assessment of spatially distributed infrastructure systems, spatial correlation of PGA and PGV between different sites needed to be explicitly modeled (Lee and Kiremidjian, 2007). Hence, the simulated site-specific IMs provided by OpenSHA were corrected with spatial correlations using the method from Jayaram and Baker (2009). Specifically, semi-variogram was used as the geostatistical measure to model the ground-motion correlation with the simulated medians and standard deviations of IMs from the ground-motion model (OpenSHA in this case) as input. Modeling spatial correlations between the IMs also mitigated the “median map problem” (lacking variances on IMs) of PSHA, which has been criticized in the HayWired case study (Hudnut et al., 2018).

Using the method described above, 100 ground-motion scenarios of the M7.05, Hayward-Rodgers Creek HN+HS earthquake rupture events were generated for the study region. Each scenario included both PGA and PGV estimations for all simulated sites with spatial correlation considerations. Figure 4.4 shows the distribution of the average value (across all simulated sites for

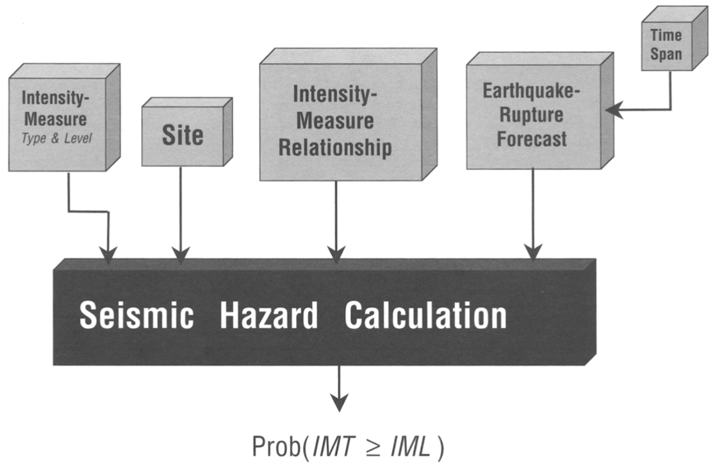

Figure 4.3: The fundamental elements needed for conducting an earthquake hazard calculation in OpenSHA (Field et al., 2003).

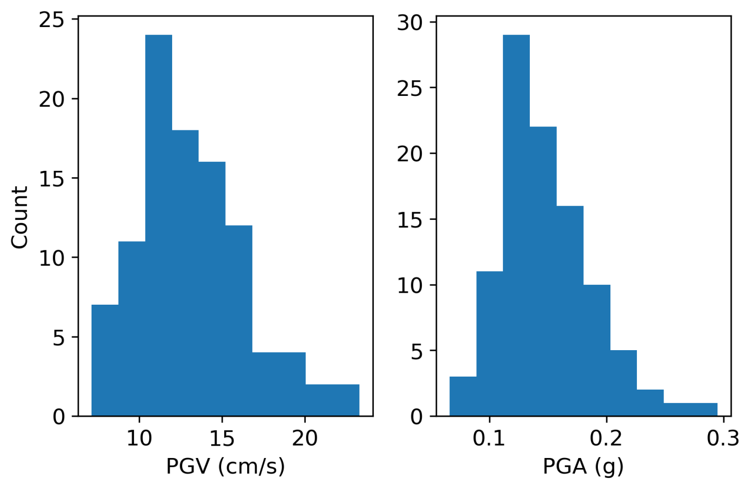

Figure 4.4: Distribution of the mean values of IMs (over all simulated sites for each realization) for 100 earthquake scenarios.

each scenario) of PGA/PGV for the 100 scenarios. The range for the simulated mean PGV of the study area is from 9 to 22 cm/sec, with a mean value around 13 cm/sec. The range for simulated mean PGA is from 0.05 to 0.28g, with a mean value around 0.14g. According to the Modified Mercalli Intensity table (Wald et al., 1999), this means that most of the study area will experience degree VI or higher earthquake intensity level for most scenarios, signaling the potential for moderate to high damage to occur. To validate the simulation result, the simulation realizations were compared with the ground-motion map from the HayWired study. When simulated epicenter locations are close to Oakland, the ground-motion simulation results of this study match the ground-motion simulation map produced by the HayWired case study. For these two cases, a comparison between Figure 4.5 with Figure 4.6 demonstrates that both the PGV magnitude range and corresponding spatial distribution match closely.

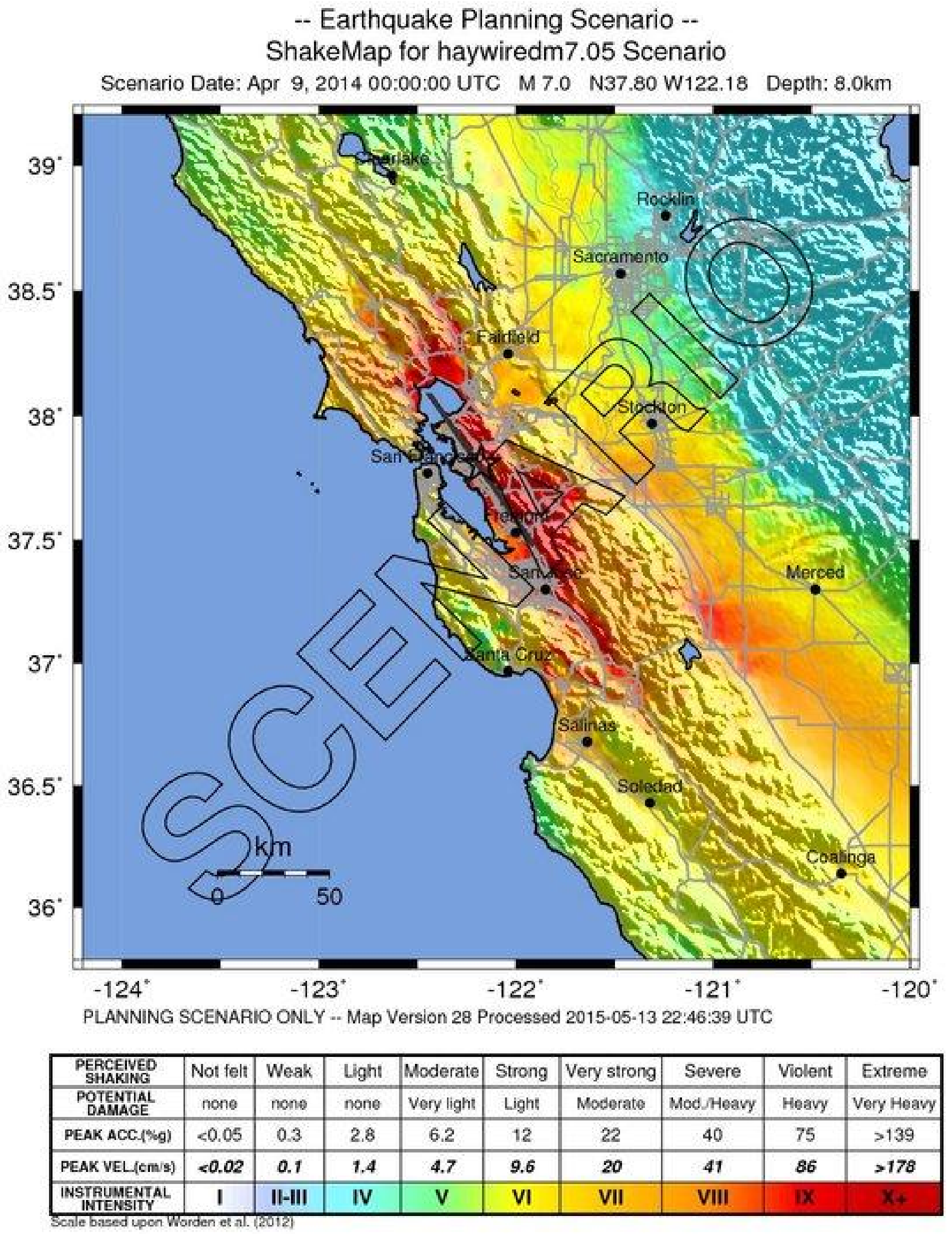

Figure 4.5: Ground-motion intensity map of the HayWired case.

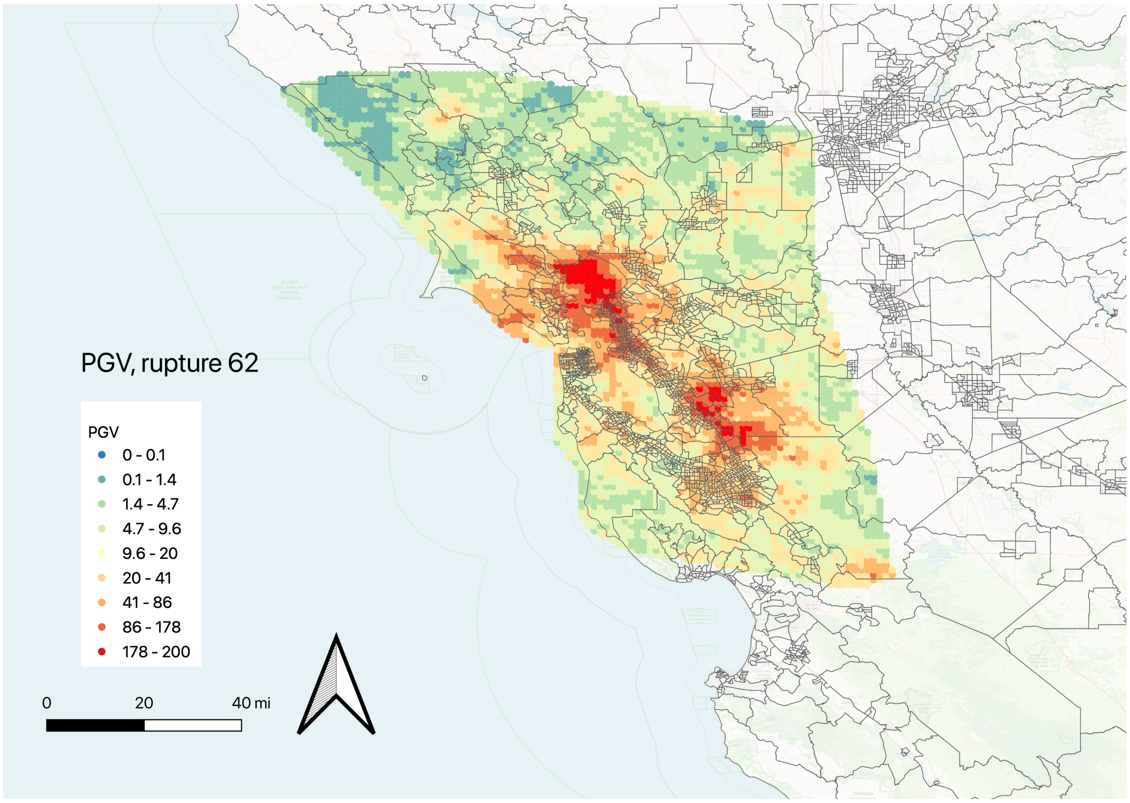

Figure 4.6: Ground-motion intensity map of a selected simulation scenario.

4.3 WATER DISTRIBUTION NETWORK

4.3.1 Introduction and Background

Past earthquakes, such as the Northridge earthquake (1994) and the Kobe earthquake (1995), caused significant damage to the WDN (Yoo et al., 2016a). In the case of the Kobe earthquake, 23 instances of damage occurred in the main waterline, resulting in disruption of drinking water supply to approximately 15 million people (Yoo et al., 2016a). Clearly, understanding and quantifying the potential impact of a major earthquake on regional WDNs is critical to characterizing the potential risk of the earthquake. In collaboration with the East Bay Municipal Utility District (EBMUD), this study assessed the potential earthquake damage of the WDN in the east San Francisco Bay Area. Specifically, the earthquake impact to EBMUD's Central Pressure Zone—a major distribution zone—was considered. This zone covers many major cities in the East Bay (Richmond, Berkeley, Oakland, Alameda Island, San Leandro, and part of Hayward); see Figure 4.8.

The EBMUD gravity-feed zone consists of 65,700 distribution pipes with a total length of 1368 miles (2201 km). The properties of pipes are shown by Figure 4.7. The majority (98.4%) of the pipes are less than 600 ft long, and the minimum, mean, and maxiumum pipe lengths are 1 ft, 109 ft, and 2711 ft, respectively. Table 4.1 listed the pipe materials used in the EBMUD network. The majority of pipes are made with cast iron (CI) and asbestos cement (AC), which

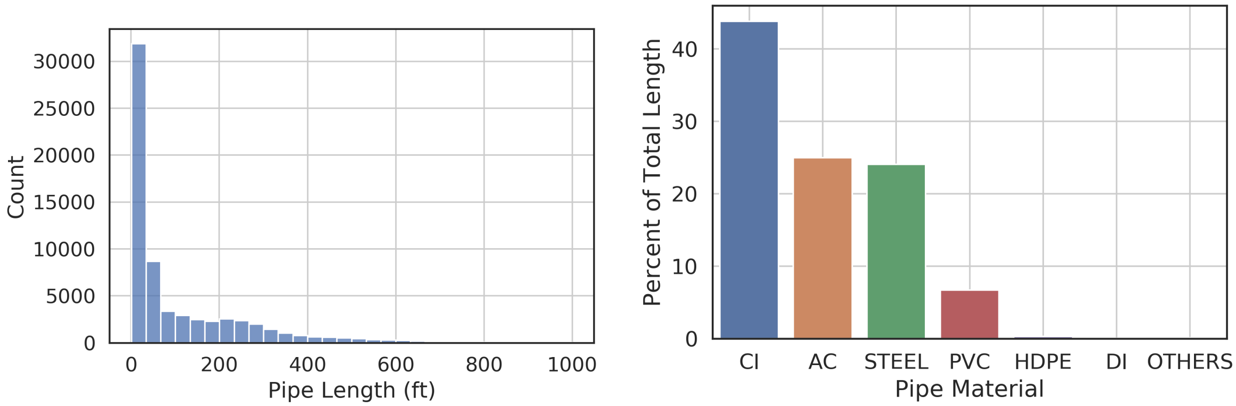

(a) Pipe length distribution

(b) Pipe material distribution

Figure 4.7: Pipe properties of the study region: (a) pipe-length distribution of the study area; and (b) pipe-material distribution of the study area.

Table 4.1: Material types and their abbreviations.

Abbreviation	Description
CI	Cast Iron
Steel	Steel
AC	Asbestos Cement
PVC	Polyvinyl Chloride
HDPE	High Density Polyethylene
DI	Ductile Iron

make up around 70% of pipes in the system. Steel and PVC pipes also exist; pipes made with other materials are rare in the system. The roughness coefficient values for the pipes are provided by EBMUD.

The averaged annual day demand for the year 2018 was used for this service area, which is around 50,000 gallons per minute (GPM) in total. The service zone is supplied by seven control stations located at the boundary of the service zone, which are shown as red stars in Figure 4.8. The control stations are located at relatively high elevations (Figure 4.9) to ensure a sufficient water supply for the rest of the system. The hydraulic heads for the sources are set at 150 ft, which satisfies all the demand in this area before the hazard occurs. In this study, pumping operations were not considered since the major driving force for water distribution in this service zone is gravity. Compared to the empirical equation based WDN resilience model by Porter (2018) in the HayWired case study, the current model is based on hydraulic simulation of the damaged network using HydrauSim. Moreover, a stochastic simulation process was adopted in this study to evaluate WDN responses considering earthquake ground-motion uncertainties.

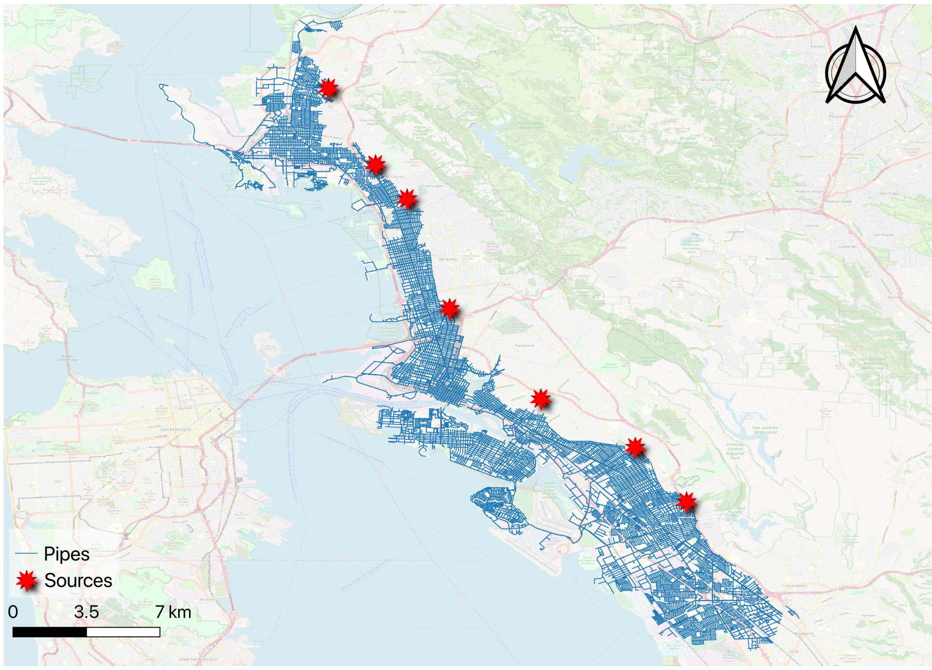

Figure 4.8: Water distribution network used for the study.

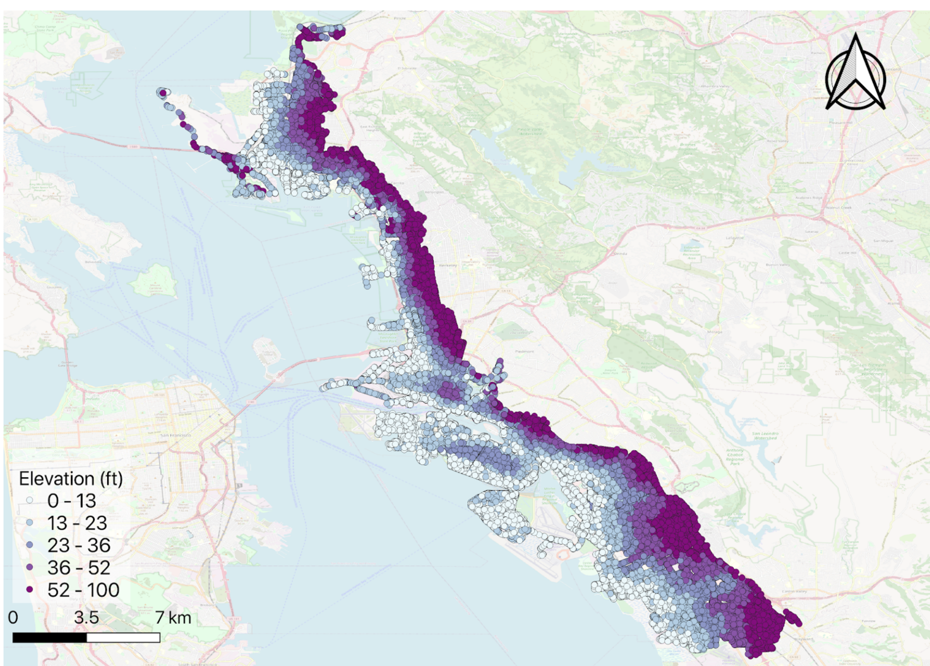

Figure 4.9: Elevation map of the study area.

4.3.2 Methodology

The potential earthquake hazard on a WDN is modeled as follows:

1. Using the simulated earthquake ground-motion IMs (PGV), the probability of failure for each network component is estimated using the pipeline fragility curves.
2. Based on the estimated fail probability, certain components were sampled as the failed component with the corresponding degree of damage.
3. A PDD hydraulic simulation was performed on the damaged network to estimate the degree of water supply shortage anticipated for the study case.

This procedure is summarized in Figure 4.10.

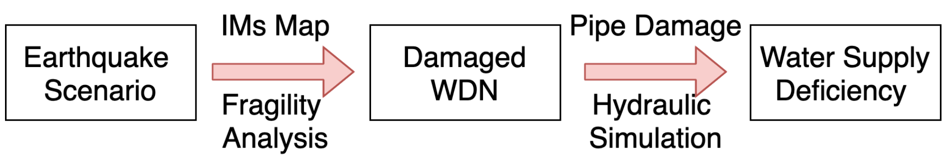

Figure 4.10: Earthquake hazard analysis procedure for a WDN.

Similar to the assumptions made by Porter (2018), this study considered only buried distribution pipes as potential fail components. Unlike other critical WDN components such as tanks and reservoirs, not many buried distribution pipes were included in the seismic improvement programs due to economical considerations, which make them especially vulnerable to earthquake impacts. The failures of other vulnerable WDN components—such as pumps—were not considered because the region under study relies on a gravity feed zone where pumps are not required. Following Alliance, AL (2001), an earthquake-induced buried pipe failure event was modeled as a Poisson process given the selected ground-motion level and pipe properties, which can be expressed by Equation 4.3.

$$P_{f,i} = 1 - e^{-RR_i L_i} \tag{4.3}$$

where $P_{f,i}$ represents the probability of failure for pipe i; L_i is the length of pipe i; and RR_i is the repair rate for pipe i modeled by Equation 4.4 (Alliance, AL, 2001).

$$RR_i = k_1(0.00187)PGV_i \tag{4.4}$$

k_1 is the fragility constant, which is dependent on the pipe material, diameter, and other properties. The list of k_1 values used in this study is presented in Table 4.2. PGV_i is the simulated PGV for site i. Note that the ALA vulnerability function for permanent ground deformation was not considered in this study due to the lack of soil data.

Table 4.2: Fragility constant for different pipes.

Pipe Material	Diameter	K
Cast Iron	small	1.0
Ductile Iron	small	0.5
Asbestos Cement	small	1.0
PVC	small	0.5
Welded Steel	small	0.9
Welded Steel	large	0.15

Each PSHA earthquake ground-motion scenario contains the simulated PGV values for every simulation grid point; see Figure 4.2. The PGV value for each pipe is estimated by mapping the center of the pipe to the spatially closest simulation grid point. Since PGV values do not vary significantly over small distances, this closest-point mapping method provides a simple yet reasonable estimation for the PGV values of individual pipes. The estimated pipe failure rate for a given pipe can be calculated using Equations 4.3 and 4.4. This study ignored those pipes with an extremely small probability of failure probability ($P_{f,i} < 0.0001$) because the total number of pipes for the study area is at the magnitude of $10,000$. After removing these pipes, group sampling on the remaining pipes was proposed to approximate the spatial distribution of damaged pipes. Specifically, the remaining pipes were grouped into 10 bins according to the simulated fail probability (with non-likely fail pipes removed) to reduce the variances and for computation convenience. Within each group, the expected number of pipes to fail is estimated using Equation 4.5.

$$N_{i,fail} = P_{i,fail} * N_i \tag{4.5}$$

where $N_{i,fail}$ is the expected number of pipe failures in group i; $P_{i,fail}$ is the probability of fail within group i, which is estimated as the mean probability of fail for this group; N_i is the total number of pipes in group i.

Using Equation 4.5, pipes (uniform sampling) are randomly selected to fail for all 10 subgroups. Combining the sampled pipe failures from each group gives which pipes are expected to fail for the whole network. The damaged degree for each pipe failure is modeled by the leak-hole diameter or the equivalent orifice diameter (EOD) for the pipe(Shi et al., 2006). According to HAZUS (FEMA, 2012), 80% of pipe damage is assumed as leaks, and 20% is assumed as breaks. For leaking pipes, the EOD is randomly assigned between 5% and 25% of the pipe diameter (Shi et al., 2006). For broken pipes, the EOD is chosen as 80% of the pipe diameter to approximate heavy water loss due to broken pipes. The damaged network is then summarized into a .inp (EPANet input file format) file, and HydrauSim is used to simulate the steady-state hydraulic of the damaged WDN.

Since both the exact pipe failure locations and the corresponding degree of damage is uncertain, a Monte Carlo simulation was considered for this study. Specifically, for each earthquake scenario, 500 different damaged network scenarios were generated and simulated using HydrauSim. The final hydraulic simulation result was obtained through averaging the hydraulic measure of the water shortage ratio for every damaged network scenario. Figure 4.11 summarizes the WDN hazard analysis workflow for a given earthquake scenario.

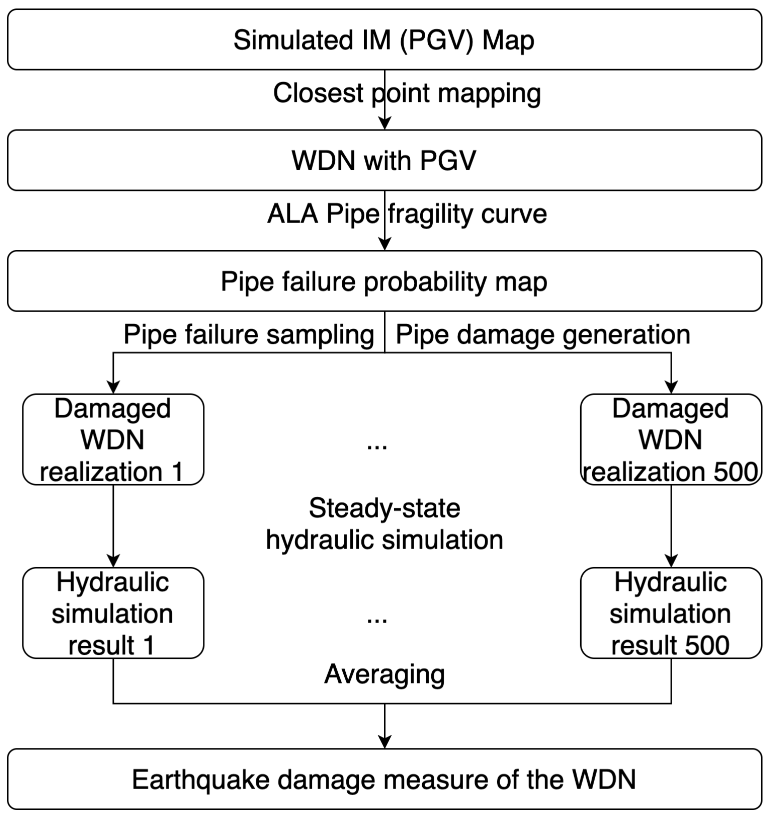

Figure 4.11: WDN hazard analysis workflow for a simulated earthquake scenario.

4.3.3 Results and Discussion

Figure 4.12(a) shows that as the level of ground movement (mean PGV) increases, more pipes tend to break. For the 100 earthquake ground-motion scenarios produced by the PSHA model, the minimum number of expected pipe breaks is 56 (corresponding to mean PGV 7.5 cm/sec), and the maximum number of pipe breaks is 752 (corresponding to mean PGV of 18 cm/sec). On average, 242 number of pipes in the study area were considered broken. The HayWired study (Porter, 2018) reported 2037 pipes might be damaged by the earthquake mainshock wave passage for the entire EBMUD network (6698 km). Converting the damage number to the scale of the EBMUD gravity feed zone, around 600 pipes will be damaged based on the HayWired report estimation, which falls into the range of 56–752 damaged pipes obtained by this study. Comparing the number of pipe breaks in the HayWired study to the number of pipes obtained in this study (around 65,000), the number of pipe failures is small. As discussed below, even a small number of pipe failures may have a noteworthy impact on demand.

Although Figure 4.12(a) shows a clear correlation between mean PGV value (average across all simulated sites for each scenario) and the number of pipe failures (marked by the red line), variations on the number of broken pipes for a certain mean PGV value can still be observed. This is because the mean PGV value as an aggregated measure does not reflect the spatial variances of the ground-motion intensities. For example, one earthquake scenario may have a larger mean PGV value than another case, but the severe ground shaking (high PGV values) in the region occurred in non-populated areas, resulting in fewer broken pipes, which has a higher ground-motion intensity compared to populated areas.

This is illustrated in Figure 4.12(b). As the mean PGV value of the study area increases, the number of pipes with large PGV values increases. Moreover, note the large variances of the numbers of pipe breaks with a given mean PGV range, demonstrating the spatially heterogeneous distribution of PGV values across different realizations. Moreover, differences in material and length across network pipes also contribute to the variations of number of pipe failures since they are important factors in the fragility function; see Equations 4.3 and 4.4). Figure 4.13 shows a map of both the PGV level experienced by the pipes and the resulting probability of pipe failure for the region of study of one earthquake scenario. In general, the high PGV value of the region tends to have a high probability of pipe failure; the region chosen as an example is the city of Berkeley. The variations of the intrinsic properties of the pipes are also reflected by the variations in the probability of pipe failure within the area with similar PGV values.

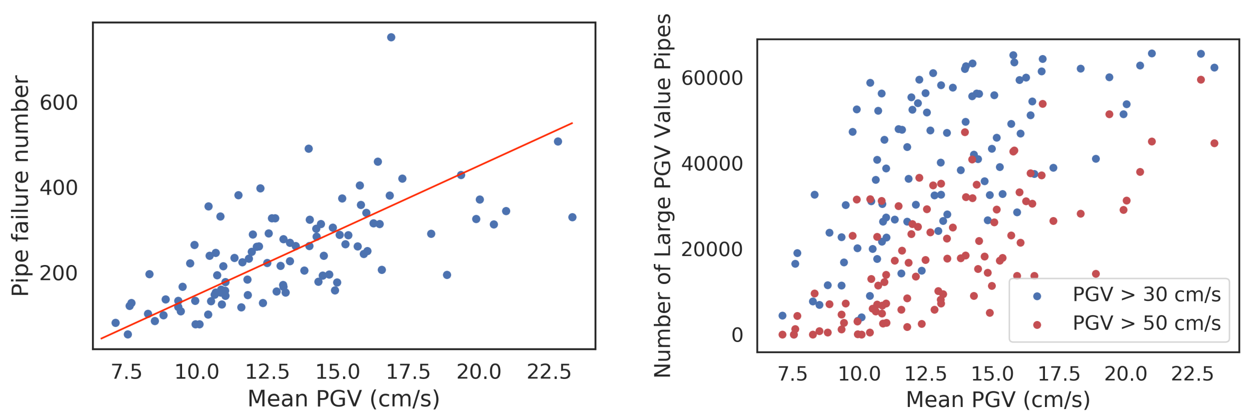

(a) PGV level of pipes

(b) Pipe fail probability

Figure 4.12: WDN response to ground motion inputs; (a) simulated number of pipe failures for all 100 earthquake ground-motion scenarios with respect to mean PGVs; and (b) number of pipes experiencing large PGV values for all 100 earthquake ground-motion scenarios.

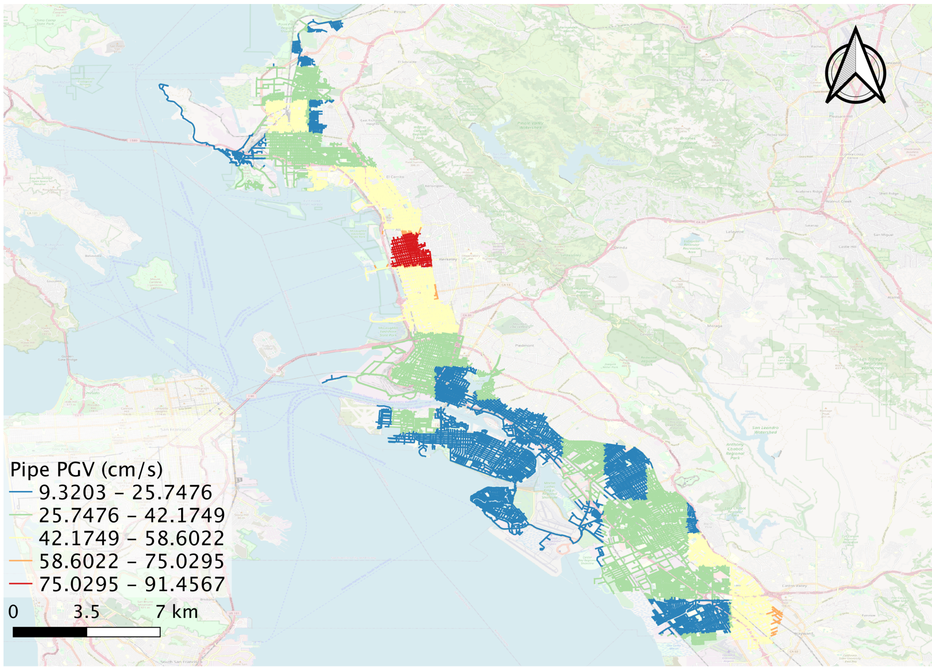

(a) PGV level of pipes

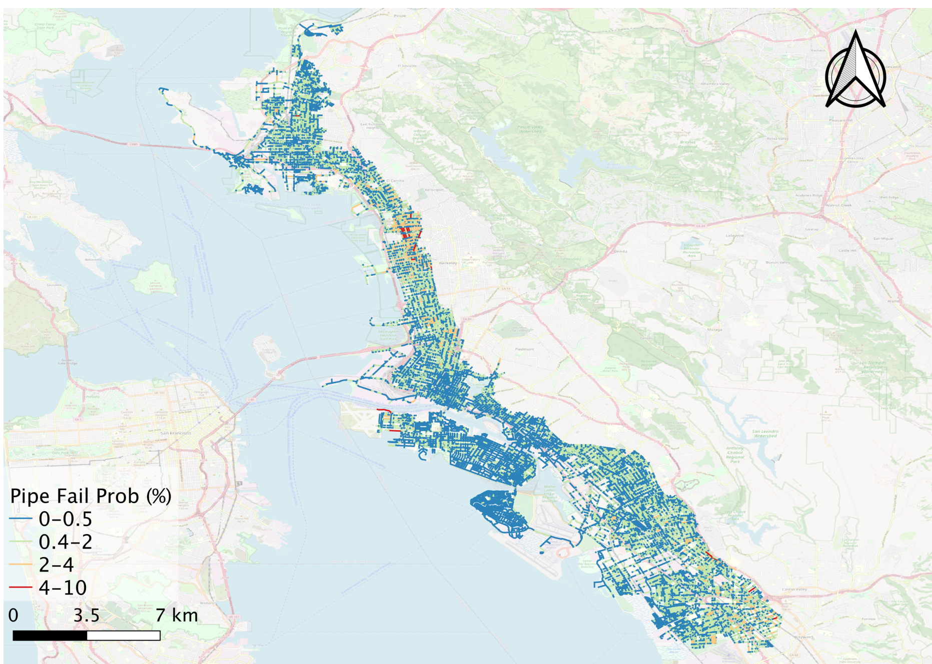

(b) Pipe fail probability

Figure 4.13: Earthquake potential impacts on a WDN: (a) interpolated PGV level for each pipe; and (b) the resulting map of probability of pipe failures using the fragility curve from Alliance, AL (2001). The shown case has a mean PGV value of 13.06 cm/sec, and the average number of pipe breaks determined from the simulation is 167.

To quantify the consequences of the earthquake to the WDN, Monte Carlo simulations were performed based on the generated pipe failure map for each earthquake scenario. The result is summarized in Figure 4.14. Each point on the plot represents a single earthquake scenario. Figure 4.14(a) shows the relationship between the mean PGV value of a scenario and the resulting total water shortage ratio, which is defined by Equation (4.6).

$$S_{tot} = \frac{(demand_{tot} - supply_{tot})}{demand_{tot}} * 100 \tag{4.6}$$

where S_{tot} is the total water shortage ratio for the WDN; $demand_{tot}$ is the total demand for the WDN; and $supply_{tot}$ is the simulated total supply for the WDN.

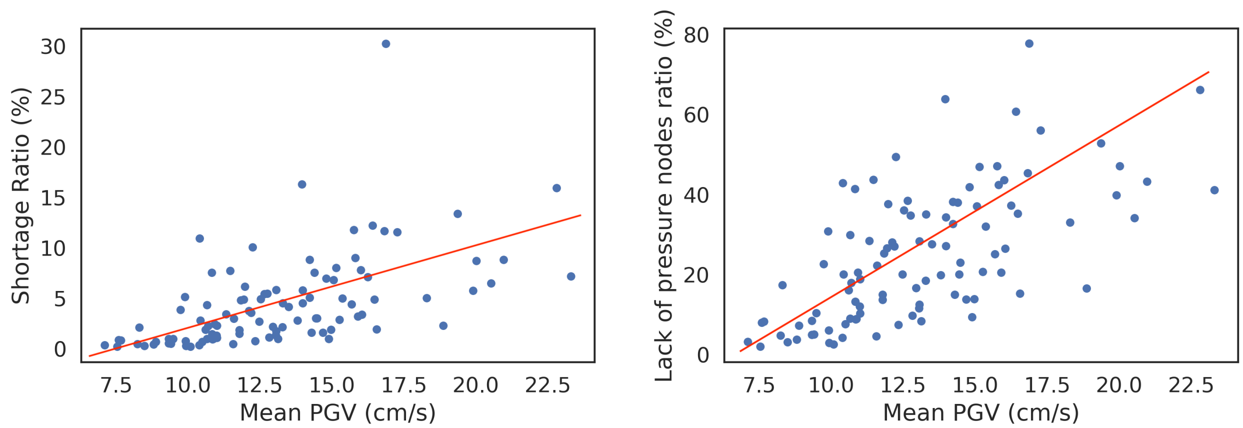

(a) (b)

Figure 4.14: Simulated hazard consequence for the WDN of 100 earthquake scenarios: (a) shows the total water shortage ratio for each scenario (depth of the hazard); and (b) shows the ratio of the number of demand nodes that are below normal operating pressure (width of the hazard).

A clear trend (see the red line on the figure) is noticeable in Figure 4.14(a) where the degree of total water shortage increases as the overall ground shaking level increases. The variations of the shortage ratio are caused by the variations of the number of pipe failures for a certain PGV value, as discussed previously. The minimum shortage ratio is only 0.234%, implying a limited earthquake impact on the WDN in some cases. On the other hand, the maximum shortage ratio is around 30%. On average, the total water shortage ratio is around 5%. Considering the small number of pipe failures generated by the simulation—around 0.45% from the total pipes—it is reasonable to conclude that the WDN performance is sensitive to strong ground motion. Although the total water shortage ratio measures the total severity of the earthquake impact on a WDN, it does not reflect how this disruption of the water supply is distributed among users. Hence, another measure, the lack of pressure nodes ratio, is used to capture the width (number of influenced demand nodes) from the earthquake on a WDN. As given by the following equation.

$$r_{lack} = \frac{(N_{tot} - N_{shortage})}{N_{tot}} * 100 \quad (4.7)$$

where r_{lack} is the lack of pressure nodes ratio; N_{tot} is the total number of nodes that experience demand, and $N_{shortage}$ is the number of nodes that experience pressure below normal operating conditions due to the damaged WDN. Insufficient node pressure often leads to water supply deficiency (see Chapter 2 for more detail). In this study, nodes with pressure less than 30 psi were defined as lack of pressure nodes. r_{lack} indicates the spatial impact of the earthquake on water supply for the region. Post-hazard actions, such as isolation valve closure due to inspection/maintenance, might cause water shortages for the impacted region.

Figure 4.14(b) shows a trend (see the red line on the figure) that the lack of pressure nodes ratio increases as the mean PGV value increases. Again, the variations are caused by the variations in the number of pipe failure for a certain PGV value. Compared to the total supply shortage ratio, the lack of pressure nodes ratio shows much more variations. For the simulated 100 ground-motion scenarios, the minimum lack of pressure nodes ratio is only 2%, but the maximum value reaches 77.77%. The average is about 24.98%.

Overall, the studied earthquake scenarios do not create a severe total water shortage when measured against the total supply quantity (5% on average). However, the width of the impact, which is measured as the number of demand nodes with insufficient water pressure, is huge. On average, about 25% of demand nodes may experience water shortages due to the lack of pressure, which can rise to 78% for the worst case scenario. The worst-case scenario estimation matches well with the HayWired report's assessment, which suggests that approximately 75% of services will be impacted after the earthquake event (Porter, 2018).

To further explore the relationship between the WDN damage state and the resulting water supply shortage, the number of pipe failures versus the total supply shortage ratio for all earthquake scenario realizations is plotted in Figure 4.15. One important feature is that the variance of the shortage ratio for a certain degree of pipe failures is small: the relationship between a pipe failure number and the resulting total water shortage ratio is nonlinear. Specifically, the trend is convex, i.e., the total water supply shortage ratio increases faster when the number of pipe failures increases. As the damage state of a WDN increases, users in the less-damaged region may experience severe water shortages due to water path blockages from severely damaged regions.

Two simulated scenarios are plotted to illustrate this phenomenon. Figure 4.16 represents a case with a moderate damaged state. The mean PGV value for this case is around 13 cm/sec, and the averaged simulated pipe break number is 167. A comparison between Figure 4.16(b) and Figure 4.16(a)demonstrate that the water supply shortages mainly occur on the damaged part of the network (top and bottom). Undamaged or lightly damaged parts of WDN do not experience a major supply shortage (middle part). Figure 4.17 shows a heavily damaged WDN case, where the number of simulated pipe breaks is around 750. When the WDN is severely damaged as a whole, all sections of the network may experience severe supply shortages regardless of local damage states. Figure 4.17(b) shows no obvious spatial pattern on the water supply shortages, whereas certain areas (bottom right) are expected to have more pipe breaks compared to other areas, as illustrated by Figure 4.17(a).

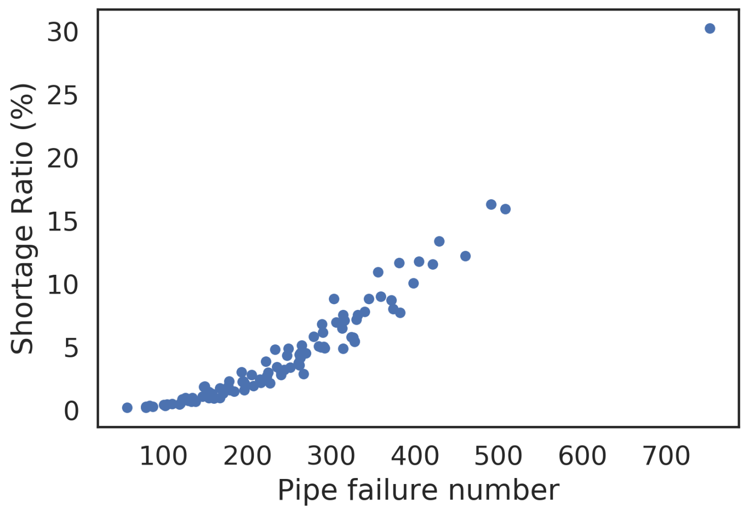

Figure 4.15: The relationship between the number of pipe failures and simulated total water shortage level for 100 earthquake scenarios.

Figure 4.18 shows the average simulated water shortage ratio across all 100 simulated scenarios. One noticeable feature of the averaged result is that the number of trivial impacted nodes (nodes that experience no or very small water supply loss) is very large, consisting 70% of the overall supply nodes. Note: this number is deceptive as spatial variances of the simulated water supply shortages are large across individual realizations, as previously discussed. Figure 4.18(b) shows that the relative standard deviation (RSD) of the simulated water shortage ratio is high across most of the study area, reaching over 100% (the standard deviation is bigger than the mean water shortage for most of the nodes) for some nodes. Moreover, nodes with small water supply shortage ratios tend to have larger RSD values compared to nodes with larger water supply shortage ratios. Such relationships implies that simulated scenarios agree on the locations of nodes experiencing severe supply shortage but not on the locations of minor impacted nodes. Hence, it is statistically meaningful to draw conclusions on high degrees of water shortage nodes but not on other nodes. Figure 4.18(a) shows that a high degree of water shortage nodes tends to group at certain parts of the network. The elevation map, Figure 4.9, shows that such clusters correspond to areas that are relatively high in elevation (i.e., the lower right corner). One can understand this phenomena by considering the energy change of the damaged WDN. Damaged WDNs tend to lose energy because of water leakages compared to the pre-hazard state. Thus higher elevations are more likely to lose water supply regardless of the actual distribution of the damaged pipes due to energy concerns.

4.3.4 Limitations and Future Studies

This study was limited in several ways. First, the study area of WDNs herein does not cover the whole San Francisco Bay Area. Instead, the study focused on the Central Pressure Zone, which covers major populated cities in the East San Francisco Bay Area and provides water services for almost half of the EBMUD's customers. Network data outside the EBMUD management area

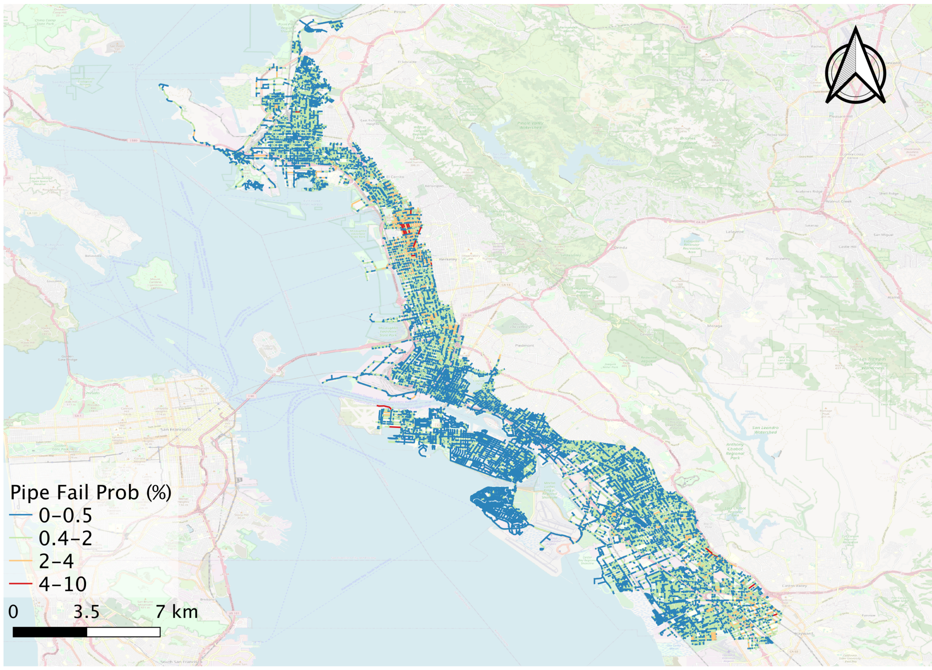

(a) Pipe fail probability

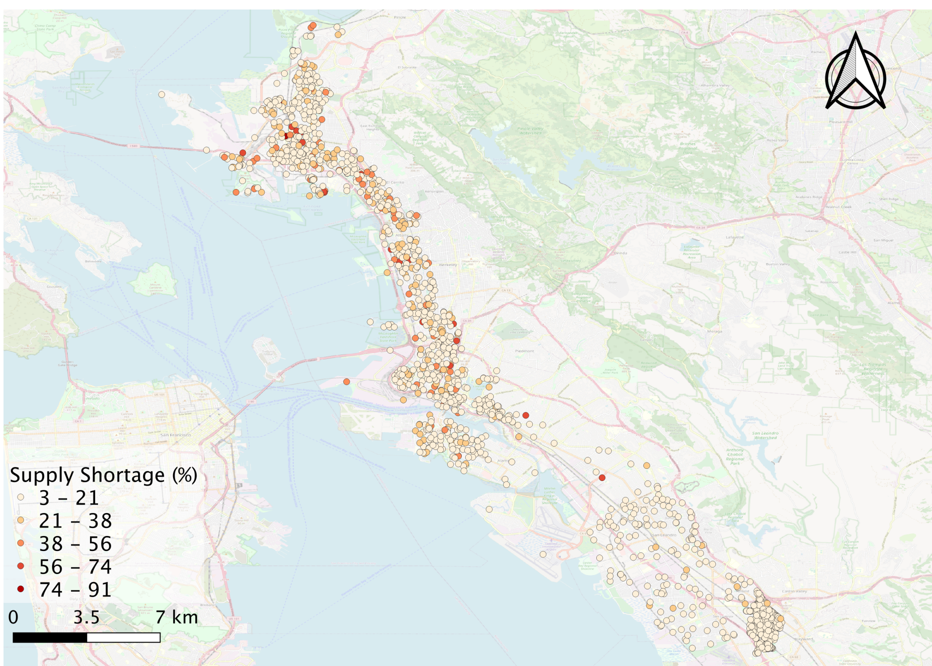

(b) Demand shortage

Figure 4.16: Pipe failure rates and simulated water shortages for a medium damage-level earthquake scenario, which has a mean PGV value 13.06 cm/sec and averaged simulated pipe break number 167.

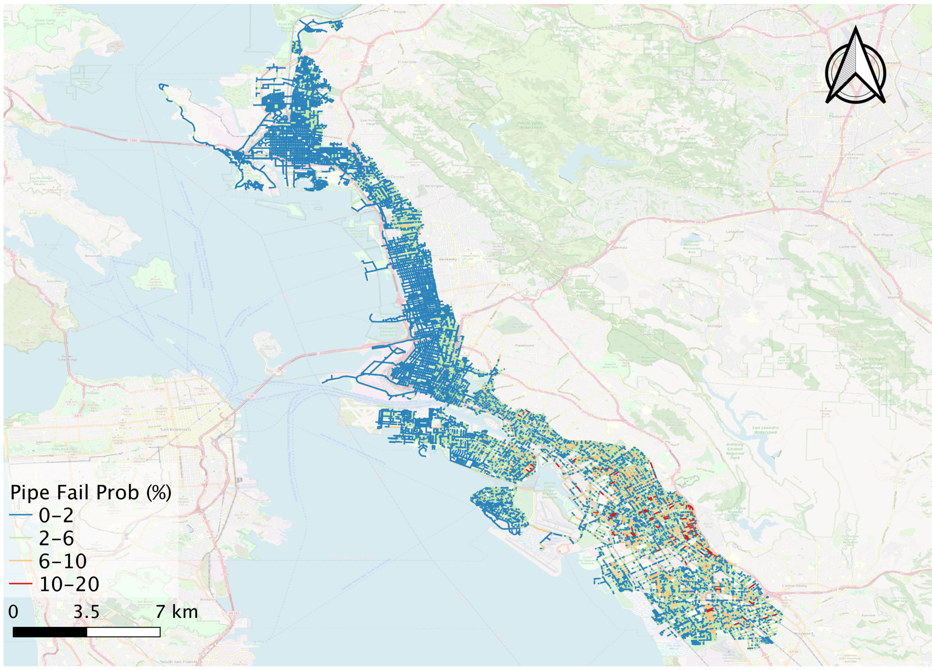

(a) Pipe fail probability

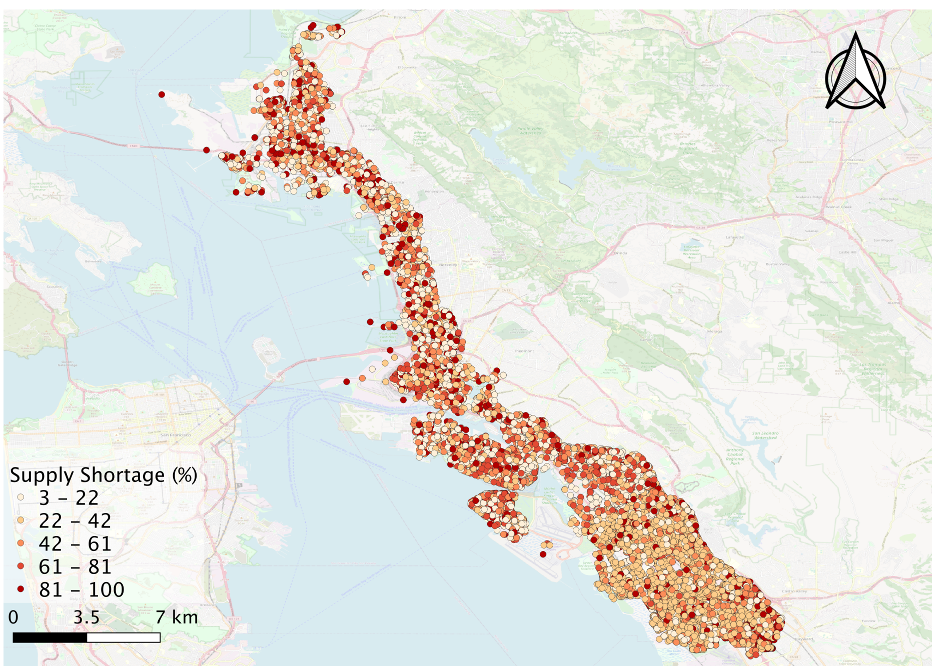

(b) Demand shortage

Figure 4.17: Pipe failure rates and simulated water shortages from a large damage-level earthquake scenario, which has a mean PGV value of 16.87 cm/sec and averaged simulated pipe break number 752.

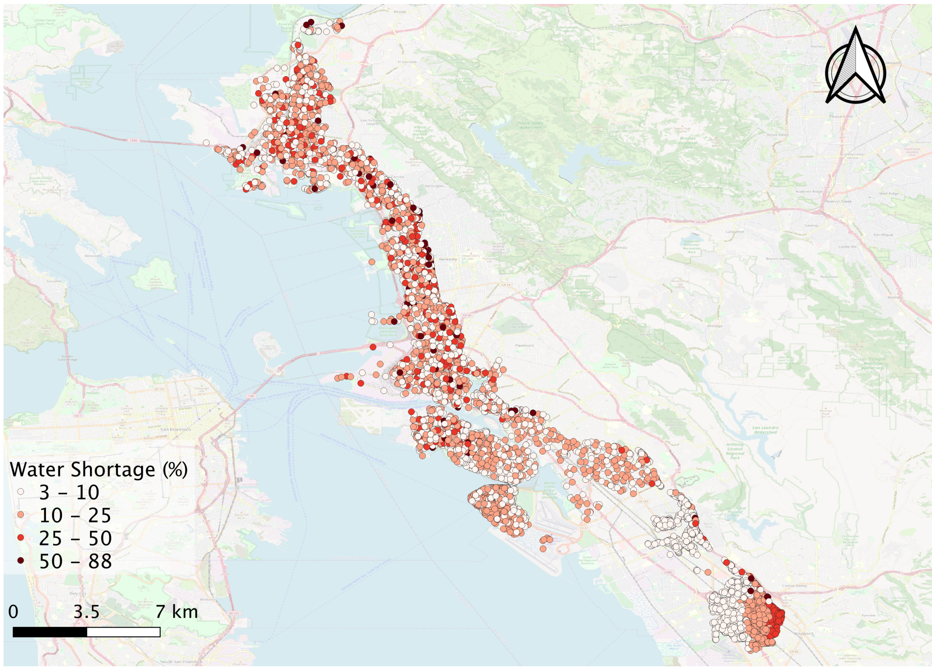

(a) Average simulated water shortage ratio

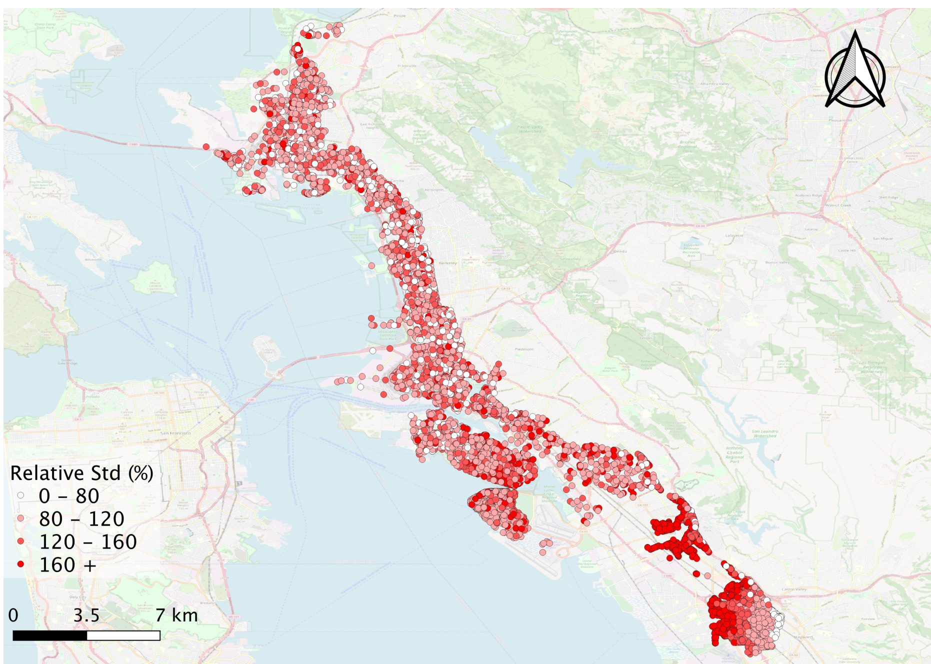

(b) Relative standard deviation ratio

Figure 4.18: Aggregated results from all earthquake scenarios; (a) Average simulated water shortage ratio across 100 scenarios simulations; and (b) relative standard deviation ratio of simulated water shortage ratio across simulations. Note that supply nodes with trivial water supply shortage (smaller than 3%) are removed from the graph for visualization purposes.

has not been included. Future studies may include contacting other water utility companies to acquire network data to model the WDN systems for the whole Bay Area. Another limitation of this study is that only buried pipes were modeled as breakable. The reason for such simplification is that the fragility of sophisticated WDN components such as pumps and regulators depends not only on ground motions but also on the functionalities of other infrastructure systems, such as the power grid. In future work, the performance of other critical infrastructure after earthquakes should be considered to correctly model the fragility of other critical WDN components other than pipelines. The impact of isolation valve conditions on WDN performance after earthquakes should also be considered in future work. In the current study, water sources such as reservoirs, tanks, and water treatment plants were modeled as robust (i.e., their failure wasn't considered). This is usually a valid assumption considering the strict building codes and regular maintenance for these structures. That said, severe earthquakes may damage such structures in rare cases, causing a complete water supply loss for the region. Due to the severity of the consequences should failure occur, the fragility of water-source structures may require further study. This study did not model WDN damages due to permanent ground deformation because of the lack of data for soil profiles for the region. Hence, earthquake damage levels for the WDN may be underestimated. Future studies should explore the impacts of other earthquake properties to the WDNs, such as permanent ground deformation and aftershocks. Lastly, this study focused on quantifying the impact of an earthquake on the WDN. Modeling the restoration process after the earthquake for WDNs will be considered in future studies.

4.4 BUILDINGS

4.4.1 Introduction

In addition to earthquake hazard analysis of the WDN, this study estimated the impact of a significant seismic event on building systems of the San Francisco Bay Area. In addition to damaging infrastructure, large earthquakes may endanger lives and cause major economic loss. The direct ground shaking and secondary hazards such as landslides and liquefaction may damage buildings by crumbling above-ground structures and warping underground foundations (Deierlein et al., 2019, 2021). Therefore, in conducting regional earthquake risk analyses, it is important to evaluate the performance of the building system and its influence on other components of the whole community.

This section describes the process of building damage estimation under the tested earthquake scenarios for the San Francisco Bay Area. The estimation is performed using the rWhale framework (Elhaddad et al., 2019; Deierlein et al., 2020) developed at NSF's NHERI SimCenter. The rWhale framework consists of multiple parts of modular software connected to form a workflow for a specific analysis of assets under hazards. The focus of this study is on building system response to earthquake hazard, using the building response and damage modeling module rWhale. The following sections describe the input for the building response and damage module, and ground-motion IMs. Next, we introduce the basic characterization of the building response and damage model. The model is applied to the building inventory data of San Francisco Bay Area, and the simulation results are presented at the end of this chapter.

4.4.2 Regional Seismic Hazard Characterization and Modeling

The rWhale framework takes seismic ground-motion characterizations as the input for seismic damage and loss evaluation. The earthquake ground motions can be determined by a variety of methods, such as physics-based simulations and GMPEs; rWhale supports both of them. Physics-based simulation of the earthquake fault ruptures is a computation-intensive way to obtain ground motions. It provides a time history of the shaking at the ground surface and is suitable for simulation-based building damage analyses. Alternatively, GMPEs are the most conventional approach for seismic ground-motion characterizations. The equations take earthquake magnitude Mw and other parameters—such as site conditions and distance to the fault rupture—as input to calculate site-specific IMs of ground shaking. Typical ground motion IMs include PGA, PGV, spectral acceleration (SA), duration, etc. This study adopts the ground-motion models developed by Baker Group (Jayaram and Baker, 2009) at Stanford University to obtain realizations of IMs that preserve the spatial correlation within a region. Details on GMPEs modeling of the study area can be found in Section 4.2. As with the WDN analysis, 100 different ground-motion scenarios were generated for the region of study on a simulation grid; see Figure 4.2). For each building, rWhale searches for nearest IMs based on its location by interpolating IMs values on the grid.

4.4.3 Response and Damage Modeling

Building performance can be estimated following different approaches, depending on the level of detail of the building information, the type of ground-motion characterizations, and the desired modeling resolution. With detailed building information and site-specific ground motions provided, rWhale can evaluate the seismic performance of buildings using the FEMA P-58 method. A nonlinear structural dynamic analysis is performed to obtain the engineering demand parameters (EDPs), such as lateral drifts, accelerations, etc., that are caused by seismic ground motions. The calculated EDPs are then related to component damages by fragility functions. The component damage levels are aggregated to calculate the damage variable for the complete building.

An alternative approach for assessing building performance is the HAZUS-based method in which a single fragility function is employed to determine the damage variables of a building given the ground-motion IM. This approach relies on fragility functions developed for specific building types based on general semantic descriptions, such as age, material, construction type, and occupancy class. The case study presented herein adopted this approach.

The HAZUS method provides the evaluation of the probability of direct physical damage of general building stock at several severity levels. General building stock represents typical buildings of a given model building type designed to either High-Code, Moderate-Code, or Low-Code seismic standards, or not seismically designed (referred to as Pre-Code buildings). The severity of damage to structural and nonstructural components of a building is described by one of five damage states: None, Slight, Moderate, Extensive, and Complete. Damage states are defined differently for different building type. For example, the damage state for a light wood-frame structure is defined as:

- Slight Structural Damage: Small plaster or gypsum-board cracks at corners of doors, window openings and wall-ceiling intersections; small cracks in masonry chimneys and masonry veneer.

- Moderate Structural Damage: Large plaster or gypsum-board cracks at corners of doors, window openings; small diagonal cracks across shear wall panels exhibited by small cracks in stucco and gypsum wall panels; large cracks in brick chimneys; toppling of tall masonry chimneys.
- Extensive Structural Damage: Large diagonal cracks across shear wall panels or large cracks at plywood joints; permanent lateral movement of floors and roof; toppling of most brick chimneys; cracks in foundations; splitting of wood sill plates and/or slippage of structure over foundations; partial collapse of "room-over-garage" or other "soft-story" configurations; small foundations cracks.
- Complete Structural Damage: Structure may have large permanent lateral displacement, may collapse or be in imminent danger of collapse due to cripple wall failure or the failure of the lateral load resisting system; some structures may slip and fall off the foundations; large foundation cracks. Approximately 3% of the total area of W1 buildings with complete damage is expected to be collapsed.

Building damage functions are in the form of log–normal fragility curves that relate the probability of experiencing or exceeding a building's damage state given the IM. Each fragility curve is defined by a median value of the IM that corresponds to the threshold of the damage state and by the variability associated with that damage state. For example, the conditional probability of being in or exceeding a particular damage state, ds, given the IM, is defined by the function:

$$\mathrm{P[ds|IM]} = \Phi[\frac{1}{\beta_{\mathrm{ds}}}\ln(\frac{\mathrm{IM}}{\overline{\mathrm{IM}}_{\mathrm{ds}}})] \tag{4.8}$$

where $\overline{\mathrm{IM}}_{\mathrm{ds}}$ is the median value of spectral displacement at which the building reaches the threshold of damage state, ds; β_{ds} is the standard deviation of the natural logarithm of spectral displacement for damage state, ds; and Φ is the standard normal cumulative distribution function.

4.4.4 Building Inventory

The analyzed inventory contains 1.8 million buildings across the San Francisco Bay Area; see Figure 4.19. In order to estimate seismic losses, the structural system must be known or inferred for all the buildings in the inventory. As shown in Table 4.3, in this inventory the basic attributes of each building, are known. This includes year built, number of stories, occupancy class, and area. The area of each building is calculated based on the Microsoft (2018) building footprint dataset. The occupancy class is noted in HAZUS as shown in Table 4.4. This inventory covers a variety of occupancy types: residential (single-family, multi-family, town house, hotel, mixed use), commercial (retail, office, parking), education (school), and industrial (light and heavy, warehouse). Based on this basic information, the structural type of each building could be inferred following a series of rules.

There is a relationship between the occupancy class and structural type, which usually varies on a regional basis. The distribution of structural types also depends on when the buildings were constructed, and whether they are low-, medium-, or high-rise structures. Age is important because it affects the types of structures that exist in a region. In detail, the inference of structural type follows this mapping schema:

- Buildings older than 1900 are treated as timber or masonry buildings.
- For buildings constructed after 1900, the structural type depends on the number of stories and the occupancy type

The detailed schema can be found in Figure 4.20. Although the inference introduces uncertainties, they should follow some region-specific facts. For example, in California, the occupancy RES1 (single-family dwelling) is 99% W1 (wood, light frame) and 1% RM1 (reinforced masonry bearing wall with wood or metal deck diaphragm, low-rise). Unreinforced masonry (URM) structures were generally not built after 1933. The definition of structural types in Figure 4.20 can be found in Table 5-2 of HAZUS (2019).

Table 4.3: Building Information.

Attribute	Definition
Year Built	Construction year
Stories	Number of stories
Occupancy	HAZUS occupancy class
Structure	HAZUS structure type
Area	Area of building footprint

4.4.5 Results

This section compares the results from the regional simulation of building damage in the San Francisco Bay Area with results of the HayWired Scenario (Detweiler and Wein, 2018). The HayWired Scenario is a study of a hypothetical earthquake scenario in the San Francisco Bay Area. The scenario considers a mainshock of magnitude 7.0 with a rupture along the Hayward fault and an epicenter in Oakland, California. In addition, the effects of aftershocks, liquefaction, landslides, and fires were included in the study. In the HayWired scenario study, a physics-based ground-motion model based on wave propagation and a kinematic rupture model was employed. HAZUS-MH (FEMA, 2012) was used for damage and loss assessment, including the mainshock, 16 aftershocks of magnitude 5.0 or more, liquefaction, and landslides. Herein, only the results from the mainshock were compared with results from a simulation using the SimCenter's rWhale. The comparison is shown in Table 4.5. Both the HayWired scenario and this study used HAZUS-MH for damage assessment. The major differences between the two studies are the ground-motion

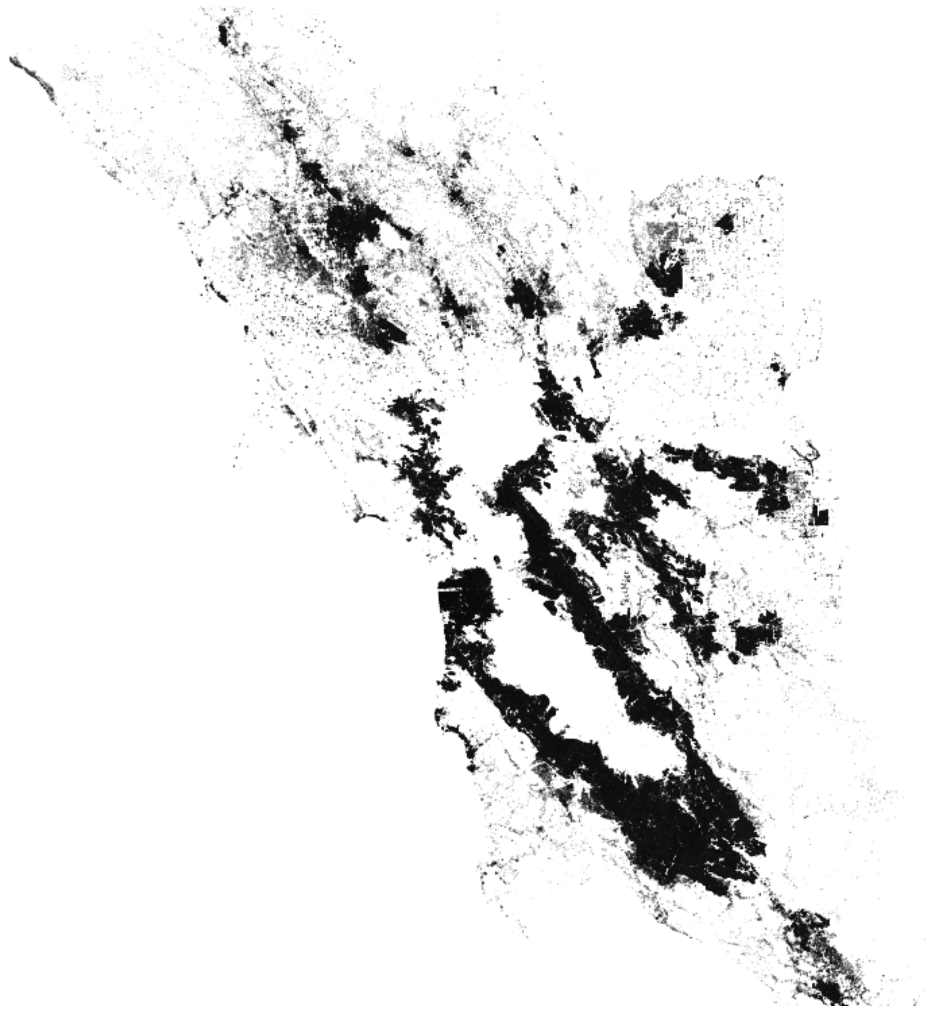

Figure 4.19: Spatial distribution of the building inventory for the study region.

YEAR BUILT	STORIES	OCCUPANCY	MAPPED STRUCTURE TYPES
OLDER THAN 1900	ANY	ANY	Timber (W1) and Masonry (RM1, RM2, URM)
NEWER THAN 1900	1-3	Residential	Timber (W1)
		Commercial	Timber, Steel, Concrete and Reinforced Masonary (W1, S1, S2, C1, C2, C3, RM1, RM2)
		Industrial	Steel, Concrete and Reinforced Masonary (S1, S2, C1, C2, C3, RM1, RM2)
		Other	Timber (W1)
	4-7	Residential & Commercial	Timber, Steel, Concrete (W1, S1, S2, C1, C2)
		Industrial	Steel, Concrete (S1, S2, C1, C2)
		Other	Timber, Steel, Concrete (W1, S1, S2, C1, C2)
	More than 7		Steel and Concrete (S1, S2, C1, C2)

Figure 4.20: Mapping building occupancy to structure types (Elhaddad et al., 2019). The structural type definition can be found in HAZUS (2019).

Table 4.4: Occupancy Type (HAZUS, 2019)

Occupancy Class	Definition
RES1	Residential - Single-Family
RES3	Residential - Town-Home
	Residential - Multi-Family
	Residential - Mixed Use
RES4	Hotel
COM1	Retail
COM4	Office
COM10	Parking
EDU1	School
IND1	Industrial - Heavy
IND2	Industrial - Light
	Industrial - Warehouse

simulation and the building inventory. Discussion on ground-motion simulation difference can be found in Section 4.2.

The building inventory used in the HayWired scenario is the enhanced HAZUS building inventory data originally developed in 2005–2006. It is a dataset mapped from the census-tract level data reflecting the differing ages of the building stock and height patterns, as well as building density. The building inventory used in this study is described in Section 4.4.4. Note: this study differed from the HayWired scenario. Herein, the damage states of 100 ground-motion scenarios were calculated. Each scenario calculated the number of red-tagged buildings; the median was found to be 29,134.

Table 4.5: Comparison of two regional simulations.

	HayWired Scenario	This Study
Fault	Hayward	Hayward-Rodgers Creek
Magnitude	7.0	7.05
Number of Buildings	3 Million	1.83 Million
Red Tagged Buildings	101,000	29,134 (median)

Included here is a visual comparison between the two studies. Figure 4.21(a) shows a map of the damage ratio from the HayWired scenario, while Figure 4.21(b) is a visualization of the red-tagged buildings from this study. Both show that destructive damage will occur in the East Bay following a rupture on the Hayward fault. It should be noted that the HayWired study is performed at the census-tract level, while the simulation herein is performed at the building level, which provides a high-resolution result that enables further analysis of the ground transportation systems and the water distribution system.

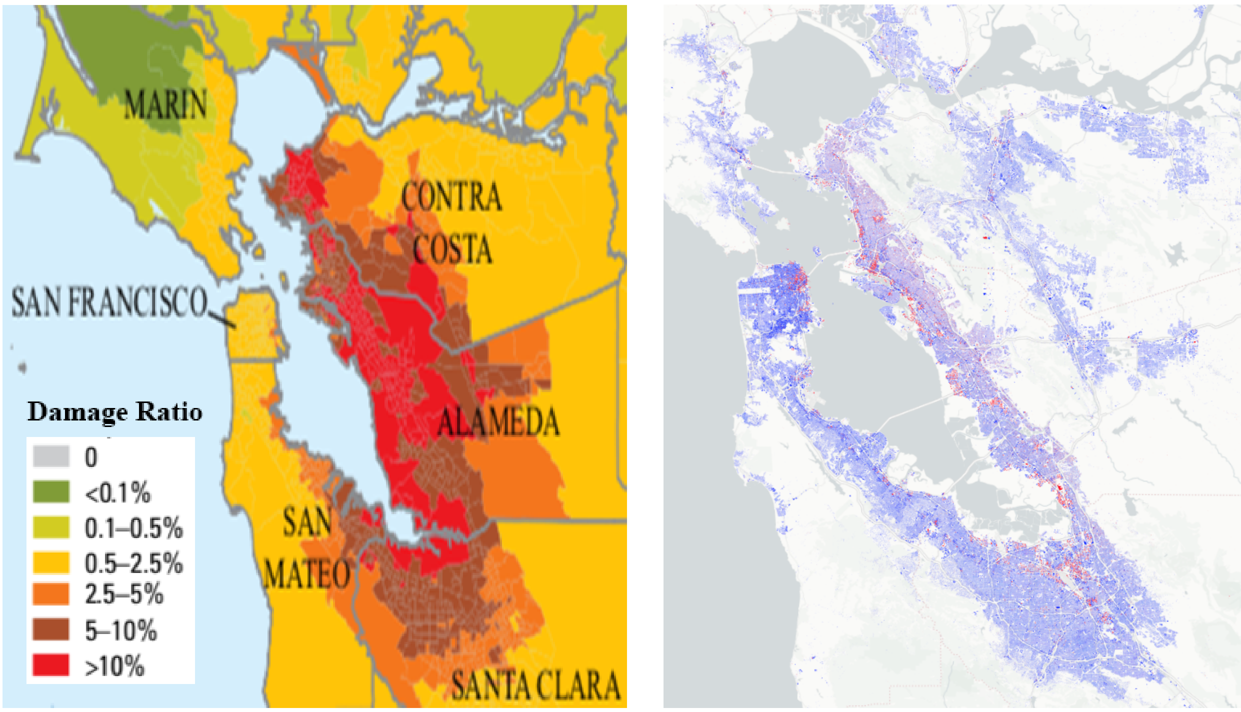

(a) HayWired Scenario: Damage Ratio

(b) This Study: Red Tagged Buildings

Figure 4.21: Comparison of building damage between the HayWired case study and this case study.

4.5 TRAFFIC

4.5.1 Overview

In this case study, the traffic simulation model developed in Section 3 was used to evaluate the impact of earthquake-induced structure and infrastructure damage to the regional traffic system performance. Specifically, two questions will be addressed:

1. What is the loss in the traffic system performance at different stages of the earthquake event (before, immediately after, halfway recovered, and fully recovered)?

2. What is the mutual impact of different infrastructure systems in the event of an earthquake? What would be the difference in the estimated traffic system performance if either one of the WDN or the building structures damage is excluded from the analysis?

Traffic system performance can be evaluated using an array of metrics, such as the total time/distance traveled, the average trip duration, traffic speed, and the total time in congestion. In this case study, the numbers of unfulfilled trips, the total travel time, and the average trip travel time were used as the metrics for comparing the traffic system performance under different scenarios.

Specifically, Question (1) aims at determining the temporal changes in traffic system performance. Due to the complex interaction of the travel demand and supply, the performance loss of the system may not be proportional to the damage of the traffic infrastructure. For example, water deficiencies or building damage in more populous areas will affect the living conditions of more people, which in turn makes a bigger impact on the traffic load in the area. The details of the assumptions made regarding the multiple infrastructure system interactions is given in 4.5.2.

The second question aims to provide an answer regarding the necessity of including multiple infrastructure systems in the analysis. Conventionally, due to the limitations in the choices of models and computational complexities, the interactions of different infrastructure systems were not considered explicitly. This may cause issues, such as inaccurate descriptions of the locations and the levels of the impacts caused by another infrastructure system. To address this question, controlled experiments were carried out where the impacts of the WDN (or building damage) were masked out, and the resulting traffic system performance were compared with the full-scaled simulations where the impacts of multiple infrastructure systems were included.

4.5.2 Modeling framework

A schematic illustration of the framework to combine the impact of building, WDN, and critical traffic link damage into the traffic simulation is shown in Figure 4.22. In general, the infrastructure damage is mapped to changes in the demand and supply side parameters in the traffic simulation.

Suppose that the road network in this simple example serves two communities: Community 1 (the yellow polygon) and Community 2 (the blue polygon). Prior to the earthquake event, there are a total of 100 trips (OD pairs) in the analysis period. Trips starting from Community 1 pick a random road intersection (graph node) as the starting location and end up in another random road intersection inside Community 2 as the destination. The exact start and end locations are required to perform the route computation. Assuming the resolution of the travel demand input is accurate according to the Census Tract levels, it is impossible to know exactly the starting and ending locations of each trip. Given that the average size of the census tract is 5.8 mi^2, the randomness in the start and end location selection is not expected to have widespread impacts on the system performance outcomes.

The damages to the water supply network and the buildings inside each community are reflected as a reduction factor on the travel demand. For example, buildings with a prescribed damage level are deemed to be too dangerous for the occupants to live or work in. Community 1 has 10 such buildings out of 150, thus there are only 140 structurally safe buildings. Given that there are 5 WDN joints that cannot supply sufficient water in the event of an earthquake, this means that an additional 10 buildings would not be habitable due to the lack of water supply if we assume that each water pipeline joint serves 2 buildings or structures. In total, only 130 buildings remain in Community 1 out of 150. Similarly, as shown in Figure 4.22, the number of remaining buildings in Community 2 is 165 out of 200. Assuming that the travel demand is proportional to the remaining safe and serviceable structures in the origin and destination communities, the number of trips considering the infrastructure damage is calculated to be $100 \times (130/150) \times (165/200) \approx 72$.

Pipeline breaks and badly damaged buildings may affect the connectivity of the road network Golla et al. (2020). Preliminary visual inspections suggest that the locations of damaged pipelines and buildings mostly align with the residential roads. The accessibility of these roads would be impacted only during extreme cases (e.g., water bursts, heavy machine presence, or the collapse of high-rise buildings). As a result, their impacts to the road capacity were not modeled. The critical road links in the road network were considered.

In the case study area, the road links that form the Bay Bridge were identified as critical links: the I-80 route is among the most heavily used road link in the network. Because it is a bridge, it is vulnerable to earthquake-induced failures or safety concerns compared to roads laid on the ground, as witnessed by the deck of the Bay Bridge collapsed during the magnitude 7.1 Loma Prieta earthquake in 1989 (Hanks and Krawinkler, 1991). The Bay Bridge has 10 lanes in total (5 in each direction) and the number of lanes was reduced accordingly in post-earthquake scenarios to capture the impact of its damage to regional traffic. In on-going work, the damage of other highway bridges is also being investigated using the fragility curve method, which is expected to be included in the system model in future work.

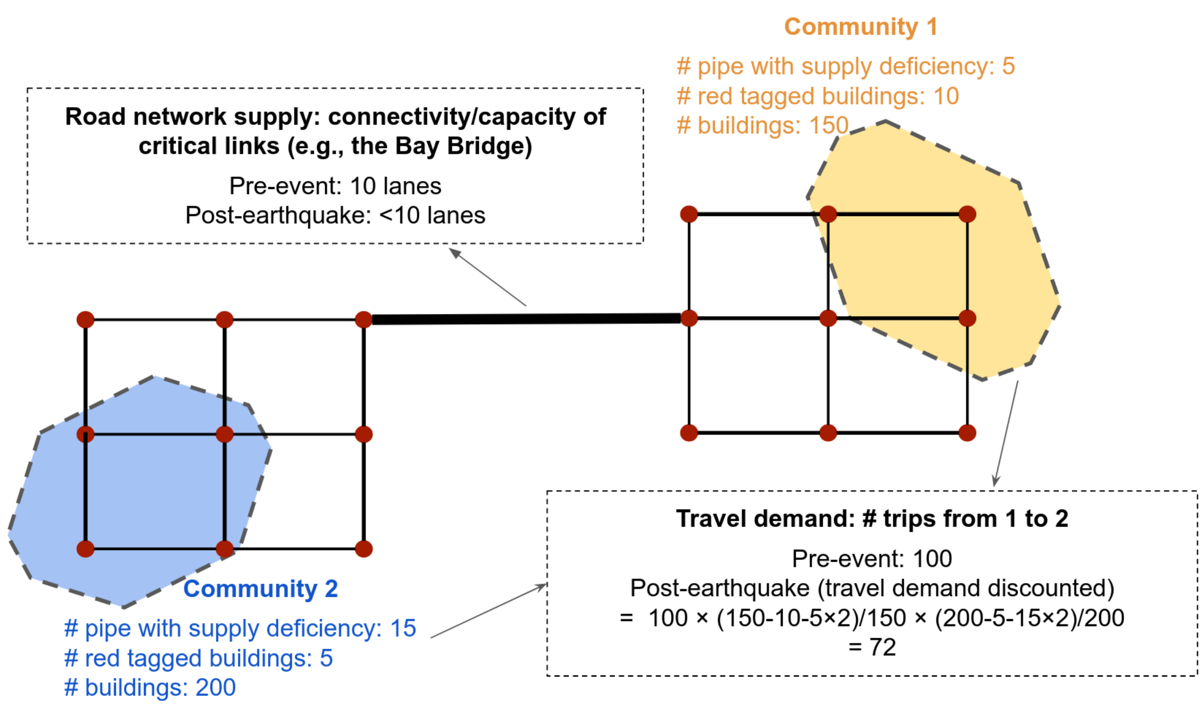

Figure 4.22: Illustration of the earthquake impacts on the traffic supply and demand.

4.5.3 Traffic simulation inputs

Two pieces of traffic inputs have been collected from open data sources, namely, the road network (topology, speed limit, and numbers of lanes) and the travel demand (OD flow). These data sourcing steps are introduced in detail in this section.

Road Network

The road network is retrieved from the OpenStreetMap (OSM) using the OSMnx package (Boeing, 2017). The extent of the network is shown in Figure 4.23. It has 224,223 nodes and 549,008 links. As introduced in Chapter 3, nodes in a network graph represent road intersections; an example of the graph node data utilized here is given in Table 4.6. Each node stores four pieces of information, including its ID in the OSM (*OSMid*) its sequential ID in the graph (*node_id*), and its spatial coordinates (*lon* and *lat*). The spatial coordinates are needed for both visualization purposes as well as for the routing computation in the contraction hierarchy algorithm (Urban Data Science Toolkit (UDST), 2021). Links correspond to the stretch of roads between two intersections and are based on the direction of traffic; therefore, the link that connects node A from node B is different from the link that connects node B from node A.

An example of the graph link data for this case study is given in Table 4.7. Each link stores richer information compared to the nodes, including

- its sequential ID in the graph (*edge_id*)
- the IDs of its beginning and end nodes (*start_nid* and *end_nid*)
- the number of lanes (*lanes*)
- the geometry of the road (*geometry*)
- the speed limit (*speed_limit*)
- the length (*length*) of the road that is derived from the *type* and the *geometry* field

In addition, the free-flow travel time (*fft*) is calculated based on the *length* and the *speed_limit*, while the capacity of the road (*capacity*) is obtained from *lanes* and *speed_limit*, following the assumptions in Çolak et al. (2016). Since the OSMnx package performs preliminary data cleaning by merging and splitting the raw roadway element from OSM, each link may have one or multiple corresponding OSM IDs. As a result, this field was not kept. The locations of the road link in OSM can be retrieved based on the geometry of the road itself or the coordinates of its start and end nodes.

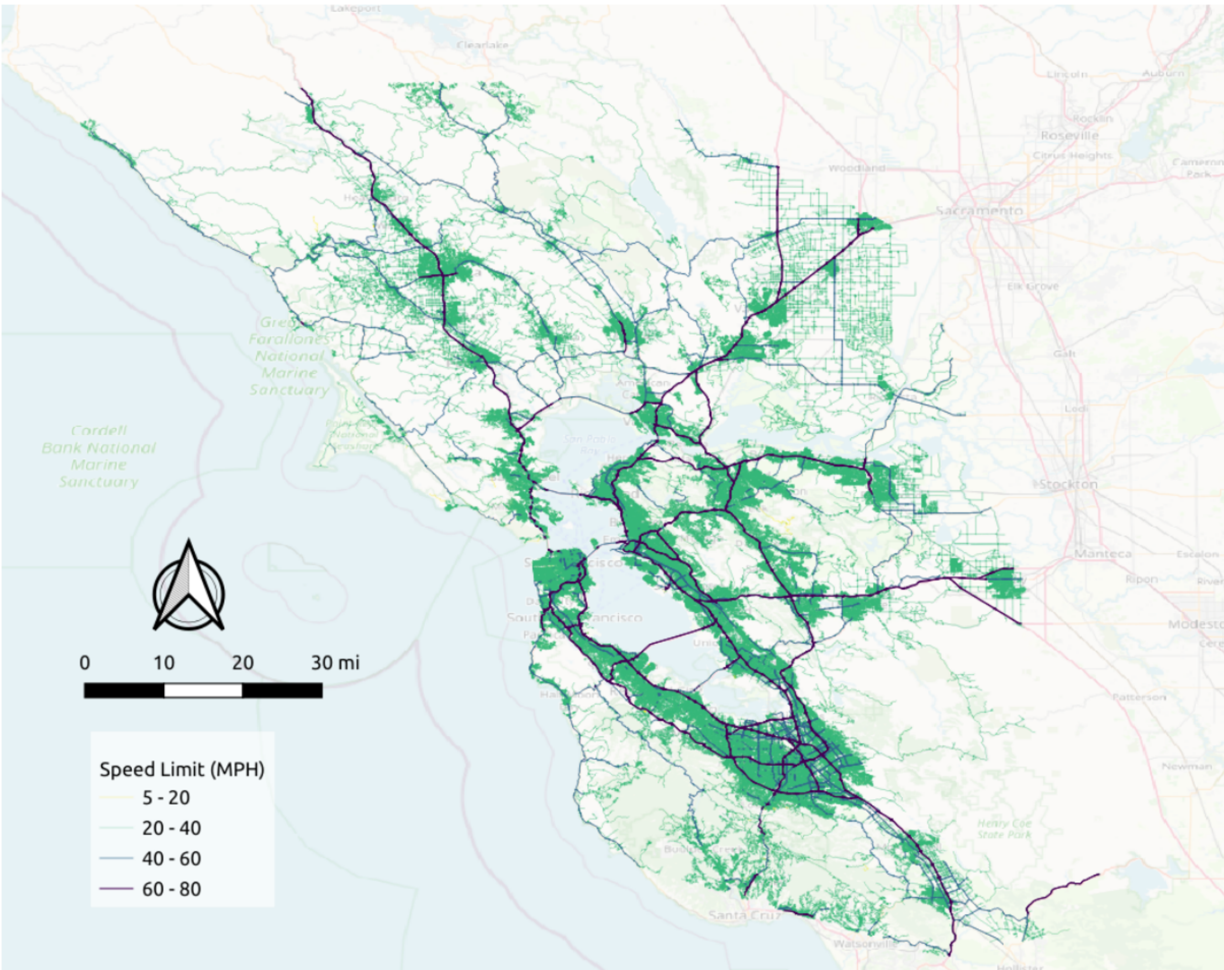

Figure 4.23: Road network retrieved from OSMnx.

Table 4.6: Examples of road network nodes.

node_id	*OSMid*	*lon*	*lat*
0	56098817	-122.7694487	38.4353358
1	65536002	-122.1367804	37.4071341
2	56098819	-122.7692682	38.4337626
3	1919942662	-121.9720395	38.0147677
4	65536007	-121.7783559	37.3251994
...	...	...	...

Table 4.7: Examples of road network links.

edge_id	*start_nid*	*end_nid*	*type*	*lanes*	*geometry*	*speed_limit*	*length*	*fft*	*capacity*
0	0	2	residential	1	”LINESTRING (-122.7694487 38.4353358, -122.7692682 ...”	25	175.64	15.72	950
13	4	218360	secondary	1	”LINESTRING (-121.7783559 37.3251994, -121.7786638 ...”	25	337.46	30.19	950
26	8	144017	tertiary	1	”LINESTRING (-121.9582606 38.0145139, -121.9581005 ...”	25	68.21	6.10	950
88	34	224204	motorway	2	”LINESTRING (-121.5600854 36.8849092, -121.5596734 ...”	65	1698.09	58.44	4700
131	55	28202	primary	2	”LINESTRING (-122.4126087 37.7483314, -122.4132281 ...”	25	96.05	10.31	1900

Three recovery-stage scenarios were considered in the simulation: namely, the pre-event scenario, the immediately post-earthquake scenario, and the halfway recovered scenario. Permanent relocation of residents was not considered, i.e., the fully recovered scenario would be the same as the pre-event scenario. The critical links in the road network were identified as those forming the Bay Bridge. The capacities of these critical links were modified according to each recovery stage scenario; see Figure 4.8. Specifically, the road networks for the pre-event scenario and the fully recovered scenario were the same, namely, the original road network retrieved from OSMnx (with some derived fields, such as *fft* and *capacity*). Immediately post-earthquake, it was assumed that travel on the Bay Bridge will be temporarily halted due to concerns of the bridge safety and functionality. After it has been inspected and necessary restoration performed, the capacity of the Bay Bridge will be considered in the halfway recovered scenario.

Table 4.8: Critical link connectivity/capacity before and after the hypothesized earthquake.

Scenario	Critical link capacity
Pre-event	Bay Bridge capacity is assumed to be 15,000 vehicles per hour.
Immediately after earthquake	Bay Bridge is assumed to be impassable.
Halfway recovered	Bay Bridge capacity is assumed to be 7,500 vehicles per hour.
Fully recovered	Bay Bridge capacity is assumed to be 15,000 vehicles per hour.

Travel demand

The travel demand was obtained from the Census Transportation Planning Package (CTPP), based on a five -year American Community Survey (ACS) Data (American Association of State Highway and Transportation Officials (AASHTO)), years 2012–2016. The online database (shown in Figure 4.24) contains a variety of traffic-related data tables, such as the total number of workers, vehicle ownership, means of transport, and household income levels. The data were aggregated to different spatial units, with the smallest unit being the census tract. The data table of interest for this study is "B302201: Time leaving home by means of transportation." This table was filtered to keep only the records for census tracts in the San Francisco Bay Area and where the modes of transportation were designated as "Drove alone" or "Carpooled". It is assumed that carpooled vehicles were shared by two workers, and thus the total numbers of workers between each origin and destination census tract pair can be determined from Equation (4.9):

$$\begin{aligned}
&\text{Total numbers of vehicular trips between an origin-destination census tract pair}\\
&= \text{Drive alone, departure time from 5:00 a.m. to 8:59 a.m. (CTPP Line Number 16)}\\
&+0.5 \times \text{Carpool, departure time from 5:00 a.m. to 8:59 a.m. (CTPP Line Number 17)}\\
&+ \text{Drive alone, departure time from 9:00 a.m. to 4:59 a.m. (CTPP Line Number 23)}\\
&+0.5 \times \text{Carpool, departure time from 9:00 a.m. to 4:59 a.m. (CTPP Line Number 24)}
\end{aligned} \tag{4.9}$$

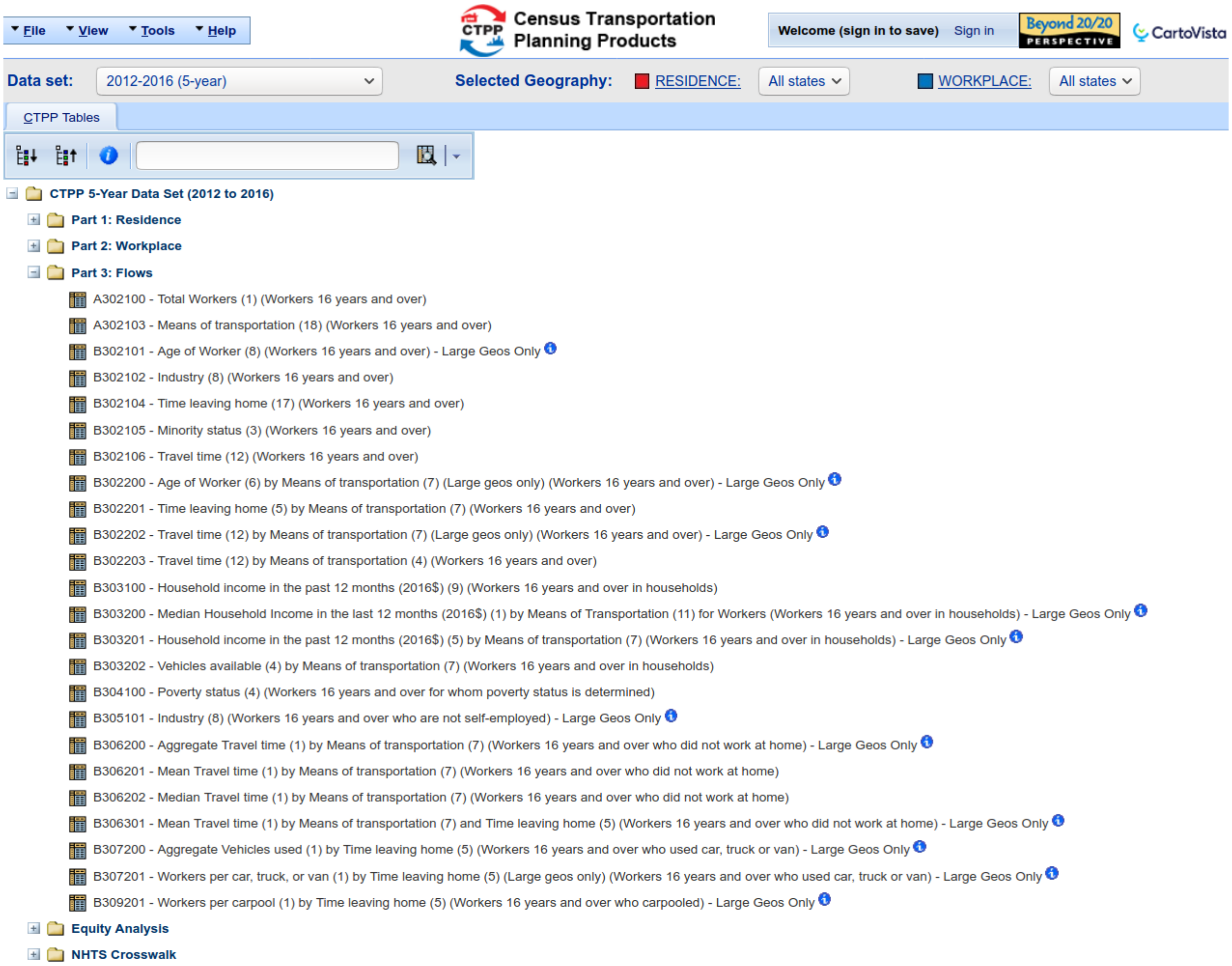

Figure 4.24: Web portal to access the CTPP data.

This produces a total number of 2,049,285 commute trips from/to 1577 census tracts. This number is used as the pre-event travel demand. Since the CTPP data contains only crude departure times (5-9 AM, or 9-5 AM), a new departure hour is randomly generated for each trip, where there are 10%, 40%, 40%, and 10% of a chance that the trip starts at 6 AM, 7 AM, 8 AM, and 9 AM. All trips were assumed to start during this morning peak period given that the CTPP traffic flow data are mostly for work-related trips. This census tract-level travel demand is plotted in Figure 4.25, where the darker lines indicate higher levels of travel demands from the start location to the end location.

As explained in Section 4.5.2, pipe-break-induced water shortages and building structure damage may both make communities unsafe or inconvenient for residents to remain, thus forcing relocation and reducing the travel demand compared to a normal scenario. In this case study, it was assumed that immediately after the earthquake, buildings with a damage severity category corresponding to 3 and above will need further building inspection and require the residents to be evacuated.

On the water pipeline side, for the immediate post-earthquake scenario, it is assumed that

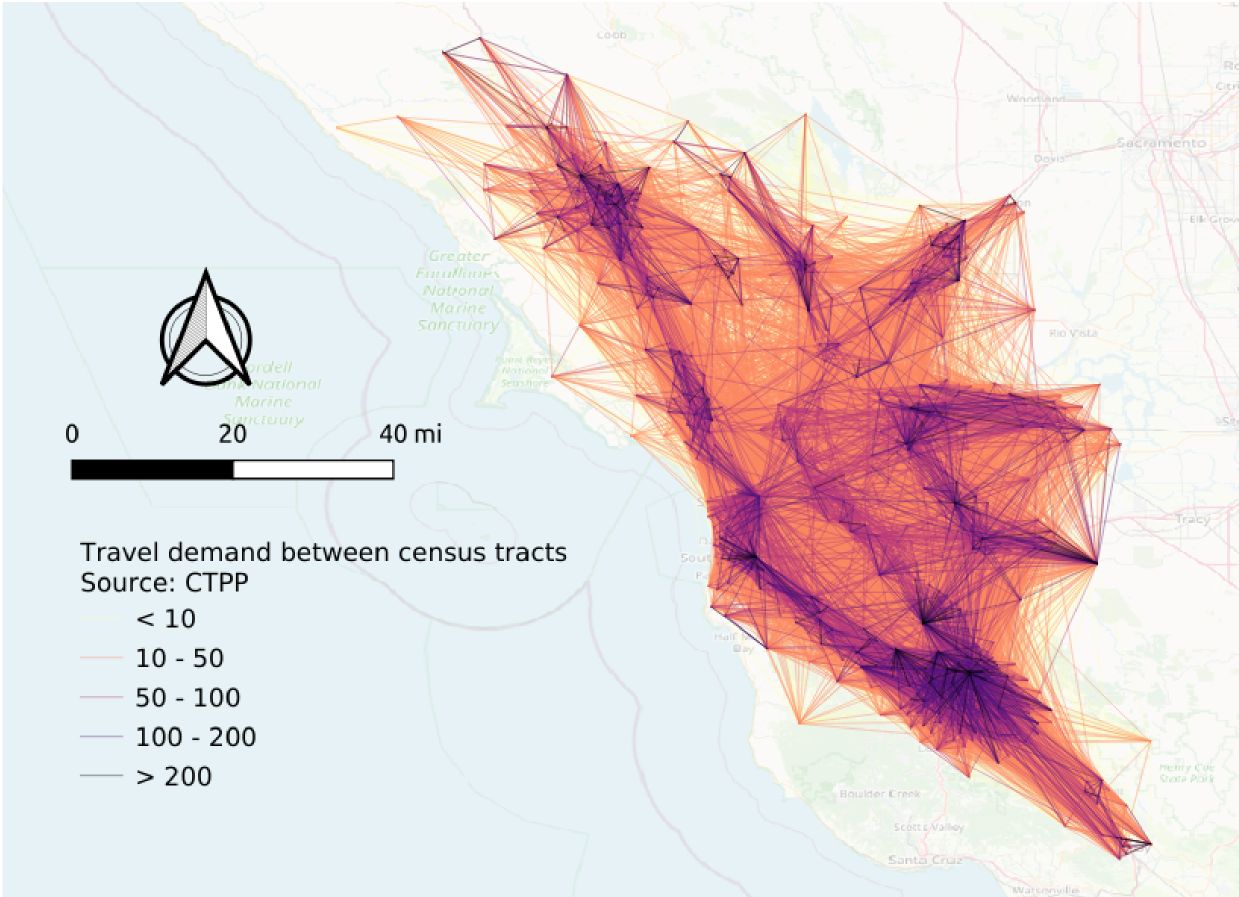

Figure 4.25: Travel demand between census tracts for the San Francisco Bay Area based on the CTPP data.

pipeline serviceability will be greatly impacted, and thus any pipe node with a water shortage ratio larger than 1% is assumed to be closed due to pipeline inspection and maintenance. Such an assumption is based on the fact that water utility companies tend to isolate damaged subsystems from the main system after a major earthquake to prevent continuous water loss (Porter, 2018). Therefore, supply nodes with insignificant water supply loss from the hydraulic simulation may fail to supply water to end users post-event due to the sub-system isolation protocols. Locations of such water deficient nodes for two earthquake scenarios (mean PGV of 13.06 cm/sec and 16.87 cm/sec) are shown in Figures 4.16 and 4.17.

For the halfway recovered scenario, it is assumed that fewer buildings (i.e., only those building designated with damage severity category 4) and half of the originally closed pipes (i.e., a random half of the WDN nodes with water shortage ratio of 1% and above) will still be affected by the earthquake damage, and the travel demand would recover accordingly. The travel demand scenarios are summarized in Table 4.9. Although these relatively strong assumptions were made with limited knowledge on relocation and recovery, they can be utilized for the purpose of this case study. Further research is being done regarding the migration patterns that will occur after seismic events in the San Francisco Bay Area.

Table 4.9: **Travel demand reduction before and after the hypothesized earthquake.**

Scenario	Infrastructure damage	Travel demand discount
Pre-event	No damage	No discount
Immediately after earthquake	No water if the water shortage ratio $\leq 1\%$, building unsafe if damage severity $\geq$ Category 3	OD flow discounted to the proportion of working pipeline nodes and safe buildings in the origin and destination census tracks
Halfway recovered	No water for half of the nodes with water shortage ratio $\leq 1\%$, building unsafe if damage severity $\geq$ Category 4	

Due to the computational challenges, only 20 earthquake scenarios were performed in the traffic simulation. The average number of OD trips in each scenario are given in Table 4.10. If both building structure damage and earthquake-induced water supply shortages are considered, the number of trips immediately after the earthquake is estimated to be 1,679,211, or 82.94% of the pre-event scenario. If the building damage is not considered (i.e., assuming no building damage), the number of OD trips immediately post-earthquake is very close to the pre-event travel demand (97.76% of the pre-event OD counts). If the water pipeline damage is not considered, the number of OD trips is only 84.29% of the pre-event level. This indicates that the level of impact of damage to the water pipeline supply is not as influential as damage to buildings. In scenarios where the damage to the infrastructure are halfway recovered, the number of OD trips is estimated to be 1,854,721, or 90.64% of the pre-event level. Again, building damage has a greater impact than pipeline damage in terms of the travel demand reduction, with the levels of travel demand being 91.43% and 98.61%, respectively, if only considering single building or pipeline infrastructure system damage.

4.5.4 Traffic Simulation Results

The road network and travel demand derived in sections above are input into the traffic simulation framework developed in Section 3. A variety of traffic-related metrics are obtained, including the temporal changes of the numbers of fulfilled trips, total vehicle hours traveled (VHT), average trip duration and impacts to traffic statistics at census tract pair levels. These results are detailed in Section 4.5.4. A similar set of statistics were also derived without considering the interdependencies of multiple infrastructure systems, and the results are given in Section 4.5.4.

Table 4.10: **Average OD counts in different simulation scenarios.**

Scenario	OD counts	% of pre-event scenario
Pre-event	2,046,272	-
Immediately after earthquake	1,679,211	82.94%
Immediately after earthquake (without considering building damages)	2,000,372	97.76%
Immediately after earthquake (without considering pipeline damages)	1,724,846	84.29%
Halfway recovered after earthquake	1,854,721	90.64%
Halfway recovered after earthquake (without considering building damages)	2,017,902	98.61%
Halfway recovered after earthquake (without considering pipeline damages)	1,870,910	91.43%

Temporary trends of the traffic performance recovery

Before an earthquake event, the traffic system in active use in the area of interest was studied. Consider a travel demand of about 2 million trips for the morning peak period [Figure 4.26(a)] where the total VHT is about 596,568 hours; see Figure 4.26(b) and Table 4.11). The average trip duration in the pre-event scenario is around 17 minutes; see Figure 4.26(c) and Table 4.11). Immediately after the earthquake, both the travel demand and the capacity of the Bay Bridge decrease, leaving 349,061 unfulfilled trips compared to the pre-event scenario. The total VHT reduces, on average, from 596,568 hours to 511,618 hours across the 20 simulated earthquake scenarios. The average trip travel time increased by a small amount, from 17.49 minutes to 18.04 minutes. This change in traffic performance metrics can be better understood from visual representations presented in Figures 4.26 and 4.27. In Figure 4.26, the traffic simulation results for each random earthquake scenario is presented, where Figure 4.26(a) shows the total OD counts, Figure 4.26(b) shows the total VHT, and Figure 4.26(c) is the average trip time.

It can be seen that the total numbers of OD pairs and the VHT both decrease immediately after the earthquake, but not the average travel time. Across different earthquake scenarios, the average travel time immediately post-earthquake may be higher or lower compared to the pre-event level but with small variations. Despite the closeness in the average trip time results before and after earthquake events, the spatially disaggregated trip information can reveal more insights. Figure 4.27(a) and (b) show the trip travel time and percentages of unfulfilled trips aggregated to each census tract pairs. The color of each line represents the average traffic metric aggregated for all trips across all earthquake scenarios. Figure 4.27(a) shows the tract-level increase in the average trip travel time. Note: there is a significant increase in travel times for trips across the

Bay Bridge. Based on the simulation results, although there are more numbers of tract-level OD pairs with decreased travel time, the range of reduction is usually small (i.e., within 5 minutes). A study of the tract-level OD pairs with larger differences in post-earthquake travel time only (5–15 minutes or over 15 minutes), is dominated in those census tract pairs with larger increases in travel time. For example, there are 1664 census tract pairs with an increase in travel time from 5–15 minutes, and 4329 with an increase greater than 15 minutes. In comparison, only 430 and 9 census tract pairs have a reduction in travel times within the 5–15 minutes window and beyond 15 minutes. Altogether, this demonstrates the relation of the system average trip travel time before and immediately after the earthquake, as shown in Figure 4.26 above.

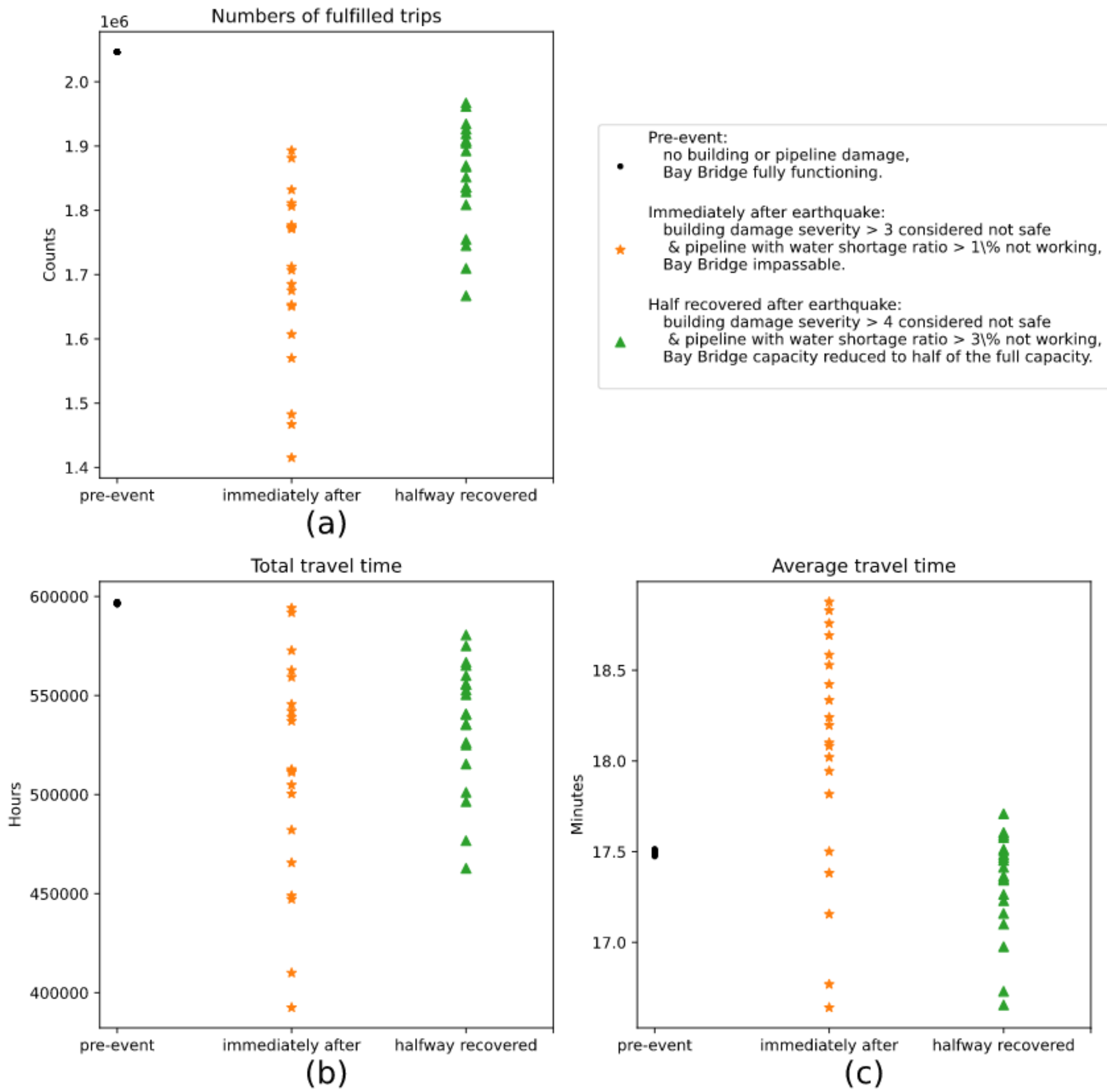

Figure 4.26: Changes in traffic-related metrics at different stages of earthquake recovery: (a) total numbers of fulfilled trips; (b) total travel time; and (c) average trip travel time.

Table 4.11: Traffic-related metrics in different stages of earthquake damage.

Metrics	Pre-event	Immediately after earthquake	Halfway recovered
Unfulfilled trips	-	349,060	191,551
Total travel time (hours)	596,568	511,618	535,892
Average trip travel time (minutes)	17.49	18.04	17.32
Track pairs with increase in travel time > 15 minutes	-	4,329	58
Track pairs with increase in travel time in 5-15 minutes	-	1,664	2,870
Track pairs with unfulfilled trips > 50%	-	3,574	1,004
Track pairs with unfulfilled trips in 30-50%	-	19,881	6,879
Track pairs with unfulfilled trips in 20-30%	-	18,830	16,418

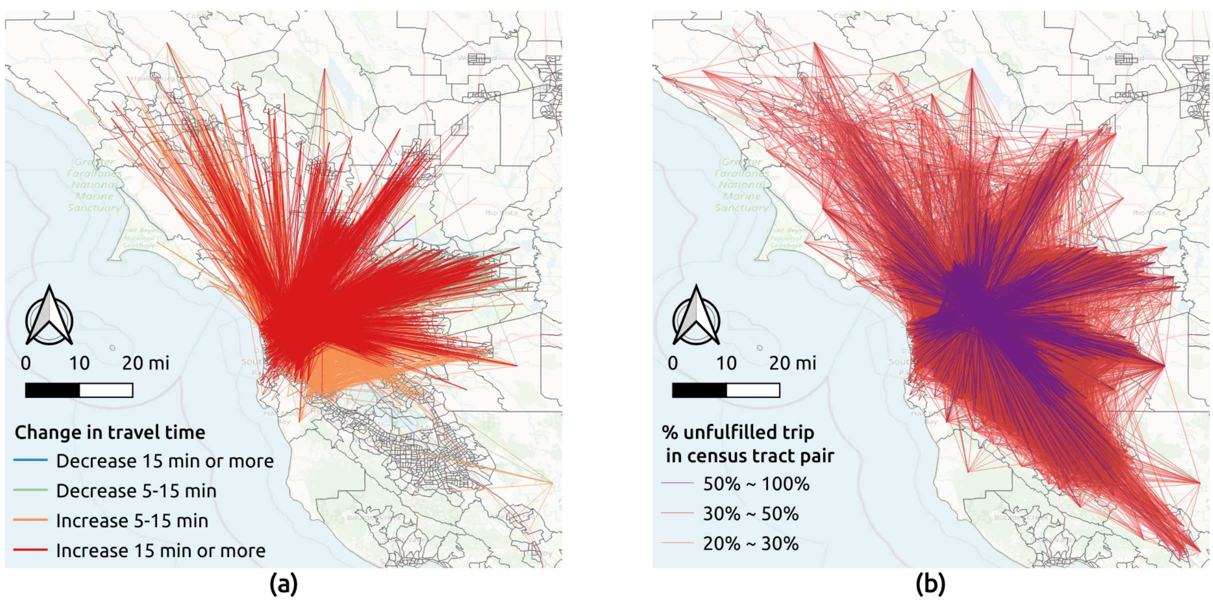

Figure 4.27: Changes in tract-level traffic statistics in the "immediately post-earthquake" scenario: (a) increase in average travel time; and (b) percentage of unfulfilled trips.

The last column in Table 4.11 presents the changes in the traffic-related metrics for the halfway recovered scenario, where building damage category below 4 (complete damage according to the HAZAS status classification, or destroyed/red-tagged in other classification systems) are assumed to be safe, and half of the pipelines with water deficiency ratio above 1% are assumed to be now functional. The Bay Bridge capacity returns to half of its normal level. It can be seen that the numbers of unfulfilled trips reduce from 349,060 to 191,551 compared with the immediately post-earthquake scenario. The total VHT also bounces back to 535,892 hours, which is still 10% lower than the pre-event level. In terms of the average trip travel time, it is still relatively close to the pre-event scenario at around 17 minutes. Based on Figure 4.26, it can be seen that the average trip duration in each earthquake scenario is mostly below the pre-event level [green triangles compared with black dots in Figure 4.26(c)], which is the same as the numbers of OD pairs and the total VHT; see Figure 4.26(a) and (b).

As shown in Figure 4.28(a), the travel time increase has reduced significantly compared to the immediate post-earthquake scenario for spatially disaggregated census-tract level results. This is mainly due to the recovery of the Bay Bridge capacity from zero to half of its normal value. The reduction in unfulfilled trips is also evident in the halfway recovered scenario [4.28(b)], which can be attributed to the assumption that the population has also recovered along with the restoration of building occupancy and the water supply.

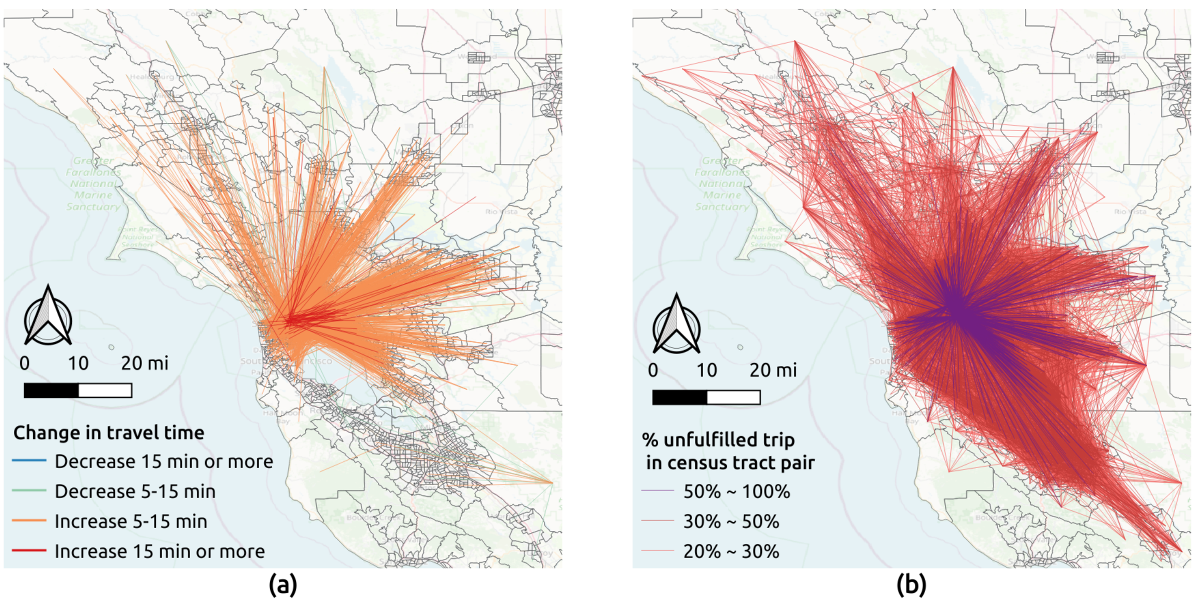

Figure 4.28: Changes in tract-level traffic statistics in the "halfway recovered" scenario: (a) Increase in average travel time; and (b) percentage of unfulfilled trips.

Impacts of System Dependencies

A common issue in regional resilience assessment is the lack of consideration of the mutual influences between multiple infrastructure systems. For example, in this case study, the traffic system performance metrics would be different if damage to buildings or pipelines is not considered. The differences are illustrated in Figure 4.29, and the quantitative differences are given in Table 4.12. In Figure 4.29, the numbers of OD pairs, total VHT, and average travel time without considering the pipeline and building damage are plotted next to the counterpart where both system damages are incorporated. In both the immediately after earthquake and the halfway recovered scenarios, the traffic performance metrics do not change much between the two cases with and without considering pipeline damage (red stars and purple triangles). That said, if the building damage is not considered, the loss in travel demand will be greatly underestimated [see brown and pink markers in Figure 4.29(a)]. Compounded by the reduction in the capacity of the Bay Bridge, the remaining traffic will need to be rerouted, thus creating larger overall VHT as well as increasing individual trip time compared to the cases where building damage is included.

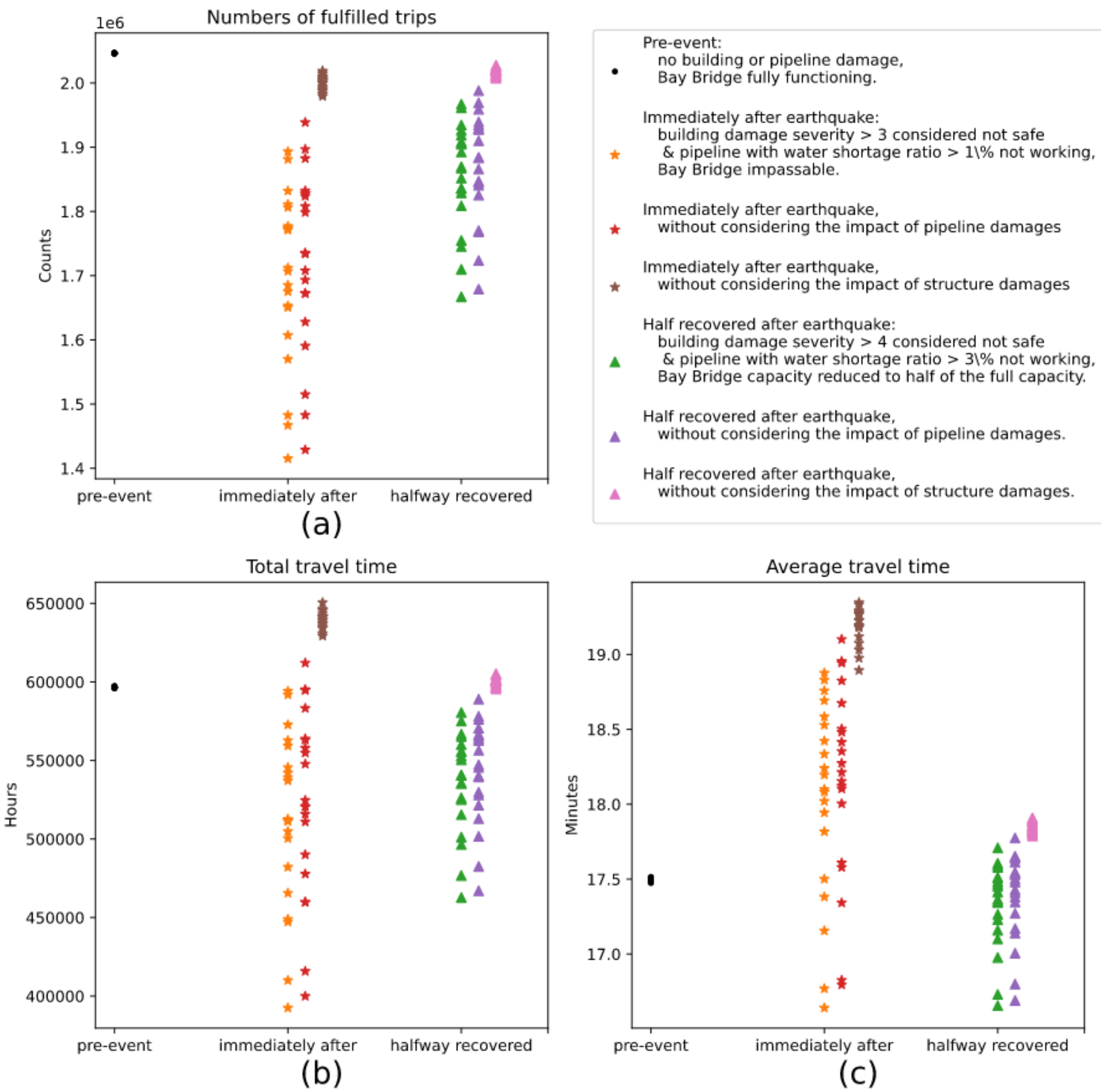

Figure 4.29: Impacts of damage in the WDN and structures on traffic-related metrics at different stages of earthquake recovery: (a) total numbers of fulfilled trips; (b) total travel time; and (c) average trip travel time.

In the quantitative comparison results given in Table 4.12, the variations in the traffic performance metrics with and without considering the performance of the interdependent systems are presented. In the immediately post-earthquake scenario, if both the building and pipeline damage are considered, the total VHT is 511,618 hours, which is close to the total VHT immediately after the earthquake event if only building damage is considered (523,418 hours). If only the pipeline damage is considered, the total VHT increases to 639,793 hours, which is 25% higher than the estimates when considering both building and pipeline damage. The same applies to the average trip duration, where the omission of building damage resulted in an average increase of 1 minute. A similar trend is seen in cases associated with the halfway recovered scenario, where similar results are seen in cases with both building and pipeline damage versus building damage only. If building damage is not considered, then it results in higher VHT and average trip duration.

Table 4.12: Traffic-related metrics in different stages of earthquake damage with and without considering system dependencies.

Metrics	Pre-event	Immediately after earthquake			Halfway recovered		
		Base	No pipe damage	No building damage	Base	No pipe damage	No building damage
Unfulfilled trips	-	349,061	321,426	45,900	191,551	175,362	28,370
Total travel time (hours)	596,568	511,618	523,418	639,793	535,892	542,226	600,362
Average trip travel time (minutes)	17.49	18.04	18.16	19.19	17.32	17.38	17.85

4.5.5 Discussion

This case study presented the impact of earthquake-induced infrastructure damage on regional traffic performance. It clearly shows the spatial and temporal impacts, as well as the importance of considering all related infrastructure systems to obtain a holistic understanding of the level of disruption.

There are a few limitations that deserve mention in the interpretation of the results. First, only the traffic, building, and part of the WDN systems in the San Francisco Bay Area were considered because of the limited data availability. Other infrastructure systems and sub-systems are also likely to suffer damage and impact the regional traffic patterns, such as the collapse of roadway bridges, disruption of the electrical supply system, and any breakdowns in the communication infrastructure. These issues were currently not considered in the case study due to the difficulty in acquiring related data.

In addition, the assumption that people will relocate away from the damaged area and move back depending on the extent of building damage and water supply shortages needs further study. Empirical evidence suggests that people's relocation decisions are complex, and the population do not simply return to the original state after a major disaster. The theories behind disaster-related migrations are rather sparse, which need to be better explored in future studies.

Finally, the recovery and rebuilt process are not modeled in detail. The "halfway recovered scenario assumes the damage is half of those that occur "immediately after earthquake" scenario. In reality, the allocation and optimization of limited resources and personnel can be a critical issue in the recovery phase. Ongoing research is being carried out to quantify the most efficient schedule for the repair of broken pipes.

5 Conclusion

This PEER project aimed to develop simulation toolkits for city-scale infrastructure system resilience quantification. Specifically, models for city-scale traffic simulation and water distribution networks hydraulic analysis were designed and tested under earthquake scenarios.

The complex behaviors of the entire city-scale transportation system were modeled through a multi-threaded, high-performance computing scalable semi-dynamic traffic simulation model. Various traffic performance metrics (e.g., traffic flow, delay, and accessibility) were estimated using the developed model during a large-scale hazard event such as an earthquake. The model was constructed using a semi-dynamic framework, which divided an analysis period (typically 24 hours or during the morning peak hours) into 15-minute slices. In each time slice, the vehicles were gradually assigned to their shortest paths in batches. After each batch, the road link-level travel times were updated to reflect the traffic congestion. For trips that could not finish their trips in 15 minutes, the remaining part of the trips was added to the next 15-minute time step as “residual demand.” This framework captured the dynamics of traffic loads during peak hours while still preserving the computational efficiency and flexibility for an extensive network.

An efficient, multi-threaded C++ WDN hydraulic simulator (HydrauSim) was developed to quantify the hydraulic behavior of water distribution networks (WDNs) after a disruptive hazard event such as an earthquake. HydrauSim includes functions to include disruptive incidents (pipe leaks/breaks) in the WDN hydraulic analysis. A modified pressure-driven model (PDD) simulation was used to quantify the pipe-failure-induced water leakages. Moreover, HydrauSim includes tools to understand the relationship between isolation valve conditions and WDN system risks: specifics include the ability of reading, configuring, and analyzing the impact of isolation valves on the network. Most importantly, HydrauSim is capable of performing efficient simulations on extremely large-sized WDNs. It is considerably faster than existing WDN hydraulic simulators on networks with over 10,000 nodes and edges.

Impacts of infrastructure systems from earthquake scenarios (M7.05 Hayward Fault) in the San Francisco Bay Area were studied. The ground-motion scenarios were generated using a PSHA approach. Specifically, A set of 100 rupture events from UCERF2 (Working Group on California Earthquake Probabilities(WGCEP), 2008) for a M7.05, Hayward-Rodgers Creek HN+HS earthquake were simulated with spatial correlation considerations on earthquake IMs.

The impact of an earthquake on the water distribution network and building systems were estimated using generated IMs. The probability of failure for each WDN pipe was calculated using pipeline fragility curves with the simulated earthquake ground motion IMs (PGV). The damaging degree of the WDN was simulated using the estimated failure probability for each earthquake scenario. An earthquake-induced regional water shortage was simulated using the developed hydraulic simulator, HydrauSim. A Monte Carlo simulation was used since multiple ground-motion scenarios were considered herein. The simulation was performed on East Bay Municipal Utility District (EBMUD) main gravity feed zone. Around 200–800 pipes were estimated to break during the simulated earthquake events. On average, 25% of demand nodes may experience insufficient water pressure level, which can rise to 78% for the worst case scenario.

The damage states of 1.8 million buildings after the hypothesized earthquake scenario across the San Francisco Bay Area were simulated using the SimCenter rWhale software (Elhaddad et al., 2019). rWhale evaluates the seismic performance of buildings using the FEMA P-58 method. It performs a nonlinear structural dynamic analysis to obtain the engineering demand parameters (EDPs), such as lateral drifts, accelerations, etc., caused by seismic ground motions. Around 30,000 buildings were considered as red-tagged for the simulated earthquake scenarios.

Traffic simulations were performed under simulated earthquake scenarios. Road connectivity was assumed to be damaged from water main break events through flooding or the presence of heavy repair work that may block roads. Since people cannot live or work in red-tagged buildings, the travel demand is assumed to decrease for those areas that sustained heavy structural damage. Also, the capacity of the Bay Bridge is assumed to be affected by the earthquake. The simulated changes in the traffic volume in the Bay Area during the morning peak hours immediately following the hypothesized earthquake scenarios were concentrated in the East Bay area near the rupture locations; however, neighboring areas were also affected due to commuting patterns.

Regarding infrastructure system interdependence, in both the immediately post-earthquake and halfway recovered scenarios, the traffic performance metrics do not change much when pipeline damage is not considered. However, if the building damage is not considered, the loss in travel demand will be significantly underestimated. Compounded by the reduction in the capacity of the Bay Bridge, the remaining traffic will need to be rerouted, thus creating an increase in the overall vehicle hours traveled (VHT) as well as individual trip time.

REFERENCES

Aagaard B.T., Boatwright J., Jones J., MacDonald T., Porter K.A. (2017). HayWired scenario mainshock, ground motions, S. Detwiler and A. Wein (Eds). *Scientific Investigations Report 2017-5013*, Chapters A-H, U.S. Geological Survey, Reston, VA.

Aagaard B.T. Graves R.W., Schwartz D.P., Ponce D.A., Graymer R.W. (2010a). Ground-motion modeling of Hayward fault scenario earthquakes, Part I: Construction of the suite of scenarios, *Bull Seismol. Am*., 100(6):2927–2944, https://doi.org/10.1785/0120090324.

Aagaard B.T. Graves R.W., Rodgers A., Brocher T.M., Simpson R.W., Dreger D, Petersson N.A., Larsen S., Ma S., Jachens R.C. (2010b). Ground-motion modeling of Hayward fault scenario earthquakes, Part II: Simulaton of long-period and broadband ground motions, *Bull Seismol. Am*., 100(6):2945–2977, https://doi.org/10.1785/0120090379.

Ait-Ali A., Eliasson J. (2019). Dynamic origin-destination-matrix estimation using smart card data: An entropy maximization approach, *RailNorrkoping*, Norrköping, Sweden.

American Lifelines Alliance (2001). *Seismic Fragility Formulations for Water Systems, Part I: Guildine*s, Federal Emergency Management Agency, Washington D.C.

Asefa T.; Clayton J.A. Adams A., Anderson D. (2014). Performance evaluation of a water resources system under varying climatic conditions: Reliability, resilience, vulnerability and beyond, *J. Hydrol*., 508:53–65, https://doi.org/10.1016/j.jhydrol.2013.10.043.

AASHTO (n.a.). American Association of State Highway and Transportation Officials https://ctpp.transportation.org/2012-2016-5-year-ctpp.

Baker J.W. (2008). *An Introduction to Probabilistic Seismic Hazard Analysis* (*PSHA*), White Paper, Version 1, 72 pgs.

Bliemer M.C., Raadsen M.P., Brederode L.J., Bell M.G., Wismans L J., Smith M.J. (2017). Genetics of traffic assignment models for strategic transport planning, *Trans. Rev.*, 37(1):56–78, https://doi.org/10.1080/01441647.2016.1207211.

Boore D.M., Atkinson G.M. (2008). Ground-motion prediction equations for the average horizontal component of PGA, PGV, and 5%-damped PSA at spectral periods between 0.01 s and 10.0 s., *Earthq. Spectra*, 24(1):99–138, https://doi.org/10.1193/1.2830434.

Casey G., Zhao B., Kumar K., Soga K. (2020). *Context-Specific Volume–Delay Curves by Combining Crowd-Sourced Traffic Data with Automated Traffic Counters: A Case Study for London,* Data-Centric Engineering, Vol. 1, Cambridge University Press, https://doi.org/10.1017/dce.2020/18.

Christodoulou S.E., Fragiadakis M. (2015). Vulnerability assessment of water distribution networks considering performance data, *J. Infrastruc, Sys.*, 21(2), https://doi.org/10.1061/(ASCE)IS.1943-555X.0000224.

Çolak, S., Lima, A., and Gonzalez, M. C. (2016). Understanding congested travel in urban areas, *Nat. Commun*., 7(1):1–8.

Crowl D.A., Louvar J. F. (2001). *Chemical Process Safety: Fundamentals with Applications*, Pearson Educatoin, Englewood Cliffs, New Jersey.

De Coninck A., De Baets B., Kourounis D., Verbosio F., Schenk O., Maenhout S., Fostier J. (2016). Needles: Toward large-scale genomic prediction with marker-by-environment interaction, *Genetics*, 203(1):543–555, https://doi.org/10.1534/genetics.115.179887.

Detweiler S., Wein A. (2017). The HayWired earthquake scenario–engineering implications, *Scientific Investigations Report 2017-5013*, Chapters I–Q, U.S. Geological Survey, Reston, VA, https://doi.org/10.3133/sir20175013.

Deierlein G.G., McKenna F., Zsarnóczay A. Kijewski-Correa T.L., Kareem A., Elhaddad W., Lowes L., Schoetller M.J., Govindjee S. (2020). A cloud-based application framework for simulating regional-scale impacts of natural hazards on the built environment, *Front. Built Environ*., 6(19), https://doi.org/10.3389/fbuil.2020.558706.

Deierlein G.G., Zsarnóczay A. (2021). *State of Art in Computational Simulaton for Natural Hazards Engineering,* Version 2, University of California, Berkeley, CA, http://doi.org/10.5281/zenodo.4558106.

Elhaddad W., McKenna F., Rynge M., Lowe J., Wang C., Zsarnóczay A. (2019). NHERI SimCenter/WorkflowRegionalEarthquake: rWHALE (Version v1.1.0), University of California, Berkeley, CA.

FEMA (2012). *HAZUS-MH 2.1: Earthquake Model Technical Manual*, Federal Emergency Management Agency, Washington, D.C.

FEMA (2018). HAZUS, Federal Emergency Management Agency, https://www.fema.gov/flood-maps/tools-resources/flood-map-products/hazus/user-technical-manuals.

Field E.H., Jordan T.H., Cornell C.A. (2003). OpenSHA: A developing community-modeling environment for seismic hazard analysis, *Seismol. Res. Lett*., 74(4):406–419, https://doi.org/10.1785/gssrl.74.4.406.

Gardoni P., van de Lindt J.W., Ellingwood B., McAllister T.P., Lee J., Cutler H., Cox, D. (2018). The interdependent networked community resilience modeling environment (IN-CORE), *Proceedings, 16th European Conference on Earthquake Engineering*, Thessaloniki, Greece,

Matsim Community (2021). Matsim: Multi-agent transport simulaton, https://www.matsim.org/2010/matsim-news-now-on-github.

Geisberger R., Sanders P., Schultes D., Delling D. (2008). Contraction hierarchies: Faster and simpler hierarchical routing in road networks, *Proceedings, International Workshop on Experimental and Efficient Algorithms*, Springer, pp. 319–333.

Golla A.P.S., Ghattacharya F.P., Gupta S. (2020). The accessibility of urgan neighborhoods when buildings collapse due to an earthquake, *Trans. Res. Pt. D, Trans. Environ*., 86(2), https://doi.org/10.1016/j.trd.2020.102439.

Guennebaud G., Jacob B., et al. (2010). *Eigen v3*, https://eigen.tuxfamily.org/index.php?title=Main_Page.

Hanks T.C., Krawinkler H. (1991). The 1989 Loma Prieta earthquake and its effects: Introduction to the special issue, *Bull. Seismol. Soc. Am.*, 81(5):1415–1423.

Hudnut K.W., Wein A.M., Cox D.A., Porter K.A., Johnson L.A., Perry S.C., Bruce J.L., LaPointe D. (2018). The HayWired earthquake scenario—We can outsmart disaster, *U.S. Geological Survey Fact Sheet 2018–3016*, 6 pgs., https://doi.org/10.3133/fs20183016.

Jayaram N., Baker J.W. (2009). Correlation model for spatially distributed ground-motion intensities, Earthq. Eng. Struc. Dyn., 38(15):1687–1708, https://doi.org/10.1002/eqe.922.

Jun H., Loganathan G. (2007a). Valve-controlled segments in water distribution systems, *J. Water Res. Pl.-ASCE*, 133(2):145–155, https://doi.org/10.1061/(ASCE)0733-9496(2007)133:2(145).

Jun H., Loganathan G. (2007b). Valve distribution and impact analysis in water distribution systems, *J. Water Res. Pl.-ASCE*, 133(8), https://doi.org/10.1061/(ASCE)0733-9372(2007)133:8(790).

Klise K., Hart D., Bynum M., Hogge J., Haxton T., Murray R., Burkhardt J. (2020). Water network tool for resilience (WNTR) user manual, *Report No. SAND2020-0301R*, Sandia National Laboratory, Albuquerque, NM.

Lee R., Kiremidjian A.S. (2007). Uncertainty and correlation for loss assessment of spatially distributed system, *Earthq. Spectra*, 23(4):753–770, https://doi.org/10.1193/1.2791001.

Lopez P.A., Behrisch M., Bieker-Walz L., Erdmann J., Flötteröd Y.-P., Hilbrich R., Lücken L., Rummer J., Wagner, P. Wießner E., (2018). Microscopic traffic simulation using sumo, *IEEE, Trans. Intell. Trans. Syst.*, 21(9):2775–2582.

Ma X., Dai Z., He Z., Ma J., Wang Y., Wang, Y. (2017). Learning traffic as images: a deep convolutional neural network for large-scale transportation network speed prediction, *Sensors*, 17(4), https://doi.org/10.3390/s17040818.

Mays L.W. (2000). *Water Distribution Systems Handbook*, McGraw-Hill and the American Water Works Assoc., Washington D.C., 900 pgs.

MTC (2018.). Time spent in congestion, Metropolitan Transportation Comission, https://www.vitalsigns.mtc.ca.gov/time-spent-congestion.

Microsoft, Inc. (2018). U.S. Building Footprints, https//github.com/microsoft/USBuildingFootprints.

Navarro C.M., Hampton S.D., Lee J.S., Tolbert N.L., McLaren T.M., Myers J.D., Spencer Jr, B., Elnashai A.S. (2008). Maeviz: Exploring earthquake risk reduction strategies, *Proceedings, IEEE Fourth International Conference on eScience*, Indianapolis, IN, pp. 457–457, https://doi.org/10.1109/eScience.2008.71.

NIAC (2009). *Critical Infrastructure Resilience: Final Report and Recommendations*. National Infrastructure Advisory Council, Department of Homeland Security, Washington, D.C.

Porter K.A. (2017). A new model of water-network resilience, with application to the HayWired Scenario, Chapter N, in *Scientific Investigations Report 2017-5013*, S. Detwiler and A. Wein, Eds., U.S. Geological Survey, Reston, VA, https://doi.org/10.3133/sir20175013.

Rossman L.A. (2000). Epanet 2: Users Manual, *EPA/600/R-00/057*, National Risk Management Research Laboratory, Office of Research and Development, U.S. Environmental Protection Agency, Cincinnati, OH.

Shi P., O'Rourke T., Wang Y. (2006). Simulation of earthquake water supply performance, *Proceedings, 8th US National Conference on Earthquake Engineering*, San Francisco, CA, pp. 547–552.

Shin S., Lee S., Judi D.R., Parvania M., Goharian E. McPherson T., Burian S.J. (2018). A systematic review of quantitative resilience measures for water infrastructure systems, *Water*, 10(2), https://doi.org/10.3390/w10020164.

Todini E., Rossman L.A. (2013). Unified framework for deriving simultaneous equation algorithms for water distribution networks, *J. Hydraul. Eng.-ASCE*, 139(5):511–526, https://doi.org/10.1061/(ASCE)HY.1943-7900.0000703.

Troutman K. (2019). *Mobiliti*, Lawrence Berkeley Laboratory, University of California, Department of Energy National Laboratory, https://cs.lbl.gov/news-media/news/2019/mobility-a-game-changer-for-analyzing-traffic-congestion.

UDST (2021). *Pandana*, Urban Data Science Tookit, https://github.com/UDST.

Wagner J.M., Shamir U., Marks D.H. (1988). Water distribution reliability: simulation methods, *J. Water Res. Pl.-ASCE*, 114(3):276–294, https://doi.org/10.1061/(ASCE)0733-9496(1988)114:3(276).

Wald D.J., Quitoriano V., Heaton T.H., Kanamori H. (1999). Relationships between peak ground acceleration, peak ground velocity, and Modified Mercalli intensity in California, *Earthq. Spectra*, 15(3):557–564, https://doi.org/10.1193/1.1586058.

WGCEP (2008). The Uniform California Earthquake Rupture Forecast, Version 2 (UCERF 2), Working Group on California Earthquake Probabilities, *U.S. Geological. Survey Open-File Rept. 2007-1437, the California Geological Survey Special Report 203, Version 1., SCEC Special Contribution 1138*, State of California, Sacramento, CA.

Yoo D.G., Jung D., Kang D., Kim J.H., Lansey K. (2016a). "Seismic hazard assessment model for urban water supply networks, *J. Water Res. Pl.-ASCE*, 142(2), https://doi.org/10.1061/(ASCE)WR.1943-5452.0000584.

Yoo D.G., Jung D., Kang D., Kim J.H. (2016b). Linear model for estimating water distribution system reliability, *J. Water Res. Pl.-ASCE*, 142(8), https://doi.org/10.1061/(ASCE)WR.1943-5452.0000664.

Appendix A: Supplement Materials for HydrauSim

A.1 ISOLATION VALVES INPUT FORMAT

To efficiently add leakage information to a WDN, the EPANet .inp file has been extended to allow users to input leakage information conveniently. HydrauSim can automatically parse the leakage information from the extended .inp file and run pressure-driven hydraulic simulation to quantify leaks. Each leak is represented by two properties. NID is the name of the node that may experience leakage. Diameter is the diameter of the leak, which is used for leak quantification with Equation (2.8). All leakage information can be grouped to the [LEAKS] section and appended to the .inp file. Figure A.2 shows an example of the [LEAKS] section.

Note that the leaks section should be appended after the [END] section in the original .inp file to allow the file to be compatible with EPANet or WNTR.

A.2 ISOLATION VALVES INPUT FORMAT

To efficiently add isolation valves to a WDN, the EPANet .inp file is extended to allow users to conveniently input the configuratoin of the isolation valves. HydrauSim can automatically parse the isolation valves information from the extended .inp file and generate the corresponding segment-valves graph. Each isolation valve is represented by three properties. ID is the name of the isolation valves. Node is the closest node id to the isolation valve, and pipe is the pipe id that the isolation

```
[LEAKS]
;NID                Diameter
node1                   3 ;
node2                   5 ;
node3                   8 ;
```

Figure A.1: Format of leaks information for the extended EPANet .inp file.

```
[ISOVALVES]
;ID                 Node            Pipe
V1                  2               P1  ;
V2                  4               P3  ;
V3                  2               P4  ;
V4                  3               P4  ;
V5                  6               P5  ;
```

Figure A.2: Format of isolation valves for the extended EPANet .inp file.

valve is placed on. All the isolation valve information can be grouped to the [ISOVALVES] section and appended to the .inp file. Figure A.2 shows an example of the [ISOVALVES] section.

Note that the isolation valve configuration section should be appended after the [end] section in the original .inp file to allow the file to be compatible with EPANet or WNTR.

A.3 SYNTHETIC WDNS GENERATION PROCEDURE

Synthetic WDNs are useful to profile the computation speed of hydraulic simulation programs as network attributes such as network size can be controlled by users. A simple yet effective algorithm is used in this study to generate synthetic water distribution networks that resemble real WDNs:

1. User inputs the desired size of the network, N. Let the square root integer of N to be n.
2. Generate a n by n grid graph.
3. Randomly remove edges with probability p.
4. Randomly assign node properties to nodes from the node property pool (uniform sampling)
5. Randomly assign pipe properties to remaining pipes from the pipe property pool (uniform sampling)
6. Connect reservoirs to the nodes at the four corners at higher elevations
7. Finish generating the synthetic network.

From graph theory, the number of edges e for a n by n grid graph is given as:

$$e = 2n^2 - 2n \tag{A.1}$$

Hence, the ratio of number of edge e to the number of nodes n^2, r can be calculated as:

$$r = 2 - \frac{2}{n} \tag{A.2}$$

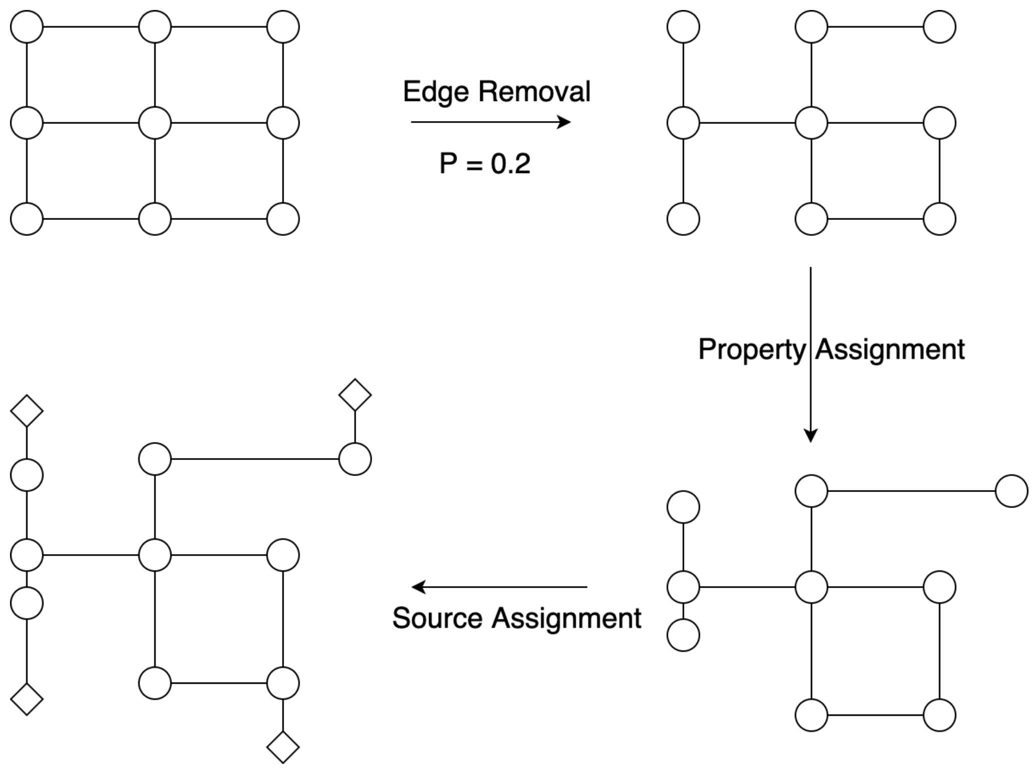

Figure A.3: The procedure to generate a synthetic network with 9 nodes.

Since r for real-world networks is around 1.5, setting the probability of removal p to 0.2 leads to $r \approx 1.6$ for large networks. Generation of a synthetic WDN with 9 nodes is illustrated by Figure A.3.

The node property pool used in this study is:

Table A.1: Node properties used for creating synthetic WDNs.

	Min	Max
Elevation(ft)	400	900
Demand(GPM)	0	5
Head for sources(ft)	500	1000

The pipe property pool used in this study is shown in Table A.2.

Note that synthetic networks are used for program profiling purposes; therefore, additional components such as pumps and valves are not included in the network generation procedure. All hydraulic simulations running on all of the generated synthetic networks with procedures and configurations described above converge.

Table A.2: Pipe properties used for creating synthetic WDNs.

	Min	Max
Length(ft)	200	800
Diameter(inch)	3	20
Roughness(unitless)	120	155

The Pacifi c Earthquake Engineering Research Center (PEER) is a multi-institutional research and education center with headquarters at the University of California, Berkeley. Investigators from over 20 universities, several consulting companies, and researchers at various state and federal government agencies contribute to research programs focused on performance-based earthquake engineering.

These research programs aim to identify and reduce the risks from major earthquakes to life safety and to the economy by including research in a wide variety of disciplines including structural and geotechnical engineering, geology/seismology, lifelines, transportation, architecture, economics, risk management, and public policy.

PEER is supported by federal, state, local, and regional agencies, together with industry partners.

PEER Core Institutions

University of California, Berkeley (Lead Institution)
California Institute of Technology
Oregon State University
Stanford University
University of California, Davis
University of California, Irvine
University of California, Los Angeles
University of California, San Diego
University of Nevada, Reno
University of Southern California
University of Washington

PEER reports can be ordered at https://peer.berkeley.edu/peer-reports or by contacting

Pacific Earthquake Engineering Research Center
University of California, Berkeley
325 Davis Hall, Mail Code 1792
Berkeley, CA 94720-1792
Tel: 510-642-3437
Email: peer_center@berkeley.edu

ISSN 2770-8314
https://doi.org/10.55461/MYSN6989